DESIGN AND FABRICATION OF ROBUST HIGH PERFORMANCE PIEZOELECTRIC MICRO-DEVICES

by

Choong-Ho Rhee

A dissertation submitted in partial fulfillment
of the requirements for the degree of
Doctor of Philosophy
(Mechanical Engineering)
in The University of Michigan
2012

Doctoral Committee:

Assistant Professor Kenn Richard Oldham, Chair
Professor A. Galip Ulsoy
Professor Euisik Yoon
Associate Professor Katsuo Kurabayashi

2012

To my family

ACKNOWLEDGEMENTS

First of all, I express my sincere appreciation to Professor Kenn R. Oldham for his guidance, patience, and support. Two areas of the research and dissertation could not been accomplished without him. I appreciate the time taken by Professor A. Galip Ulsoy, Professor Euisik Yoon, and Professor Katsuo Kurabayashi to serve on my dissertation committees.

The outcome of the microfabrication process in this dissertation could not been completed without any advice from many people, who perform their research or support the researchers, at Lurie Nanofabrication Facility. I would like to express thanks to Dr. Pilar Herrera-Fierro, Dr. Nadine Wang, Terre Briggs, Tony Sebastian, Brian Vanderelzen, Ed Tang, Greg Allion, Katharine Beach, Russ Clifford, Matt Oonk, Tom Latowski, and Steven Sostrom for their plentiful instruction on microfabrication. I also thank Mr. Joel Martin and Mr. Brian Power for metallization and milling at U.S. Army Research Laboratories, and Ms. Luz Sanchez for PZT deposition at Radiant Technologies, Inc.

For experimental testing, I thank Katherine Knisely and Professor Karl Grosh in Vibrations and Acoustics Laboratory, and Fatih Ozkeskin and Professor Yogesh Gianchandani in Solid State Electronics Laboratory. And I thank other former and present members in Vibrations and Acoustics Laboratory for general help in research. I

am grateful for the friendship of the micro-robotics team members, Biju Edamana, Bongsu Hahn, and Jeong-Hoon Ryou, who have been developing the bio-inspired micro-robotic system in different areas, Ryan Rudy who worked on weight bearing simulation of thin-film PZT actuator structure, and Christopher Kao who worked on yield test of thin-film PZT actuator samples. And I am also grateful for the friendship of all of the members of Professor Kurabayashi's and Professor Wang's group, especially Zhen Qiu, with whom I worked closely on many assignments.

And, I appreciate the unending support from my parents and family. Thank you.

TABLE OF CONTENTS

LIST OF FIGURES

FIGURE

LIST OF TABLES

TABLE

LIST OF APPENDICES

ABSTRACT

Two research tasks are performed to achieve robust fabrication and uniform dynamic performance of complex piezoelectric micro-electromechanical systems: first, production of complex thin-film lead-zirconate-titanate (PZT) microdevices requiring high-yield chip-level process robustness; second, design for feature-level parametric robustness that improves the finite-time dynamic performance uniformity of piezo-MEMS devices.

Thin-film PZT actuators are integrated in a robust way with silicon microstructures via the latter's encapsulation by vertical silicon dioxide barrier trenches. The process conserves piezoelectric performance with high actuator yield and supports multi-level structure fabrication. Two prototype devices that take advantage of this process to produce multiple-degree-of-freedom motions and large displacements with fast response times are characterized experimentally. For the first prototype, a micro-robotic leg joint, displacement modeling is performed that includes compensation for intrinsic residual stress of thin-film stacks, oxide barrier trench properties as they influence behavior of in-plane flexure joint arrays, and the stiffness of an electrical interconnect structure across compact actuator arrays. The modeling approach and empirical measurements show good agreement for multi-degree-of-freedom static displacements. For the second prototype, a vertical translational z-axis focusing stage for endoscopic

microscopes, the fabrication process allows backside etching to release stages actuated by multi-fold thin-film PZT vertical actuators. Motion generated by the proposed vertical translational z-axis focusing stage is targeted up to 200μm, and the transient response of two-fold stage is shown and found to be faster than other existing actuation mechanism of endoscopic micro-mirror platform.

For design of robust finite-time transient response of piezoelectric MEMS devices the maximum perturbed finite-time transient behavior of the system is represented by the spectral radius of a compact matrix. This allows efficient optimization of the worst-case scenario for perturbed finite-time transient response. In case studies, locally optimal structural parameters of piezoelectric micro-electromechanical systems were obtained. Using μ-synthesis analysis, the maximum perturbation is estimated systematically when compared to randomly generated samples, which may not guarantee the maximum perturbed finite-time transient response.

CHAPTER I

Introduction

1.1 Research Introduction and Background

The end user market for micro-electromechanical systems (MEMS) has grown dramatically since its birth from integrated circuit (IC) technology [36], [37], [88], requiring increasing reliability and performance robustness from MEMS devices. In this dissertation, two important aspects of design and fabrication of robust, high-performance MEMS are considered, with respect to novel devices based on piezoelectric actuation. The first aspect is the production of complex thin-film piezoelectric microdevices requiring high-yield wafer- or chip-level process robustness when integrated with moving silicon micro-structures. The second aspect is design for feature-level parametric robustness that improves the finite-time dynamic performance uniformity of such devices.

Among miniaturized MEMS components or devices, a micro-actuator is a micro-machined electromechanical structure capable of generating motion from miniaturized transduction mechanisms. These mechanisms includes electrostatic, electrothermal, electromagnetic, shape memory alloy or piezoelectric effects [92], [93], [94], usually integrated with various mechanical transmission elements. When the micro-actuator mechanism is integrated with other complex micro-structures, there remains a need for

advanced techniques for increasing feature-level and wafer-level process robustness. Among various micro-actuators, similar to other smart material-based actuation structures, piezoelectric micro-actuators offer especially high areal work densities.

Example systems of complex micro-structures actuated by piezoelectric microactuators are presented in Figures 1.1 – 1.4. These systems show several desired applications of advanced thin-film piezoelectric, as well as some bulk ceramic piezoelectric, actuators: a bio-inspired autonomous micro-robotic platforms that would provide new capabilities in security and rescue missions (Figure 1.1); a vertical translational z-axis focusing stage which could help provide *in vivo*, non-invasive large depth-of-field detection of cancer to medical professionals and researchers (Figure 1.2); a simplified version of the micro-robotic platform driven by bulk Lead-Zirconate-Titanate (PZT) ceramic actuator mechanism (Figure 1.3); and a large-displacement amplifying mechanism for endoscopic microscopy applications (Figure 1.4).

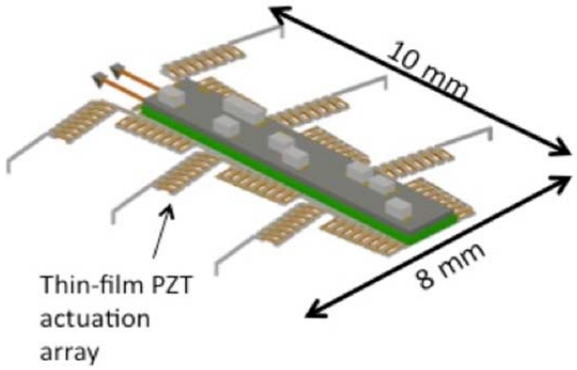

Fig. 1.1 Bio-inspired autonomous micro-robotic platform

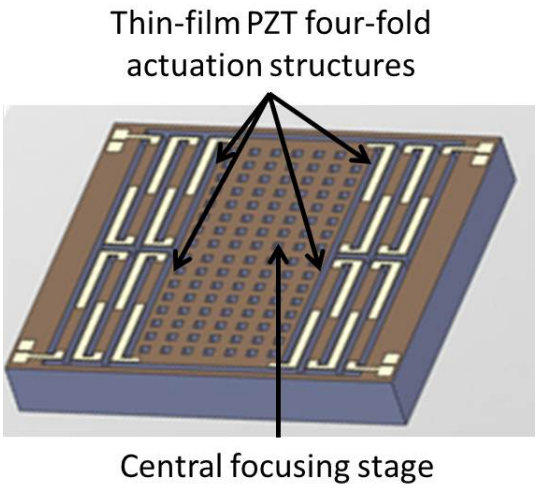

Fig. 1.2 Vertical translational z-axis focusing stage

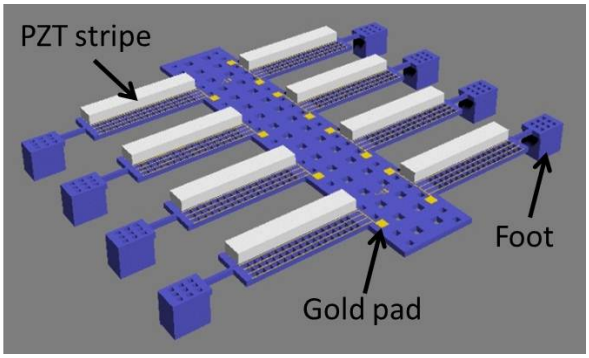

Fig. 1.3 Bulk PZT actuator driven micro-robotic platform

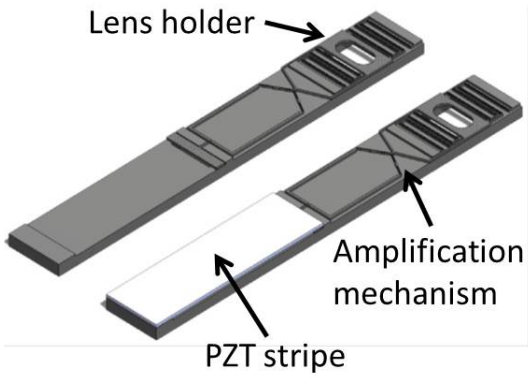

Fig. 1.4 Bulk PZT large-displacement amplifying mechanism

From the structural standpoint, these piezoelectric MEMS devices contain at least two elements: a micromachined frame, primarily silicon, and a piezoelectric deflection element fabricated or assembled onto the silicon frame. But the manufacturing procedures incorporating piezoelectric materials with the associated structural components at the wafer level are challenging. Thin-film PZT unimorph bending actuators integrated with complex multi-layer silicon structures, as in Figures 1.1 and 1.2, have significant fabrication and design complexity when device-specific geometric requirements and processing conditions need to be satisfied. Possible specifications include minimum feature sizes, planar or three-dimensional topographies, structure and trench aspect ratios, residual stress compensation, polymer-free and residue-free surfaces, and so on. Obtaining adequate yield is also a challenge for microfabrication of thin-film PZT actuated micro-devices when the specifications mentioned above are to be met by numerous thin-film PZT actuation structures. Even with high-yield fabrication, achieving required dimensional tolerances and accuracy and positional accuracy can be significant challenges when wafer bonding, photolithography, and etching processes are performed to define the geometry of complex structures. This in turn affects the finite-time dynamic response of the device. Bulk PZT driven micro-devices with layer thicknesses near one hundred microns, such as in Figures 1.3 and 1.4, also have substantial dimensional variations in forming and assembly to the remainder of the device.

Therefore, a need exists to overcome certain key obstacles related to processing variability for integrating piezoelectric materials into complex electro-mechanical systems. Two research tasks are aimed to achieve such results in this dissertation, and some modeling of behavior of the resulting microdevices is also performed.

As the first task, production of complex thin-film piezoelectric microdevices requiring high-yield chip-level process robustness using silicon barrier trenches and associated processing is conducted. The device focused on is a multi degree-of-freedom micro-robotic leg joint. Piezoelectric coefficient measurement using sample piezo-cantilevers is conducted to verify piezoelectric performance of the finished microdevices. Modeling and empirical verification of static displacement of the resulting piezoelectric micro-devices is also performed, to incorporate the expanded number and type of piezoelectric actuators in the devices into their system models. Finally, the dynamic response behavior of the resulting devices, the first resonance frequency and the quality factor (Q-factor), are found by frequency sweeping.

As the second task, design for feature-level parametric robustness is performed to improve the finite-time dynamic performance reliability of such devices. In addition to thin-film PZT actuated microdevice fabricated from the first task of the chip-level process robustness, a bulk-PZT actuated microdevice is also considered for feature-level parametric robustness in the design case study. By careful selection of feature-level dimensions, an attempt is made to minimize the variability in device performance due to variability of fabrication processes that cannot be completely dealt with by processing improvements. This is done by adapting transient dynamics into models that may be analyzed using robust design techniques from the robust control field.

The following sections introduce the background of the key concepts related to design and fabrication of low-yield-loss micro-devices, including some common difficulties in development of small-scale components, and key concepts related to robust finite-time dynamic performance of piezoelectric micro-devices.

1.2 Background of Key Concepts

1.2.1 Background on Lead Zirconate Titanate (PZT) Actuator

In this section, the characteristic of PZT and the fabrication process for a PZT actuator structure are introduced. Piezoelectric materials expand or contract when an electric field is applied according to the orientation and strength of the field. Piezoelectric materials are typically categorized into three groups: (1) low strain piezoelectrics such as Quartz, which strain by up to $3x10^{-5}$ upon application of an electric field, (2) high strain piezoelectrics such as lead zirconate titanate, which strain by up to $2x10^{-4}$ and are most commonly used in microsystem [10], [13], and (3) piezoelectric polymers such as polyvinylidene fluoride (PVDF) which can strain by up to $1x10^{-3}$.

Compared to other mechanical actuators, PZT actuators generally have a high cyclic power coefficient and high maximum power density per unit volume, proportional to the frequency of operation, which in turn is limited by structural resonance or thermal dissipation. It is known that PZT actuators can exhibit a faster response (or maximum frequency) by an order of 10^5, compared to most other types of macro-mechanical actuators [9]. PZT ceramics, in particular, have relatively high piezoelectric coefficients and electromechanical coupling factors compared to other piezoelectric ceramics, as shown in Table 1.

Thin-film piezoelectrics are fabricated using thin film deposition techniques such as sol-gel spinning, plasma sputtering, or chemical vapor deposition [13]. It is known that high maximum force and energy density, fast dynamic response time, low input power and low driving voltage can be achieved compared to existing electrostatically- and thermally-actuated devices [24], [34]. For example, electrostatic actuation is relatively

easy to implement and offers large amplitude actuation but at the cost of larger driving voltages and more limited actuation forces for actuator voltages and areas equivalent to most piezoelectric actuators. Current-based actuation, as in magnetically- and thermally-actuated devices, usually requires comparatively high power dissipation, and the latter type tends to respond slowly in dynamic motion due to comparatively long thermal time constants [11]. Furthermore, electromagnetic motors show poor scaling with size at the micro-scale while piezoelectric actuators have high energy density even as device sizes drop to the micro-scale [12]. It is also known that piezoelectric thin-films are adequate for integrated sensing devices requiring large output signals, low noise, or high frequency operation [34].

The main difference, from an implementation standpoint, between thin-film PZT and bulk PZT materials lies in the fact that thin films are typically used in composite structures where the total elastic properties are dominated by the other materials, such as a silicon cantilever or a silicon dioxide or silicon nitride membrane [11]. Note also that the fabrication techniques for thin film and bulk materials are different. Thin film PZT fabrication is based on several iterations of thin-film deposition, photolithography and etching [10]. On a polished substrate coated with an electrical insulator layer such as silicon dioxide (SiO_2), a titanium (Ti) adhesion layer and platinum (Pt) bottom electrode are deposited by sputtering. Then, PZT is deposited via a chemical-solution-derived deposition process (sol-gel) or sputtering, and a top Pt electrode is deposited. To open contact vias to the bottom electrode, the vias area of PZT film is etched by wet or dry etching [10], [24]. On the other hand, bulk PZT ceramic is manufactured from a mixture of lead zirconate/lead titanate powders [32]. Fine powders of the component metal oxides

are mixed and heated to form a uniform powder. Then it is mixed with an organic binder and formed into structures with desired shapes such as discs, rods, and plates. By sintering, the material attains a dense crystalline structure, then the material is cooled and trimmed, and a poling treatment is performed [32]. However, etching of bulk PZT ceramic using the thin film etching techniques is difficult due to the slow etching rates and, in the case of wet etchants, the severe undercut resulting from the isotropic etching. Instead, dicing, lapping, sand blasting, or krypton fluoride (KrF) excimer laser cutting can be employed for patterning bulk PZT ceramic [14].

Table 1 Comparison of Piezoelectric Materials in MEMS Applications

	Piezoelectric Coefficient, d_{33} (pm/V)	**Dielectric Constant**	**Electromechanical Coupling Factor**
Zinc oxide (ZnO)	5.9	10.9	0.27
Aluminum nitride (AlN)	3.9	10.5	0.24
PZT	60 ~ 130	300 ~ 1300	0.39 - 0.5

However, the aforementioned existing fabrication techniques for thin-film PZT and bulk PZT ceramic often result in substantial variability of the manufacturing process. In the thin-film processing of the multiple material stacks and sacrificial layer removal, the sources of variability that could be overcome by the first research task to be performed are failure of the resulting device protection during sacrificial layer removal and inconsistent geometric topography of post-sacrificial layers by gaseous timed etching. In the assembly processing of the patterned bulk ceramic onto a micro-machined frame or thick-film processing, the misalignment of the final assembled structure or the parametric variation of the patterned thick-film is the variability that could be mitigated by the second task in this dissertation.

1.2.2 Piezoelectric MEMS Device Application: Bio-Inspired Autonomous Micro-Robotic Platform and Vertical Translational Z-Axis Focusing Stage

The most common piezo-MEMS devices that are reported in the literature, some already commercialized, are micro-pumps and valves, ultrasonic motors, probes for non-destructive testing, and accelerometers and electronic components that include filters, memory devices and switches. For those micro-pumps, valves, and switches, the piezoelectric actuation mechanism is based on disk, cantilever, or stacked structures [110], which generate out-of-plane motion by unimorph piezoelectric actuation [111]. While these devices operate in the small displacement range, large displacement piezoelectric micro-actuation structures generating 500μm to 1mm displacement will be considered for the autonomous micro-robotic devices and vertical translational z-axis focusing stages.

In this dissertation, two newly-developed example systems actuated by thin-film PZT are considered. The first thin-film PZT-actuated system is the micro-robot in Figure 1.1, along with its bulk PZT-actuated simplified version in Figure 1.3, which is in some sense a modified chip fabricated by silicon micromachining technologies. Several previous researchers have demonstrated micro-robots of less than one centimeter in length, using various actuation types and mechanisms. In 1999, Ebefors et al. built a silicon walking robot with thermally-actuated, single degree-of-freedom, spin-coated polyimide leg joints able to carry loads more than 30 times the weight of the robot, though its power supply was maintained through tethered bonding wires [74]. In 2003, Hollar et al. built electrostatic inch-worm motors to generate high forces in a two-legged micro-robot from on-board solar cells and a 50V high-voltage translator [76]. In 2007,

Bergbreiter et al. integrated electrostatic inchworm motors with molded elastomers to generate a rapid jumping motion from on-board 50V high voltage buffers and solar cell arrays [77]. In 2008, Donald et al. used electrostatic scratch drives, and in 2001 [78], Mohebbi et al. used thermally actuated silicon motors to drive high force motion [79]. However, these approaches limit mobility due to limited degrees-of-freedom, small actuation angles, while the mechanisms providing high forces (thermal actuation) require large actuation power.

For high-bandwidth, high-mobility, and low-power micro-robotics, Oldham et al. developed a thin-film PZT actuator design in 2008 that produced high work-density lateral displacements from combinations of unimorph actuators and could recover portions of the electrical energy used to drive the actuators using charge recovery circuitry [24]. Actuator arrays created from the lateral actuators could generate series rotational motion at 20V that might enable the high-mobility walking of autonomous micro-robotic platforms [81]. However, the thin-film PZT unimorph bender integrated with complex multi-layer silicon structures proved difficult to expand to multiple-degree-of-freedom leg design, due to limitations on thin-film PZT device processing. A modified, more reliable fabrication process is the first topic under consideration in this dissertation, followed by modeling of the resulting multi-degree-of-freedom robotic leg joints. More generally, piezoelectric MEMS devices require amplifying transmission structures to produce large displacements. Novel design of the transmission structure also provides multi-axes, multi degree-of-freedom motion, despite the motion of piezoelectric materials being limited to only short-range elongation or contraction.

Other PZT-actuated systems can be created with similar process flows and actuator designs. Examples include a vertical translational z-axis focusing stage used for a novel fluorescence endoscopic instrument that can rapidly image the surface of the distal esophagus [90]. This target instrument in which the z-axis stage would be installed would be capable of passing through the working channel of a standard medical endoscope so that dual-axes confocal imaging can be used to guide tissue biopsy in a dual channel endoscope [90]. The focusing device proposed for this instrument is a thin-film PZT actuated z-axis focusing stage fabricated by the same process as micro-robotic leg joints, with additional benefits from backside processing and reduced processing variability. The details of this device are included in Appendix C. Other examples of devices that are fabricated through the proposed process include adaptive optics components, antenna-like tactile sensors, and x-y nanopositioner [112].

1.2.3 Background on High-Yield Microfabrication of MEMS

As noted earlier, thin-film piezoelectric materials have significant advantages over other transduction mechanisms for microactuation and sensing in many situations, thanks to high work density, low voltage requirements, and potential for high frequency operation. However, strict limitations on their deposition and treatment, especially in the case of lead-zirconate-titanate (PZT), which has especially high piezoelectric coefficients and dielectric constants, can severely impede their integration with other micro-structures. For example, the key challenge of piezoelectric thin-film fabrication in the micro-robotic leg joints in [24] is that low actuator release yield was observed when isotropic xenon difluoride (XeF_2) etcher undercuts the silicon understructure [24], which

in turn often results in a variation in length of the undercut area of a piezoelectric actuator [24] or damage to silicon flexures and tethers needed to amplify motion. This limits the quantity of actuators that can be included in a single device, preventing the target high-mobility robot appendages with multiple, large range-of-motion degrees-of-freedom.

The challenge of increasing yield in order to increase complexity and capabilities of other MEMS systems is also becoming an urgent need, not just for the thin-film piezoelectric microdevices [8], with increasing applications of MEMS to fields such as health care, environmental monitoring, and infrastructure maintenance [36], [37]. Thus, to successfully fabricate functional but increasingly complex devices, robust and high-yield microfabrication processes need to be developed for each device and application.

However, the following examples in the literature demonstrate that MEMS fabrication processes are dependent on its application, and need to be customized for a particular case. In [22], several challenges are classified for MEMS packaging processes. Since then many researchers have focused on novel and high-yield fabrication technologies for their device application, although expertise, experience and know-how from the manufacturer in MEMS industry often remain proprietary secrets. In [21], two different fabrication approaches are considered during wafer bonding and deep reactive ion etching (DRIE) process in their device application. Although both proposed approaches seem feasible, they experience fabrication failure due to the arcing of gases inside the chamber during wafer bonding process, and loss of heat dissipation capability during DRIE process which subsequently causes loss of photoresist mask layer. To resolve this application-specific issue which could be also resolved by changing the layout as mentioned in [21], incorporating an additional metal layer deposition prior to

silicon glass bonding is proposed from a fabrication point of view, and a DRIE-after-bonding approach is proved to be capable of producing high yield of devices. In [20], fabrication of a polyimide-based flexible sensor array is considered. Compared to the previous works related to MEMS devices made on a flexible substrate, polyimide is selected for excellent electrical and thermal insulation, high chemical resistance, high-temperature stability, and high flexibility. From a high-yield perspective, a spin-coated Polydimethylsiloxane (PDMS) interlayer between the silicon carrier wafer and the polyimide substrate is proposed because the low adhesion between oxygen plasma-treated PDMS and the polyimide enables them to separate easily. Examples of wafer level encapsulation from MEMS packaging technique can be also considered as high-yield fabrication techniques. To avoid the die attach material and coefficient of thermal expansion mismatch, which causes large wafer bowing and eventually device failure, bonding of a silicon wafer and two glass wafers are used in [17]. As one of the wafer bonding techniques, adhesive wafer level bonding in [18] using Benzocyclobuene (BCB) is also considered for a high-yield technique since the bonding temperature is much lower than that of fusion or anodic bonding, and the demand for the roughness of the wafer surface is not very critical. In addition to wafer-to-wafer bonding techniques for encapsulation, polymer encapsulation can be applied to protect movable and delicate micro-structures. For example, [19] uses double-side coated polyimide to protect the mirrors against the strong water flow, which serves as a coolant and a lubricant, and other shocks during the dicing step. This encapsulation for dicing protects the device from diamond particles that are generated during sawing and possibly contaminate the device.

Although the aforementioned are just a few examples of fabrication processes selected for high yield microdevice, it can be concluded that reliable integration of different fabrication techniques to a process flow brings out the potential to produce lower yield loss MEMS devices in specific applications. Development of the microfabrication process flows for high-yield production is customized, and expertise, experience and know-how are required prior to development, and can be obtained during and after the development. Therefore, in the proposed research, emphasis is given to high-yield fabrication techniques for thin-film piezoelectric actuator structures.

1.2.4 Background on Robustness in MEMS

Even when fabrication device yields are significantly improved, significant variability between devices may remain that must be dealt with by other means, such as through robust design of the devices or processes. The fundamental objective of robust design methodologies is the development of systematic methods for achieving insensitivity of products and processes to sources of variations and noise factors that cannot be easily controlled or eliminated [1], [2]. From [1] and [2], the motivation and research directions for robust high-yield MEMS design can be depicted schematically as shown in Figure 1.5. The first step in a systematic robust design methodology is an awareness of variation. In [6], [7], and [17], among others, the causes of variation in MEMS application are fabrication errors, material property uncertainty, and environmental uncertainty that can critically affect long-lasting system performance. Through awareness of variation, it is determined which variables and parameters are sensitive to variations so that controllable variables can be optimized in the early design

process. The determination of the controllable variables is based on prior knowledge and experience of the device design and microfabrication processes design, or cause-effect analysis. Modeling in terms of nominal and variant terms also helps the cause-effect analysis if the system model is well-known in advance.

Two directions can be proposed to study how to achieve insensitivity of products and processes in the second step in Figure 1.5. One is to study robust design techniques from the mechanical and/or electrical design perspective, and the other is to develop application-specific high-yield microfabrication techniques from the production process perspective. The latter case of process improvement for reduced yield loss was discussed in Section 1.1.1 and 1.1.3 and a solution is presented in Chapter II for the problem of integrating thin-film lead-zirconate-titanate with complex, high-aspect ratio micro-structures. In the former case of robust design, traditionally the controllable variables obtained from the first step are converted into performance measures that represent the quality characteristics of the product being designed. Signal-to-Noise ratio from Taguchi's method, which is widely used in MEMS design, and quadratic functions of state and input energy terms from optimal control theory are two examples of a performance measure used in robust design. From a probabilistic point of view, such as in [4], a stochastic approach models uncertainties that correspond to noise factors as random variables, and the probabilistic bounds on estimates of the performance measure are minimized. When defining performance measures in a probabilistic manner, other researchers also consider minimizing the variance of distribution and the sensitivity, such as in [5], [6], and [7]. From a deterministic point of view, the bound of the worst case scenario is often chosen as the performance measure, with methods such as an ellipsoid

algorithm considered to minimize the smallest ellipsoid that encloses all possible noise factors in [4].

Having chosen to address robust performance from the design or processing perspective, in the third step of "Details" development shown in Figure 1.5, previously developed techniques can be directly applied or modified, or new techniques can be developed for the mechanical design or process design of the specific MEMS applications. In the proposed research, although it is impossible to prevent all variation or ensure all physical structural yields, a robust design technique for the dynamic response of a microfabricated mechanical system is considered with emphasis on the finite-duration transient response, and the design techniques are developed from a deterministic viewpoint. Case studies related to high-yield microfabrication techniques are already mentioned in Section 1.1.3, and related studies of robust design techniques for micro-scaled dynamic systems in the literature are presented in the following section.

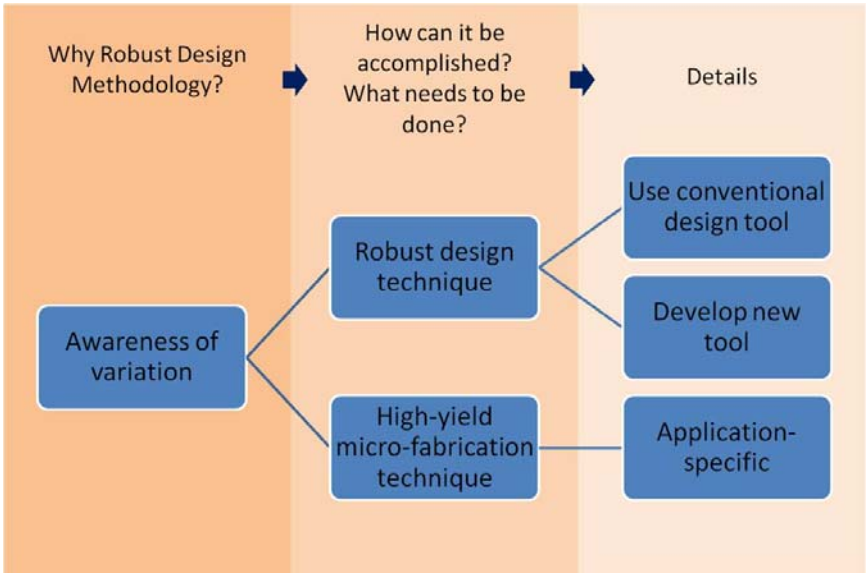

Fig. 1.5 Motivation and research direction of robust high-performance MEMS

1.2.5 Background on Robust Transient Response of Dynamic System

Fabrication processes associated with MEMS often have significant variation or error relative to the size of the device. For example, layers are subject to geometrical uncertainties due to fabrication variations, such as mask misalignment during photolithography process and variation of etching profiles during reactive ion etching. The structural properties of deposited film structures, such as elastic modulus and residual stress, depend not only on deposition parameters but also on the actual equipment and the history of that equipment used. Wafer-to-wafer bonding techniques entail significant misalignment errors which can have a major effect on structural dynamics. These variations related to microfabrication processes result in deviation of structure stiffness, total mass and possibly damping constant from their nominal designed values. Therefore, a robust design technique for a micro-scaled dynamic system is important for the systems' dynamic performance.

Previous work on robust design techniques for micro-scaled dynamic systems can be grouped into two approaches: robust open-loop design and robust feedback control design approaches. The former approach is based on a multi-objective constrained optimization and open loop dynamics are directly optimized without feedback control implementation. For example, one optimization problem is to match the natural frequency of a system with random vector of noise factor to a predefined natural frequency when the effect of variant natural frequency is minimized [39]. In robust feedback control design approaches, robust design techniques, such as H_∞ minimization, mixed H_2/H_∞ control and μ-synthesis (structured singular values), are employed [31], [43-45], [48], [50]. For example, Li et al. proposed an adaptive dynamic surface control

and H_∞ control technique to ensure robust tracking of parallel-plate electrostatic actuator in the presence of parametric uncertainty and external disturbance [48]. Zhu et al. used backstepping control design for electrostatic actuator with uncertain parameters [50]. From the robust performance and transient response perspective, the linear time-invariant system is represented in the form of a generalized plant [31], and an n-th order controller is considered. Uncertainties in parameters of lumped modeled plant, linearization error, and unmodeled dynamics are assumed. For their μ-synthesis, previous work on DIA (Disturbance and Initial-state Attenuation) control is used to generate the initial controller in an iterative optimization, and a D-K iterative calculation for controller synthesis is applied with the initial controller being set up with H_∞ DIA in the iteration. One of the limitations of the aforementioned approaches is that they are applicable for infinite horizon cases. Due to short duration operating time of many MEMS devices, such as MEMS switches [47], MEMS logic gates [71], [72], or micro-robots [70], the transient behavior is often the most important aspect in dynamic performance [46], [47]. In response, finite-time control design, with fewer previous examples such as [52] where the discrete system is concerned, can be considered to overcome such limitation.

In the development of the finite-time robust design technique, μ-analysis is applied from robust control theory in this dissertation. The upper bound of the performance objective to be minimized is represented in linear fractional transformation (LFT) representation, which is further used in worst-case performance minimization by μ-analysis. More specifically, instead of picking random parametric samples to generate the perturbed finite-time transient response, which may not be the maximized perturbation, μ-represented upper bound of the perturbed finite-time transient

performance is computed for the maximum perturbed finite-time transient response. Furthermore, this μ-based optimization shows the reduced computation time when compared to the possible perturbed case scenario selected by the random uniform distributed samples of parametric dimensions.

1.3 Thesis Outline

This dissertation presents the results of the followings in Chapter II, III, and IV, respectively:

- In Chapter II, improved state-of-art fabrication process for less-than 1μm-thick thin-film Lead-Zirconate-Titanate (PZT) actuator is presented. Robust encapsulation of structural components in the complex devices via silicon dioxide barrier trenches enabled uniform undercut of thin-film PZT layer during xenon difluoride (XeF_2) gaseous isotropic etching. In addition, backside processing was allowed for fabrication of two-level silicon structures of the complex device from a silicon-on-insulator (SOI) wafer. High-yield fabrication of numerous thin-film PZT actuators in the complex device was conducted. The procedure developed is potentially applicable to a wide variety of thin-film piezoelectric devices.
- In Chapter III, improved modeling and experimental characterization of thin-film PZT robotic leg that consists of numerous actuators generating multi-degree-of-freedom motion is presented. From the original modeling of the parallel uncompact in-plane actuator arrays in [81], the new and improved modeling of vertical and lateral motions of actual multi degree-of-freedom microrobotic legs,

which were fabricated in (1), were obtained. The estimated motion from the improved modeling was shown and compared to the experimental results, which show good agreements in the multi-degree-of-freedom displacements. While this modeling effort is limited to a specific piezoelectric device, it demonstrates that performance of piezoelectric devices can be accurately predicted with knowledge of processing limitations.

- In Chapter IV, a method for robust design of finite duration transient response of a system subject to parametric variations is presented. A proposed performance measure of minimal error between the worst case perturbed response and the nominal response is converted to a structured singular value of a certain time-varying matrix. In a case study, finite-duration transient behavior of 500μm-thick bulk-PZT actuated robotic leg was optimized for the robustness with respect to nominal finite-duration transient response. Since the worst case difference from the nominal response could not be greatly reduced by updating only structural dimensions during optimization procedure, the state feedback gain was considered, as if all states of a system were measurable, so that the closed-loop, robust finite-duration transient behavior was obtained. The case studies for this procedure focus on piezoelectric microdevices, but the theoretical approach is applicable to any linear dynamic system subject to bounded model perturbations.

CHAPTER II

Robust Microfabrication of Thin-Film PZT Micro-Devices

2.1 Introduction

Thin-film PZT is generally produced from sputtering or chemical-solution-derived deposition on an appropriate substrate with complementary metal and insulating thin-films. For the type of thin-film PZT actuator processing in this dissertation [24], patterned thin-film PZT layers with various stack geometries are connected to high-aspect ratio silicon structures. At one end of the PZT actuator the silicon structures are movable, and at the other end the silicon serves as an anchor, which is a fixed silicon structure. However, as will be discussed in Section 2.2, there are limitations of the processing of thin-film PZT actuator structure. These include inconsistent actuator undercut length and the incapability of backside patterning for multi-layer piezo-MEMS structures. The solution developed to overcome these limitations is to use oxide barrier trenches for encapsulation of the silicon connectors at both ends of thin-film PZT actuators and other complex silicon structures in the proposed microdevices. Simultaneously, the oxide deposition provides hard mask layers on the backside of a silicon substrate, permitting backside patterning for multi-layer structures. Meanwhile, other challenges are raised, such as the protection of the front side of a silicon-on-

insulator wafer during the backside DRIE by using polymer layer, and the removal process of the polymer films.

In this chapter, an improved state-of-art microfabrication process integrating a thin-film PZT layer with complex multi-layer silicon structure is performed to overcome the limitation of the previous microfabrication process flow. Other challenges related to the protective polymer layer are also solved. The basics of thin-film PZT processing and the limitation of previous processes are presented in Section 2.2, the improved process development of oxide trench barriers for thin-film PZT devices is presented in Section 2.3, the final processing of PZT devices are presented in Section 2.4, and the summary and conclusion are presented in Section 2.5.

2.2 Basics of Thin-Film PZT Processing and Limitation of Previous Microfabrication

The standard layers of most thin-film PZT micro-devices are the PZT layer itself, an insulating base layer (usually silicon dioxide) and top and bottom electrode layers. The base silicon dioxide layer provides an insulating intermediate layer between the bottom electrode and the silicon substrate, as well as a uniform surface on which high-quality PZT may be deposited. The top and bottom electrode layers are required because, unlike other smart materials such as titanium nickel shape memory alloy (TiNi) [67], piezoelectric films require two electrodes to generate an electric field. In some cases, a top gold layer may be included [24] which converts the contraction in the lateral direction of PZT thin film to out-of-plane deflection; this is due to the gold layer shifting the location of the neutral axis of the thin-film stack above the midline of the PZT layer.

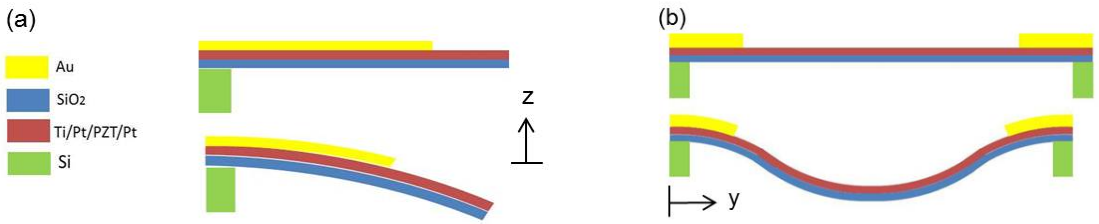

Fig. 2.1 Schematics of thin-film PZT actuators: (a) before and after actuation of the vertical actuator, (b) before and after actuation of the lateral actuator

Once the thin-film stack is presented, it can be patterned into various geometries on a silicon substrate. For example, the silicon layer underneath thin-film stack may be partially or completely removed to form various movable structures driven by PZT actuators. Depending on the applications, different geometry and clamping conditions are applied to the piezo-MEMS devices: from a simple cantilever to a fully clamped membrane or partially clamped diaphragms [10]. For piezoelectric cantilevers, the standard mechanisms are bend-up unimorphs, bend-down unimorphs, or combinations of both. Figure 2.1 shows the cross section of a bend-down unimorph, also referred to as a vertical actuator, in (a), and a lateral actuator which is a combination of bend-up and bend-down unimorphs in (b). In Figure 2.1 (a), a unimorph segment consists of thin-film PZT (0.8μm) as an active layer, top platinum (0.15μm) and bottom platinum (0.08μm) as electrode layers, and gold (1μm) and silicon dioxide (0.17μm) as inactive top and bottom layers. A downward bending moment is generated about the neutral axis when the PZT layer contracts laterally in response of the applied electric field parallel to the remnant polarization. In Figure 2.1 (b), a thin-film PZT lateral (in-plane) actuator is designed in such a way that two standard, downward-bending unimorph segments of the PZT with both the gold and silicon dioxide (SiO_2) structural layers are located at the ends of the

actuator, and two segments with only the SiO_2 structural layer are located at the center of the actuator [24]. This results in an upward bending moment in the center of the structure. The combined structure produces net motion of the tip of actuator in the lateral direction. Furthermore, due to its curved shape, such an actuator produces larger displacements than pure contraction of the PZT thin-film alone.

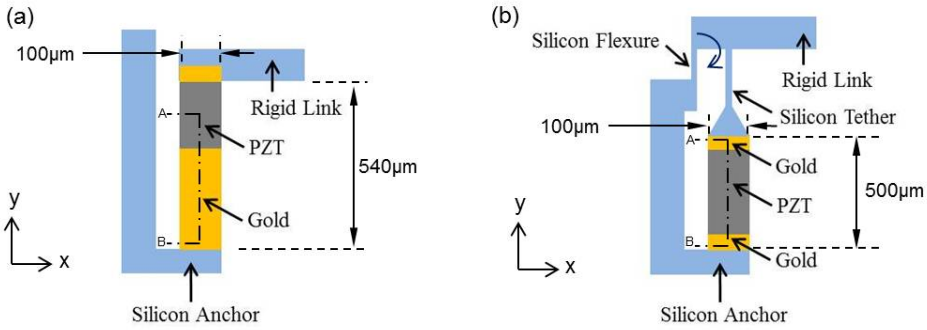

Fig. 2.2 Structure of a single thin-film PZT actuator structure in proposed applications: (a) vertical actuator unit, (b) lateral actuator unit

For the proposed applications in this dissertation, thin-film actuators are connected to other silicon components that can move with respect to a silicon substrate as shown in Figure 2.2. The cross sectional views of the line A – B shown in Figure 2.2 correspond to Figure 2.1 (a) and (b), respectively. Figure 2.2 shows that one side of the thin-film actuators is connected to a silicon anchor, while the other side is connected to a rigid link for the vertical actuator, or a silicon tether for the lateral actuator. The silicon tether transmits the force from the thin-film PZT lateral (in-plane) actuator to moving silicon components. A silicon flexure is a structural rotational spring, which is fixed at the silicon anchor and is deflected as the lateral actuator produces the motion. For higher force or larger displacement operation, multiple thin-film PZT actuator structures may be

connected in parallel or series, respectively. For example, in a multi degree-of-freedom (DOF) robotic leg presented in Chapter III, ten vertical actuators are connected in parallel for large weight capacity, and eight lateral actuators are connected in series for large rotational displacement.

The original microfabrication process for thin-film PZT actuators is shown in Figure 2.3 [24]. The substrate used for fabrication is a silicon-on-insulator wafer (SOI). The silicon-on-oxide wafer is coated with silicon dioxide as the base layer for a PZT thin-film (Fig. 2.3A). Then thin film layers of titanium (Ti) and platinum (Pt) are deposited by sputtering, and PZT thin film layer is deposited by sol-gel (Fig. 2.3B). The layers of top electrode (Ti/Pt) and PZT are patterned using two argon ion-milling steps, and contact vias for the electrical connection are next opened to the bottom Pt layer by a wet etch (Fig. 2.3C). Next, gold (Au) is deposited by a standard metal lift-off process (Fig. 2.3D).

After material deposition, additional micromachining is performed to create movable structures. First, the silicon device layer of the SOI wafer is patterned and etched down to the buried oxide layer through deep reactive-ion etching (DRIE) process, followed by short oxide RIE and DRIE steps to continue etching slightly past the buried oxide (Fig. 2.3E). To couple the resulting silicon microstructures defined by the DRIE step to the unimorph thin-film PZT lateral actuator, photoresist encapsulation is performed to protect the silicon microstructures during actuator release. Actuator release is then completed in a xenon difluoride etcher (XeF_2) that undercuts the silicon in the device layer and beneath the PZT unimorph actuators (Fig. 2.3F).

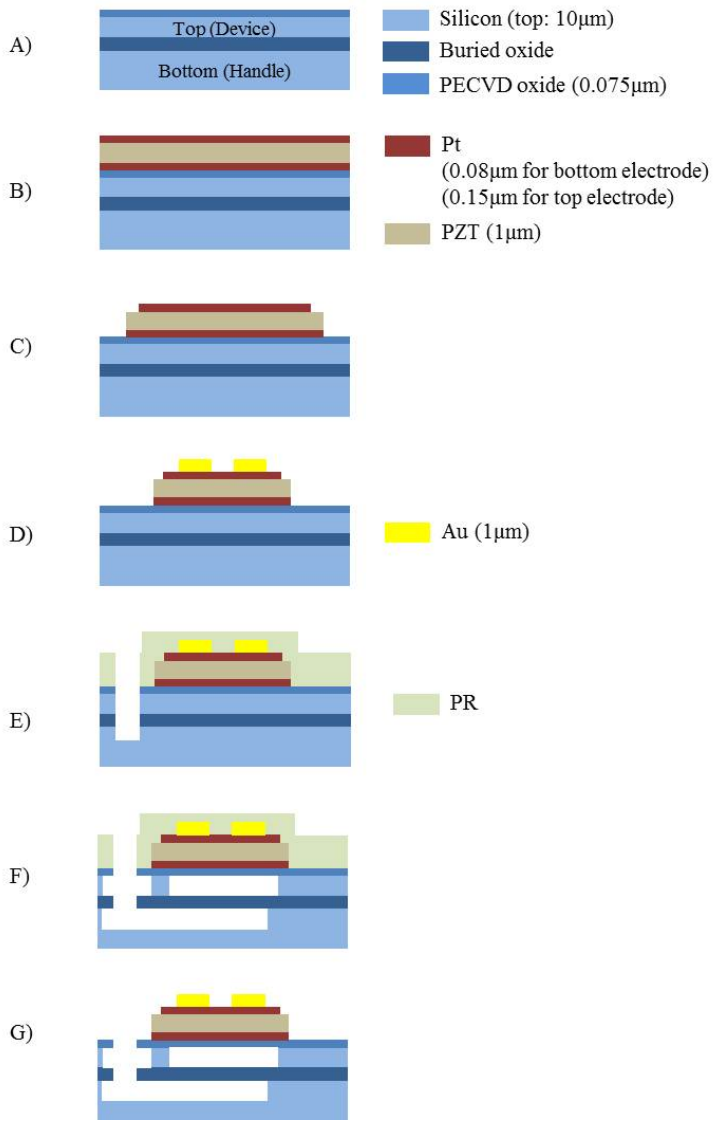

Fig. 2.3 Original process flow of thin-film PZT integrated complex micro-devices (by Oldham et al. [24])

However, this original microfabrication process used to produce lateral and rotational PZT microactuators has various limitations. It is vulnerable to flaws in the photoresist encapsulation layer and cannot handle the wide variation in etch rate of XeF_2 across complex structures with many actuators. It is also not feasible to perform fabrication of multi-layer silicon structures. One desirable multi-layer silicon structure,

obtained in the revised process to be presented, is a released structure that is obtained from both the device layer and the handle layer of a silicon-on-insulator wafer with different geometries of top (device) and bottom (handle) layers.

To elaborate on device release with the original fabrication process, individual actuators were released from underlying silicon with a timed XeF_2 isotropic etch. During this etching process, the photoresist encapsulation layer protects silicon anchor points and other silicon structures. However, spin-coated photoresist on the bulk-micro machined microstructures is prone to having trapped air bubbles (a.k.a photoresist bubbles) near the sidewalls of bulk-micro machined structures. The photoresist is also susceptible to hardening and cracking during long duration processes, such as the XeF_2 release. In addition, since the actuator release by XeF_2 after photoresist encapsulation is an isotropic timed-etch method, this results in over-etching or insufficient-etching defects beneath the thin-film PZT actuators due to significant etch rate variation over complex or large area structures, as shown in Figure 2.4.

The consequences of the above problems are not only to degrade the performance of the single actuator but also to result in uncompleted or failed multiple actuator structures, where actuators are connected in parallel or in series arrays. Once again, an example is the multi degree-of-freedom microrobotic leg presented in Chapter III, which could not be produced by existing methods for thin-film piezoactuator fabrication. In this example, previous fabrication based on the original microfabrication process flow resulted in the loss of silicon connectors between the PZT layer and the silicon tether in the vertical actuators array while uncompleted actuators were still observed in the lateral actuators array during XeF_2 release. Therefore, the previous fabrication process of thin-

film PZT actuator hinders high-yield microfabrication of complex geometry thin-film PZT-actuated devices.

In this chapter, the solution to these limitations is presented in the form of oxide barrier trenches. These are integrated into the previous thin-film PZT process flow to provide much more reliable encapsulation of the silicon connectors at both ends of thin-film PZT actuator and other complex silicon structures. Simultaneously, the oxide deposition provides hard mask layers on the backside of a silicon substrate, permitting backside patterning of multi-layer structures. However, for the backside patterning of the silicon substrate in a silicon-on-insulator wafer, other challenges are raised, such as the protection of the front side of the device during backside DRIE, and the removal of polymer protective layers. But, the improved microfabrication of thin-film PZT layers with complex multi-layer silicon structures is successfully performed, overcoming the limitations of the previous microfabrication process flow.

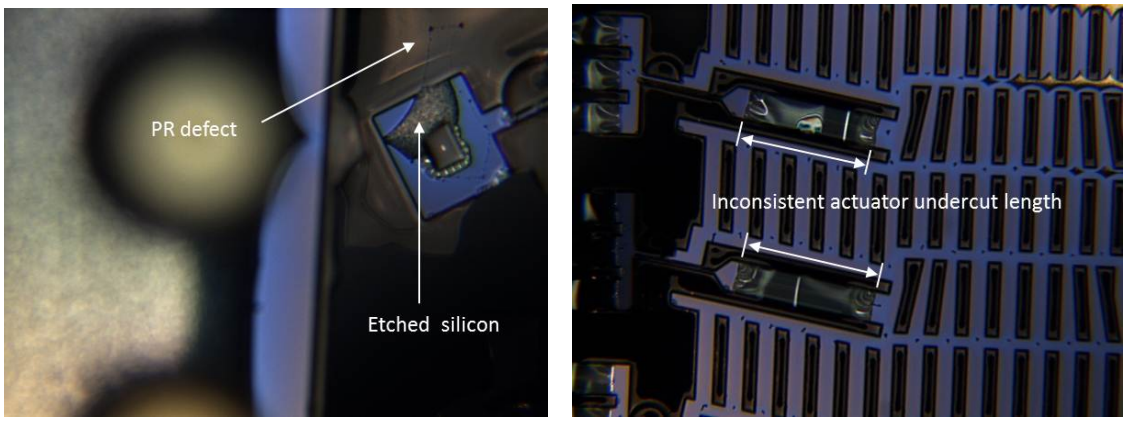

Fig. 2.4 Occasional crack and failure of photoresist encapsulation layer (left) and inconsistent actuator under length (right). Images courtesy of the U.S. Army Research Laboratory

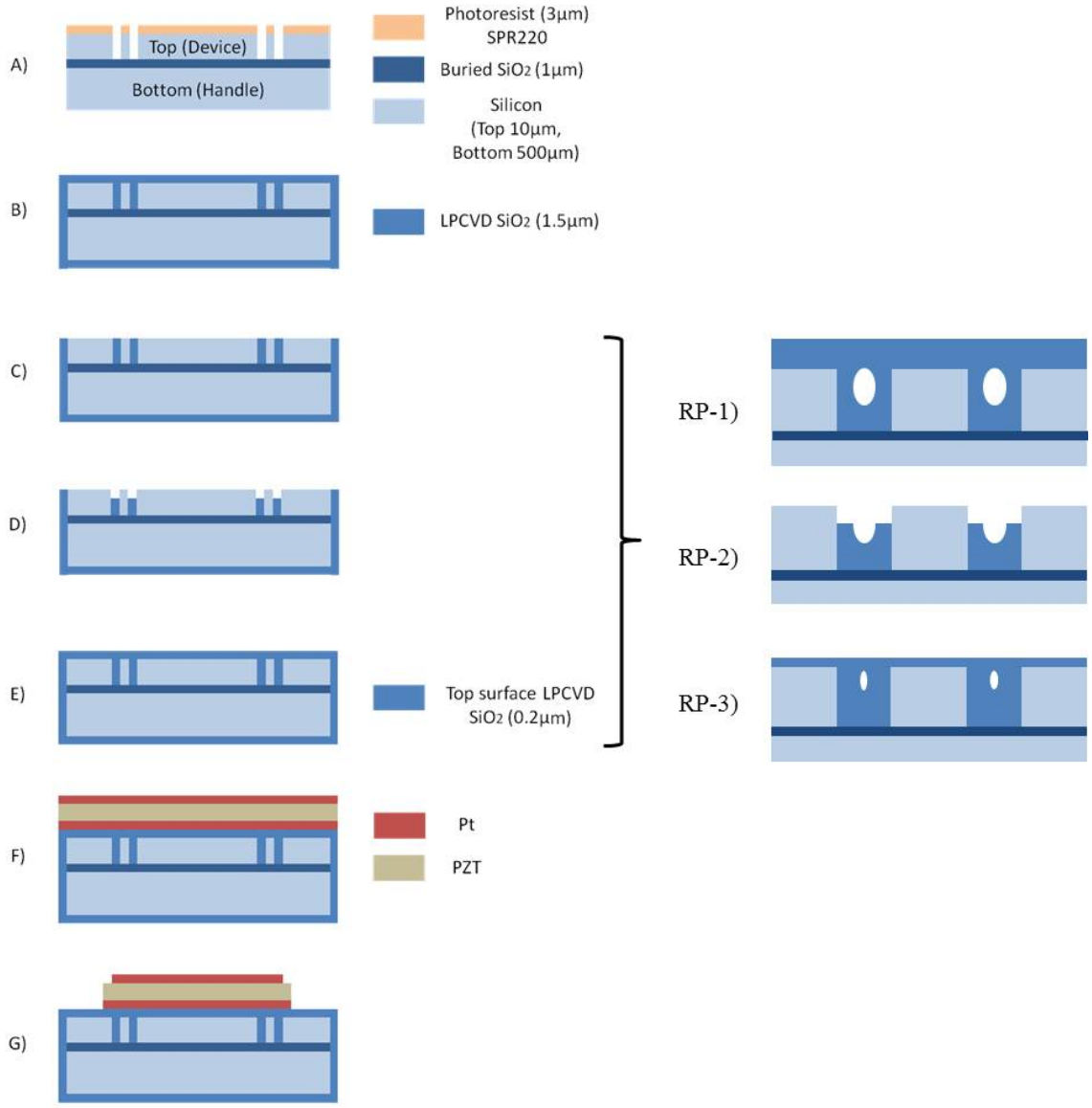

Fig. 2.5 Multi-level microfabrication process flow of thin-film PZT actuated silicon structures: top side process on a silicon-on-insulator wafer

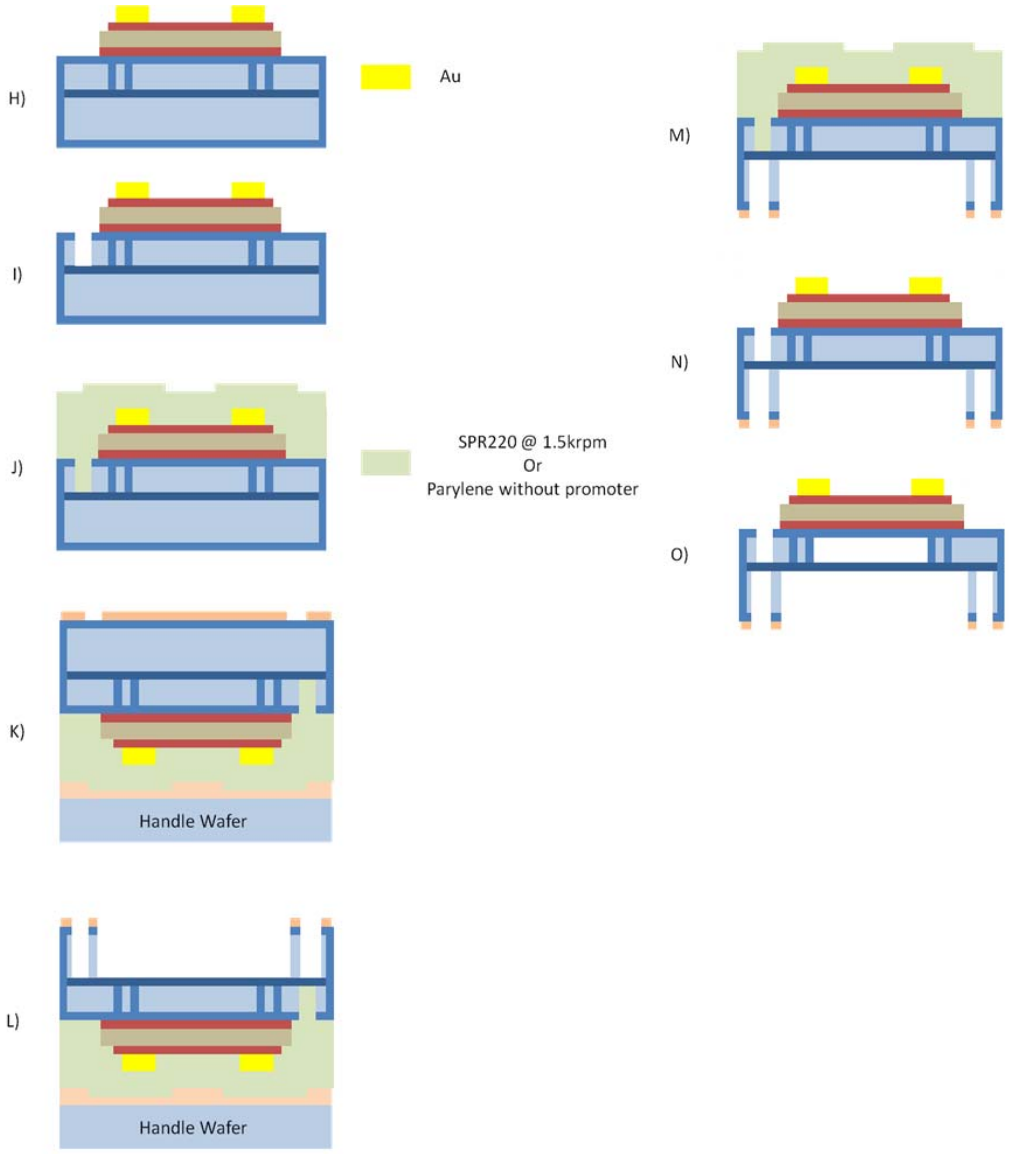

Fig. 2.6 Multi-level microfabrication process flow of thin-film PZT actuated silicon structures: bottom side processing of a silicon-on-insulator followed by XeF_2 release

2.3 Development of Oxide Trench Barriers for Thin-Film PZT Devices

A revised multi-level microfabrication process flow is performed in which deposition of silicon dioxide to fill isolation trenches is included as the earliest process step, in replacement of photoresist encapsulation much later in the process. In IC technology, oxide trenches are used for electrical insulation [64], [65], [66], and previous MEMS structures have used them to separate capacitive electrodes, as in [34]. In the current process, the oxide trenches provide vertical etching barriers against isotropic XeF_2 gaseous etching of substrate silicon device layer underneath thin-film PZT actuators. Thus, they serve as a robust encapsulation structure, also defining the geometry of the devices. Damage to the device layer is minimized during actuator release, and uniform undercut length of PZT/Au unimorph actuator structure is obtained across the wafer. In addition, the oxide deposited to fill the trenches also provides material for a hard mask on the backside of silicon-on-insulator wafers for multi-layer structure fabrication.

Figures 2.5 to 2.6 show the revised process flow for thin-film piezoelectric MEMS devices. To create the trenches along the sidewalls of bulk-micro machined structures, such as flexural springs and silicon connectors, or tethers, from springs to PZT unimorphs, 3μm-wide trenches are etched through the device layer (Fig. 2.5A) to protect the microstructures. Fig. 2.5B shows how pre-furnace cleaned trenches are then filled with silicon dioxide by low pressure chemical vapor deposition (LPCVD).

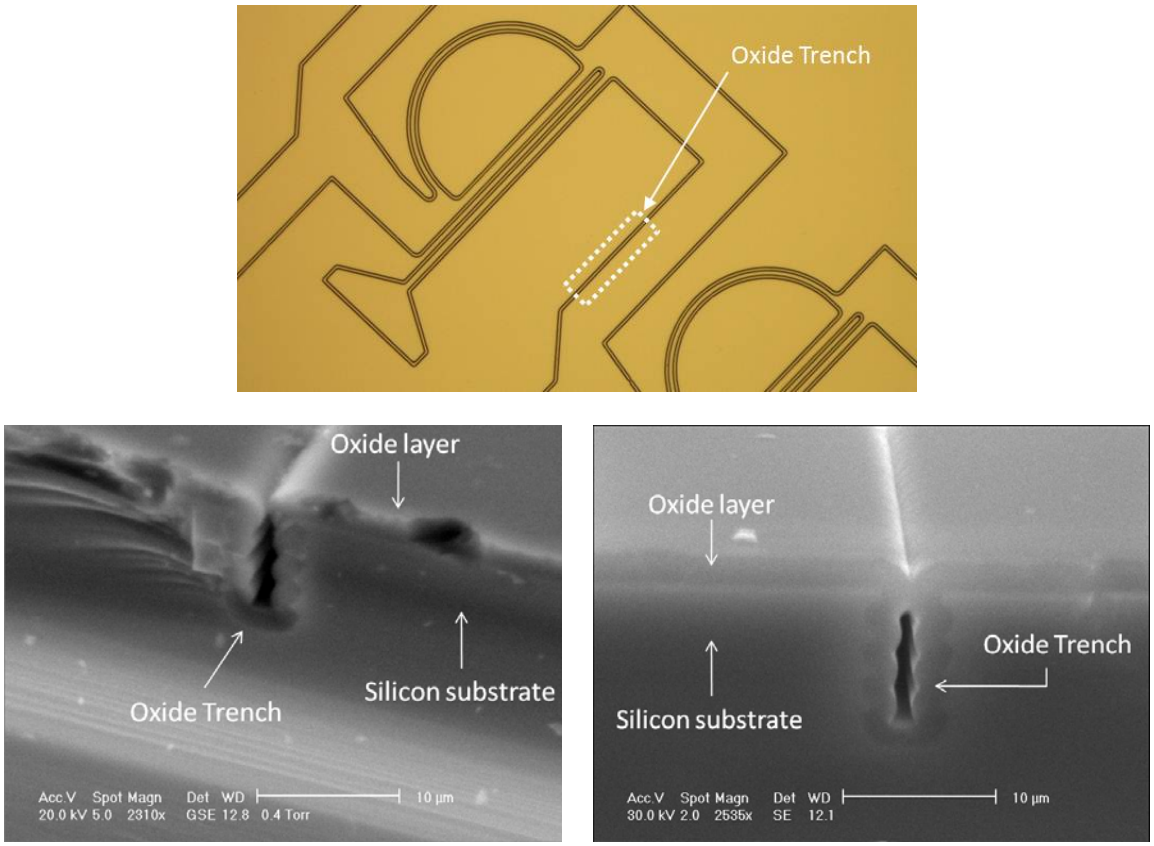

Fig. 2.7 Oxide vertical trench barrier (top) and its cross-sectional view before annealing (bottom-left) and after annealing (bottom right)

However, keyholes are generated in the oxide trenches that complicate barrier trench formation. These keyholes form due to non-uniformity in the trench sidewalls and a slightly faster deposition rate at the trench mouth than inside the trench, as shown in Figure 2.7. Annealing above 1000^0C has been shown in some cases to make oxide reflow in such trenches [68], [83]. However, 1µm wide keyholes could not be closed in the present devices experiment in annealing tests at 1000^0C for approximately 4 hours. Instead, the surface of the oxide is removed by either chemical mechanical polishing (CMP) or reactive ion-etching (RIE), and the upper part of the trench is etched by short RIE (Fig. 2.3 C-D). Figure 2.8 shows cross-sectional images of trenches before- and

after- a short RIE by which the keyhole is opened. After re-opening the keyholes, the LPCVD process is repeated to fill the opened trenches (Fig. 2.3E). Several iterations of steps B – D help diminish the size of the keyholes but it is difficult to eliminate them entirely. In Figure 2.5, the process steps labeled as RP-1 to PR-3 show the schematic evolution of keyholes during oxide filling and refilling steps.

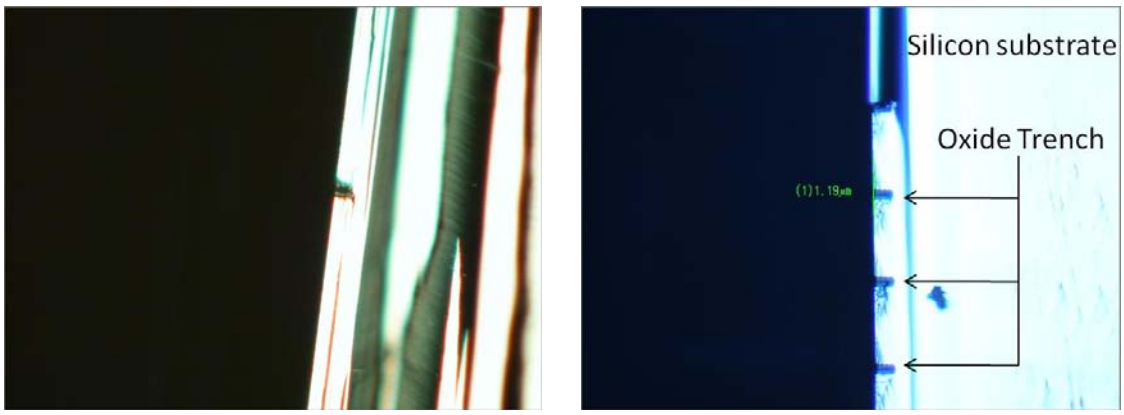

Fig. 2.8 Reactive ion etching to open key hole mouth: before (left) and after (right) RIE

Once keyholes are adequately closed, the surface of the wafer is planarized. This is done because sol-gel thin-film PZT deposition requires a very flat surface of the base layer for PZT deposition, silicon dioxide in this work, to avoid the failure or degradation of thin-film PZT layer during microfabrication and actuator operation. Therefore, the step after trench fabrication was to polish the surface of the top of the oxide trenches by Chemical Mechanical Planarization (CMP), followed by an optional oxide deposition by PECVD to reach a target thickness of 2000Å. From [91], this thickness of the base oxide layer was optimized for the maximum lateral actuation angle and weight bearing capabilities of the individual thin-film PZT actuator structure shown in Figure 2.2.

Before performing the actual thin-film PZT actuator fabrication, as shown in Fig. 2.3F–H, a test wafer was produced. In this wafer, a dummy gold layer was deposited by lift-off on the top surface oxide, to serve as a dummy actuator in replacement for steps F – H. Then, the silicon microstructure in the top device layer was patterned and deep reactive ion-etched (DRIE) as shown in Fig. 2.3I. Prior to backside etching of SOI wafer, polymer materials were used to protect the microstructure of the top device layer. More details about the protection using polymer materials will be discussed in Appendix A.

Finally, the backside, or handle layer, of the SOI wafer is then patterned. Sample features of the backside structure include micro-robot feet and island connectors of z-axis scanning micro-mirrors. Backside patterning and etching also provide additional open area for XeF_2 to etch the underneath actuators and other unprotected silicon structures (Fig. 2.4O). After backside etching, the protective polymer layer on the top device layer is removed by oxygen plasma. Figure 2.9 shows fully released gold dummy micro-actuators along orthogonal and oblique angles. In the orthogonal image, the etching time was chosen to be 120 cycles with 30 seconds per cycle, and further added with 180 cycles to fully etch the silicon underneath thin-film PZT layer as shown in the oblique image in Figure 2.9. The left image in Figure 2.9 demonstrates that the vertical Teflon passivation layer along the etched silicon by DRIE process prevents XeF2 gas from etching the silicon underneath thin-film PZT layer. This results in an irregular profile of the etched silicon layer underneath thin-film PZT layer when the both sides of the silicon layer of a single actuator are compared.

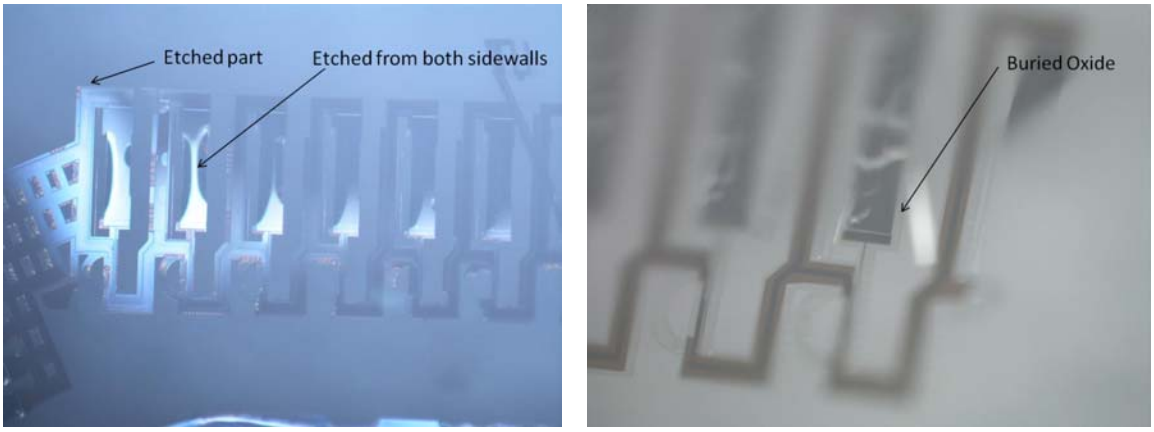

Fig. 2.9 Orthogonal (left) and oblique (right) images of the bottom of dummy actuator: partially finished XeF_2 etching (left) and fully finished XeF_2 etching (right)

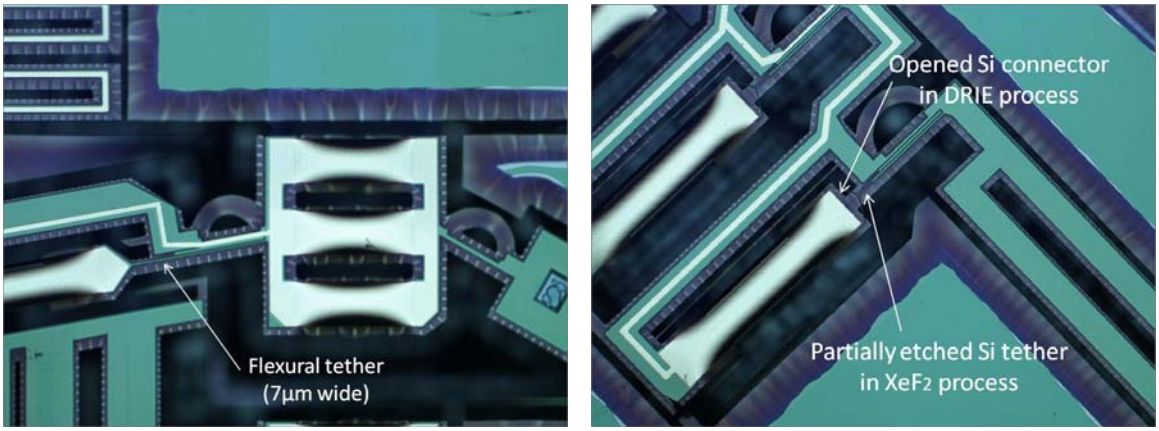

Fig. 2.10 Top view image of the topside of dummy actuator (left) and unprotected silicon connector and partially etched tether (right)

Figure 2.10 shows fully released gold dummy actuator structures from the top of the wafer. The flexure-tether structure that is used for translating contractive actuation of thin-film PZT actuator into rotation of bulk silicon microstructures is well protected and robustly survived XeF_2 etching, as shown in the left image. For contrast, due to a drafting mistake during computer-aided drafting process, the topside of silicon connector between gold dummy actuator and silicon tether is not covered with LPCVD oxide. This results in

the connector disappearing during DRIE (step I), and the part of silicon tether close to the silicon connector is exposed to and etched by XeF_2 gas, as shown in the right image.

2.4 Processing of PZT Devices

Once test monitor wafers with dummy gold "actuators" were successfully fabricated, actual thin-film PZT on SOI wafers were processed up to step E at Lurie Nanofabrication Facility. Then, PZT (with a Zr/Ti ratio of 52/48) and electrode layers were deposited at the U.S. Army Research Laboratory and Radiant Technologies, Inc..

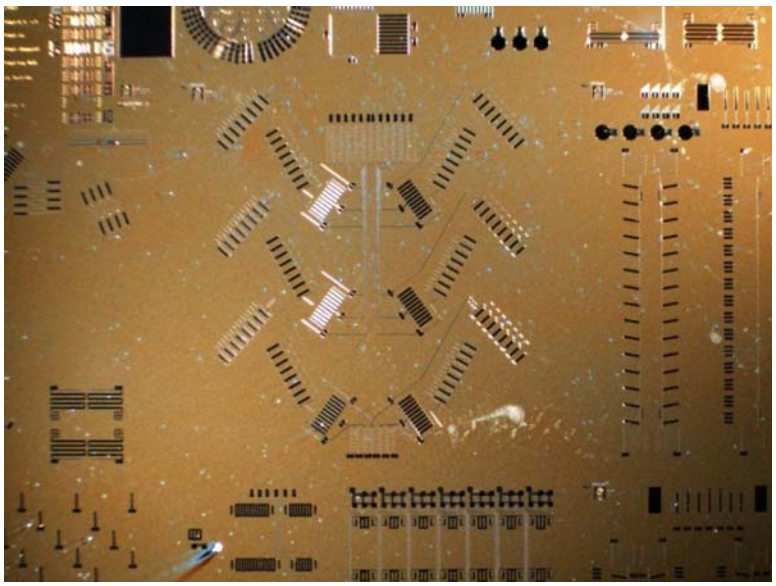

Fig. 2.11 Deposition and patterning of bottom electrode, PZT, and top electrode layers

To complete the PZT stack patterning, two argon milling steps for the top electrode and PZT layer, respectively, and a wet etch for contact vias to the bottom electrode are performed at ARL [24]. A sample die after PZT stack patterning is shown in Figure 2.11. From there, the same process flow up to step O is continued at the Lurie

Nanofabrication Facility. Figure 2.12 shows sample actuators following the gold liftoff process, showing that the structural gold layer is aligned to the PZT and platinum top electrode layer. Once gold is present, it is a well-known processing issue that hardened polymer layers on top of gold are difficult to remove without wet processing. Since the wet etching method to remove residual polymer after backside etching steps is difficult to perform in our process flow due to stiction and the fragility of the actuator devices, a thin oxide protection layer is deposited by PECVD before continuing. This oxide protective layer has good adhesion to gold surfaces and good step coverage, and is performed between steps H and I to protect the top gold surface from hardened polymers, such as photoresist.

The details of the final stages of device processing, namely, backside processing and release, continue at step I. Figure 2.16 shows the photolithography process followed by RIE and DRIE process on the backside of a SOI die (step I). Since a chemically inert Teflon-like passivation layer is deposited during the DRIE process, this vertical layer prevents XeF_2 gas from etching the silicon underneath the material stack. Thus, after removal of chemically inert Teflon-like passivation layer, a uniform undercut length of the PZT/Au unimorph actuator structure is obtained during XeF_2 under-etching process of thin-film PZT actuator and silicon microstructure layer. Figure 2.17 and 2.18 show the etching status of vertical actuators of multi-DOF robotic leg and of in-plane actuators of hexapod robotic leg. This illustrates that the silicon device layer underneath the PZT stack is gradually etched.

Several completed devices are shown to illustrate the successful completion of the proposed microfabrication process. Figure 2.19 shows a backside view of fully undercut

PZT actuators from a translational z-axis focusing stage and of a compact actuators array from a multi-DOF leg, both taken from the backside of SOI die. Figure 2.20 show the frontside view of the entire four-folding z-axis focusing stage and multi-DOF leg before the top protective oxide layers are removed. Figures 2.21 and 2.22 show the scanning electron microscopic image of the fully released multi-DOF robotic leg and translational z-axis focusing stage.

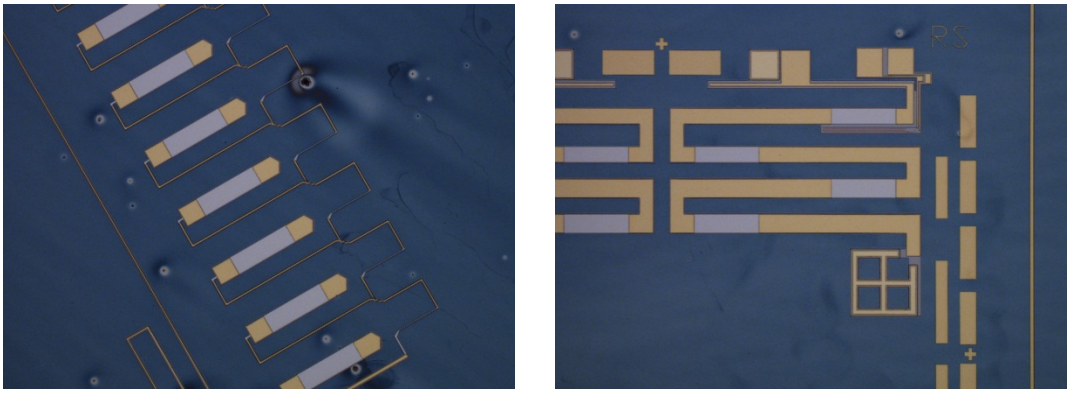

Fig. 2.12 Au liftoff process: In-plane actuators in the micro-robotic leg (left) and out-of-plane actuators in the translational z-axis focusing stage (right)

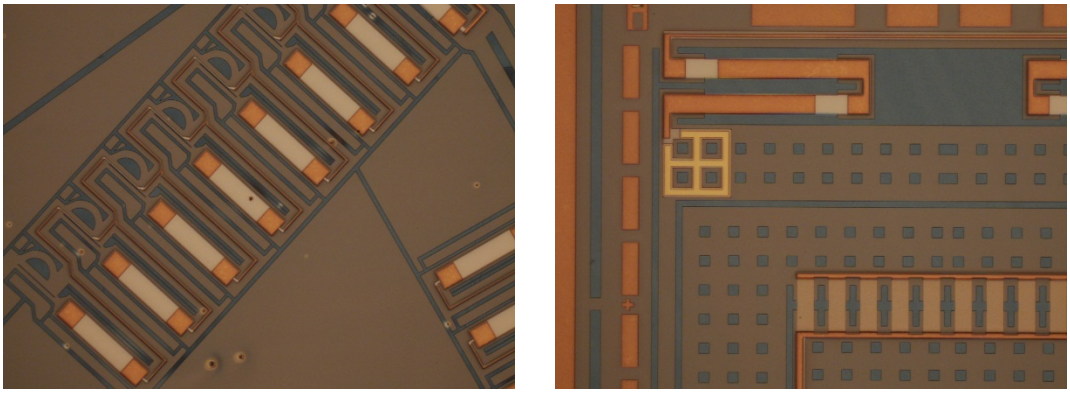

Fig. 2.13 Photolithography process on the top of SOI die: In-plane actuators in the micro-robotic leg (left) and out-of-plane actuators in the translational z-axis focusing stage (right) after develop in H_20:AZ400K 1:3

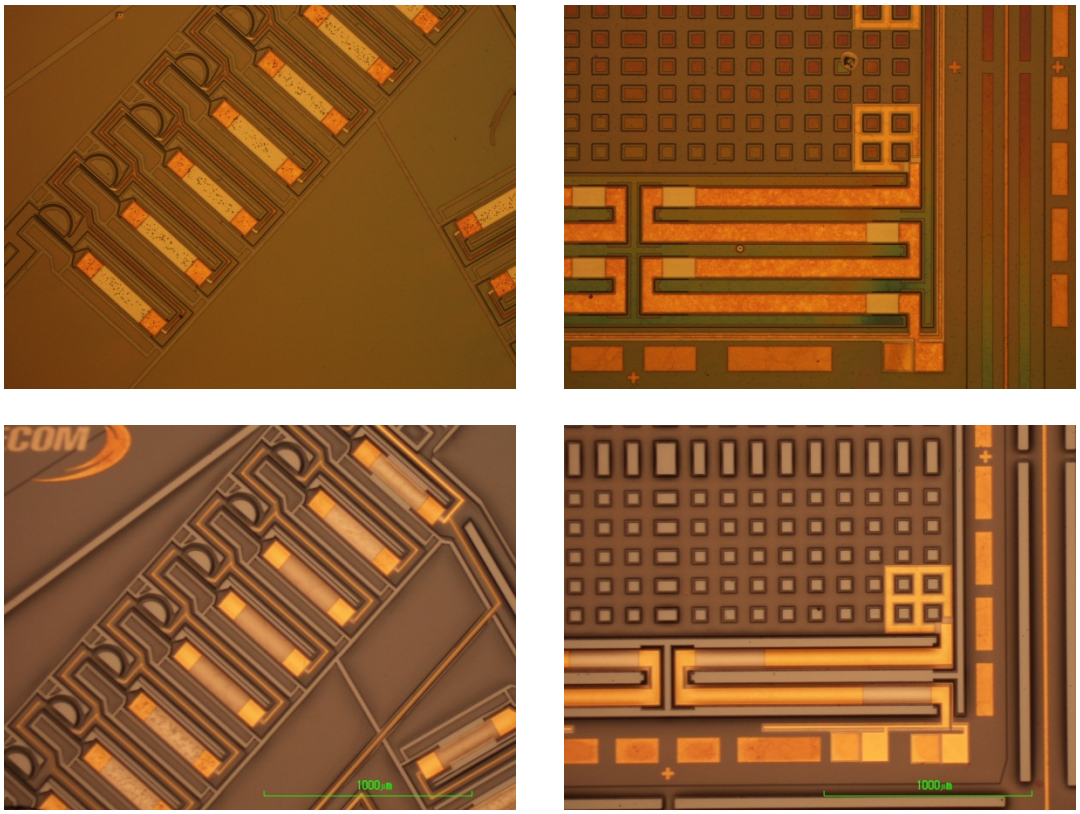

Fig. 2.14 Partially removed top oxide layer (top images) and fully removed top oxide layer (bottom images): In-plane actuators in the micro-robotic leg (left images) and out-of-plane actuators in the translational z-axis focusing stage (right images)

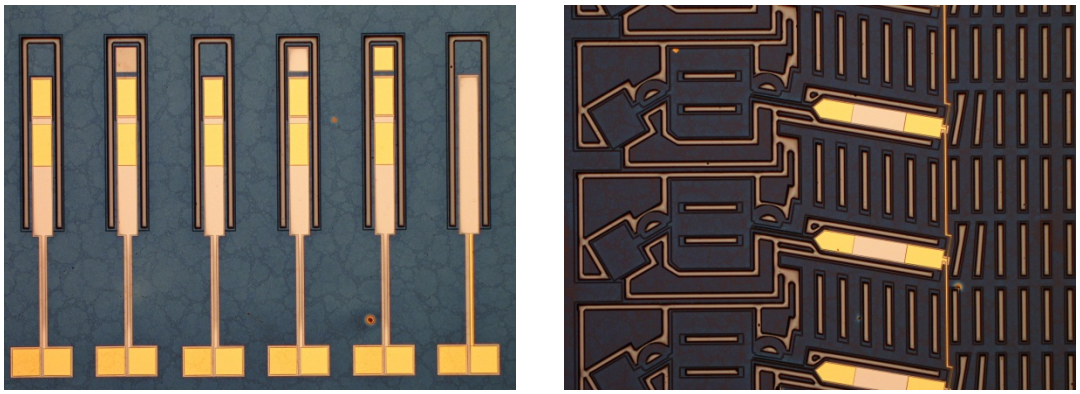

Fig. 2.15 Bosch process followed by removal of photoresist mask layer: test cantilevers for piezoelectric coefficient measurement (left), and millipede micro-robotic legs (right)

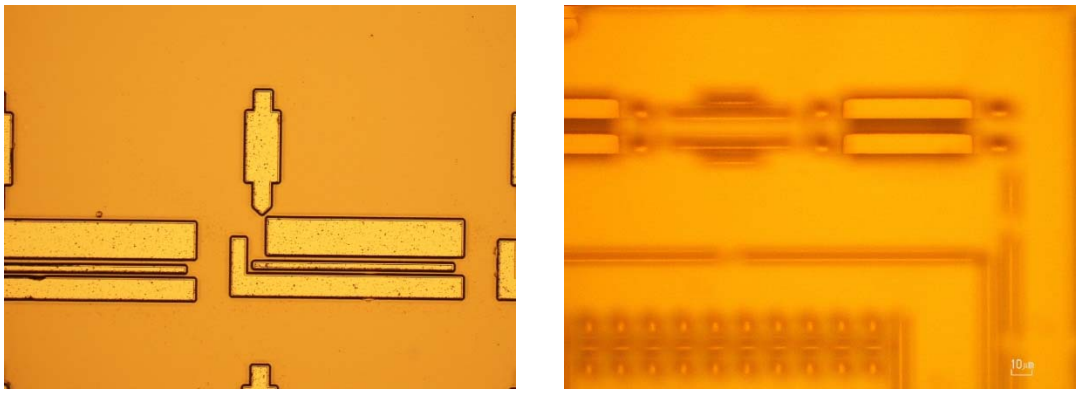

Fig. 2.16 Photolithography process followed by RIE process (left), and DRIE process (right) on the backside of a SOI die

Fig. 2.17 Backside image of vertical actuators of multi-DoF robotic leg after 15-minute (left) and 30-minute (right) XeF_2 Etching

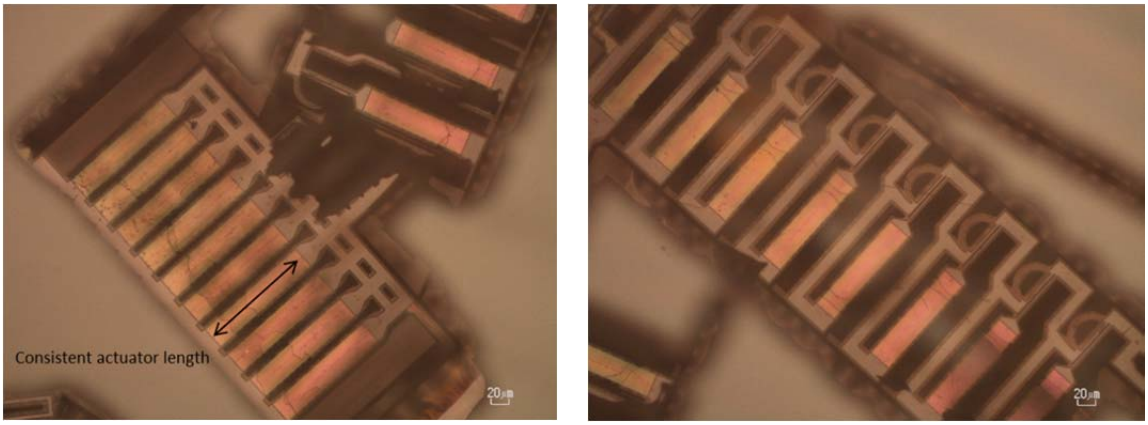

Fig. 2.18 Backside image of vertical actuators of multi-DOF robotic leg after completed XeF_2 etching (left) and backside image of in-plane actuators of hexapod robotic leg after completed XeF_2 etching (right)

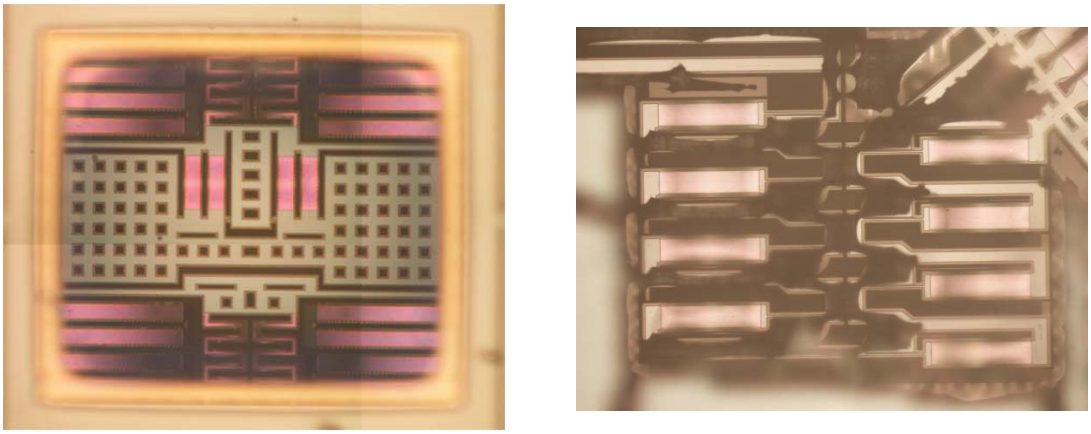

Fig. 2.19 Image from Backside: Z-scanner (left), Multi-DOF leg (right)

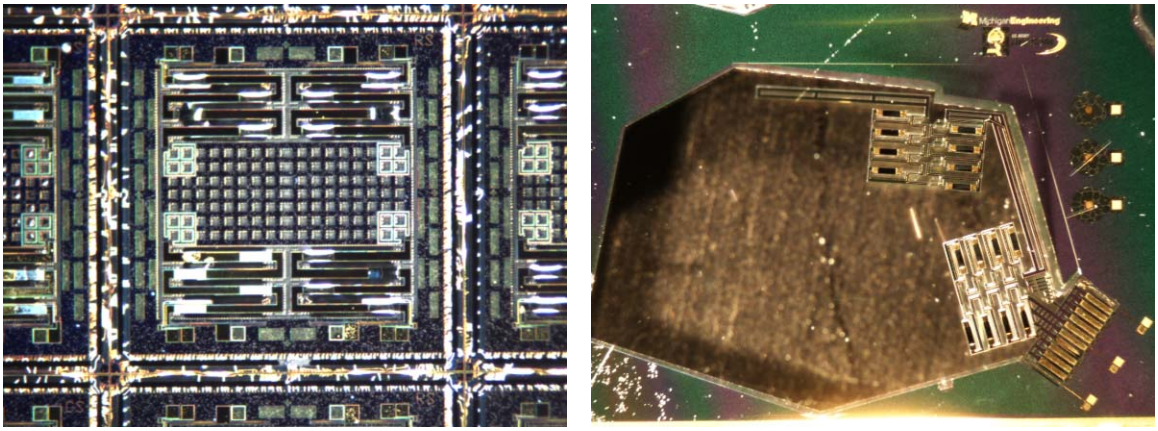

Fig. 2.20 Four-folding z-axis focusing scanner (left) and a multi-degree of freedom leg (right) before the top protective oxide layers are removed

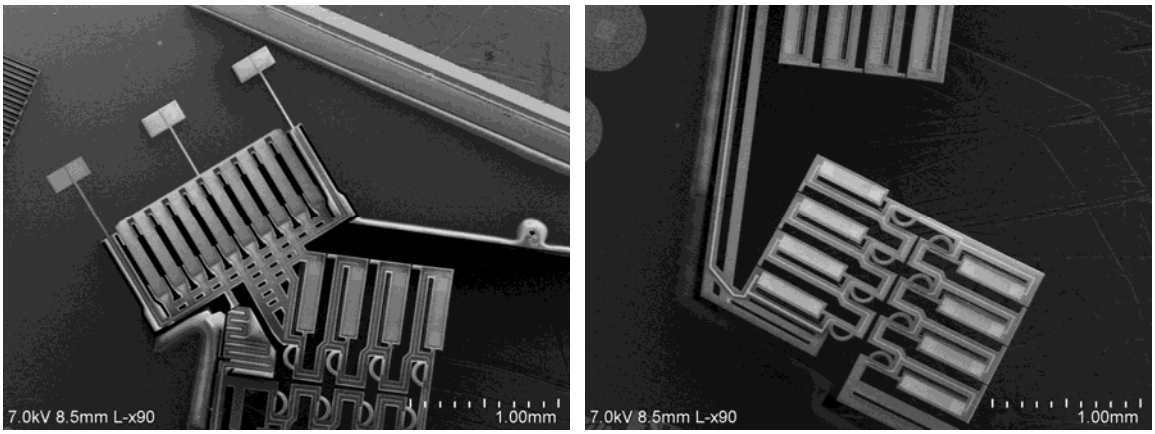

Fig. 2.21 Scanning electron microscopic image of multi-degree of freedom robotic leg

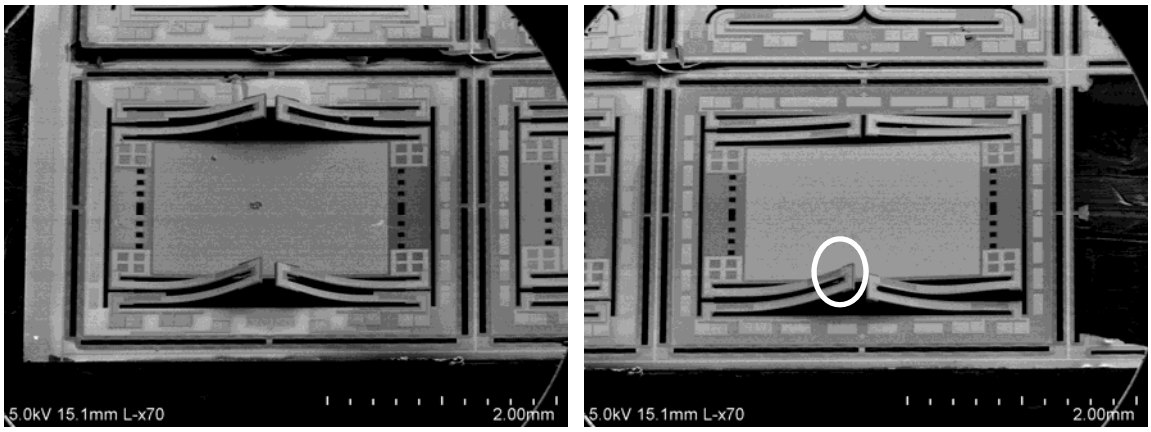

Fig. 2.22 Scanning electron microscopic image of translational z-axis focusing stage

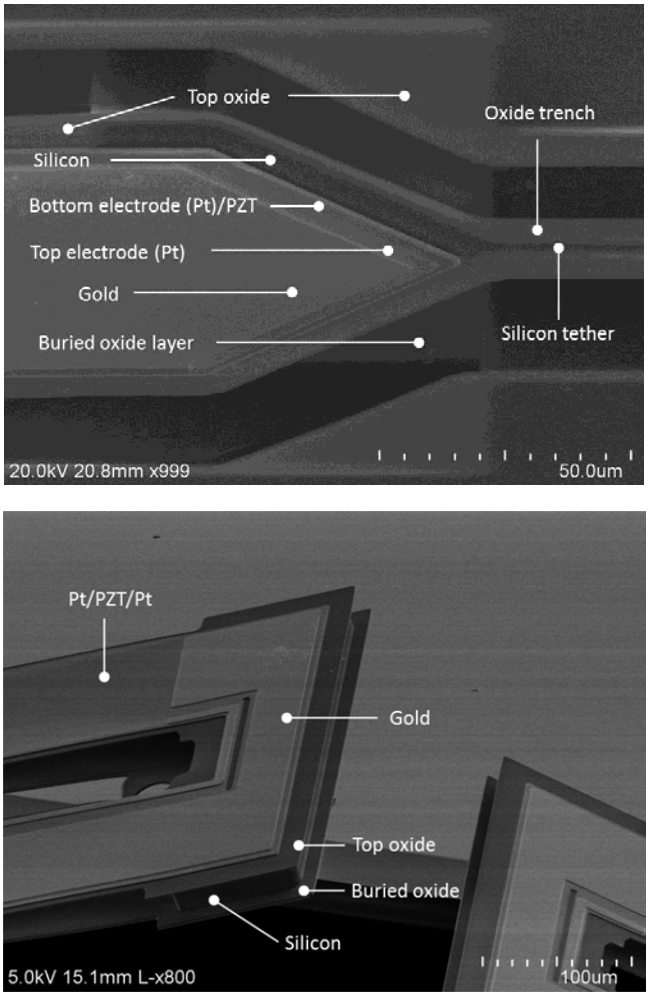

Fig. 2.23 Scanning electron microscopic image of thin-film PZT lateral (top) and vertical (bottom) actuator structure produced by the multi-level microfabrication technique

Figure 2.23 shows the layers of thin-film PZT actuator structure. The top image in Figure 2.23 shows the one area of the thin-film PZT lateral micro-actuator structure that the stack of the top gold, top electrode, PZT, bottom electrode, and the base oxide layer is connected to the silicon connector and the tether as shown in Figure 2.1. The bottom image in Figure 2.23 shows the area of the folded actuator highlighted in a white circle shown in the right image in Figure 2.22.

One final difficulty was encountered during release of the above devices. It was observed that process variation of the recipe parameters, high process temperature generation and insufficient heat dissipation during backside DRIE processing can cause a thick Teflon-like passivation layer during step I. This may then harden into a residual polymer layer along silicon sidewalls during step L. Even though these vertical polymer layers can be partially removed by standard "descum" processing with low pressure oxygen plasma process with SF_6in an inductively coupled plasma (ICP) process tool, much of the residual layer on the sidewall still remained. This caused irregular silicon etching or prevents XeF_2 gas from etching the silicon during step O in the first devices produced by the process described. To elaborate, two-hour multiple SF_6 etching steps were performed at various pressures with O_2 ashing among the etching steps, and XeF_2 etching was conducted. The teflon-like passivation layer along the edge of top oxide and buried oxide layer was still observed, as shown in Figure 2.24, though XeF2 was able to irregularly etch the silicon underneath the PZT layer. To solve this problem, a high temperature oxygen plasma at 200^{o}C for 15 minutes was developed to remove the vertical polymer layers between steps N and O. When this is done, the PZT layer is successfully undercut at a uniform rate, as shown in Figure 2.25.

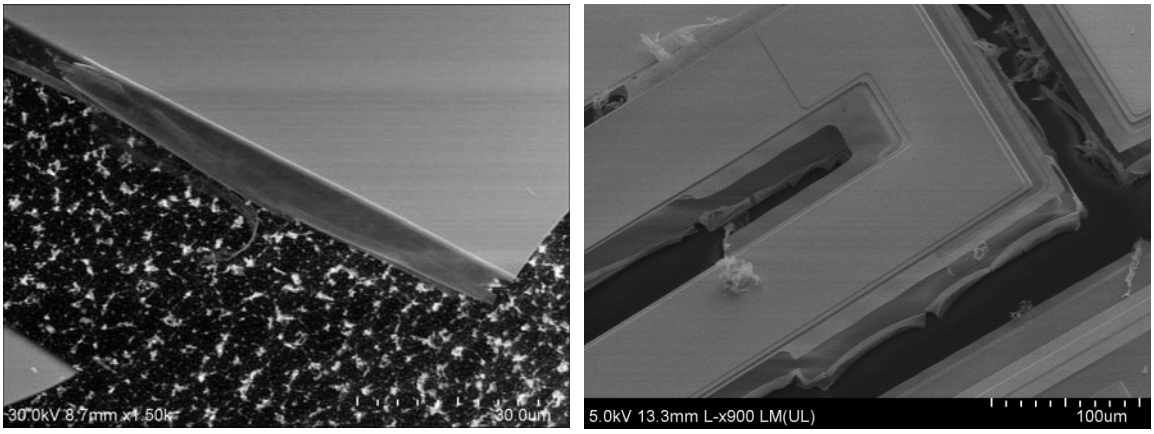

Fig. 2.24 SEM image of CF_x passivation layer along silicon sidewall

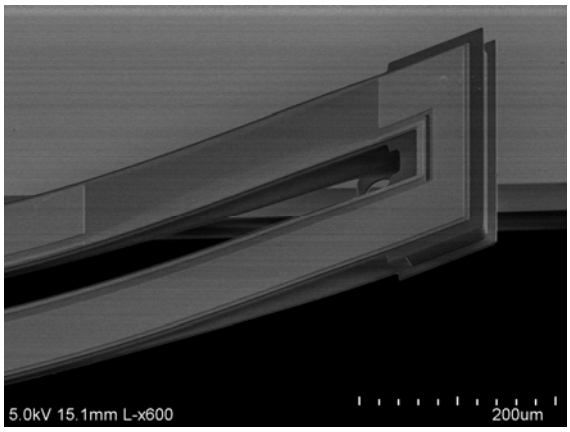

Fig. 2.25 200^{o}C oxygen plasma process followed by XeF_2 etching

One major limitation of the finalized process flow is an inability to remove the oxide trenches following XeF_2 release. While this was originally intended via isotropic reactive-ion-etching (RIE) of silicon dioxide, and structures were designed with removal of silicon dioxide expected, in practice the top platinum electrode on the PZT layer was found to be eroded in such an RIE step, removing electrical connection to most actuators. Thus, flexible structures in the device layer are wider than originally designed by the oxide trench width, and some flexible electrical interconnects (such as that providing

power to the outer actuators) are also reinforced. For example, this reduces range-of-motion of the final micro-robotic leg structures compared to their designed specifications, and future devices should take oxide trench width into account in the design stage. In addition, residual stresses in the metal-stack result in the vertical actuator array having a non-zero neutral position, which leads to variation in vertical displacements from planar neutral position which would be expected from an initially flat structure.

2.5 Characterization of Piezoelectric Performance and Yield

Following fabrication, simple cantilever beams were used to verify piezoelectric coefficient magnitudes as in [82]. Since the piezoelectric coefficient, $d_{31,eff}$, represents the contractive displacement along the lateral direction at given input voltage, it is important to keep this coefficient minimally affected during the revised microfabrication process for the piezoelectric actuation performance, even though piezoelectric coefficients are often very sensitive to the underlying substrate. Since a randomly oriented polycrystalline structure is present in PZT thin film after fabrication, a poling treatment is required to align the scattered poly-domain structure into a meta-stable alignment in the direction of an applied electric field to form a consistent remnant polarization of the layer. The poling test was performed at 250kV/cm (i.e. 20V) using a direct-current power supply at room temperature is used for 45 minutes. After poling, the static vertical displacement of the tip of cantilever was measured by optical profilometry while stepping down to 0V in 1V decrements and returning back to 20V in 1V increments as shown in Figure 2.26.

Due to intrinsic residual thin film stress following fabrication, the piezoelectric coefficient is experimentally determined from radius of curvature of the beam, ρ, in the

Bernoulli-Euler equation with the superposition of the resultant moment due to the residual stress and the moment generated by PZT thin film in Eq. 2.1:

$$\frac{1}{\rho} = -\frac{M_{\text{residual}} + M_{PZT}}{(EI)_1} \tag{2.1}$$

where $M_{residual}$ is the moment due to residual stress of the films, M_{PZT} is the moment generated by PZT actuator, $(EI)_1$ is the vertical composite rigidity of the material stack without Au deposition. Figure 2.27 shows the estimated, field-dependent effective electro-active strain coefficient $d_{31,eff}$ of the piezoelectric cantilevers with and without oxide barrier trenches. Multiple measurements have been performed at each applied electric field and represented as error bars, and the electro-active $-d_{31,eff}$ for both test cantilevers at higher voltages are determined in the range of 60 – 80 pm/V. The variation of measured $d_{31,eff}$ with respect to electric field is observed to be inversely proportional to the applied electric field as deflection due to intrinsic residual stress is predominant at low voltage and the piezoelectric coefficient is approximately inversely proportional to electric field. The empirical $d_{31,eff}$ coefficients in Figure 2.27 show that the performance of fabricated actuators could be preserved in the proposed microfabrication process, especially at high voltages where typical operation occurs.

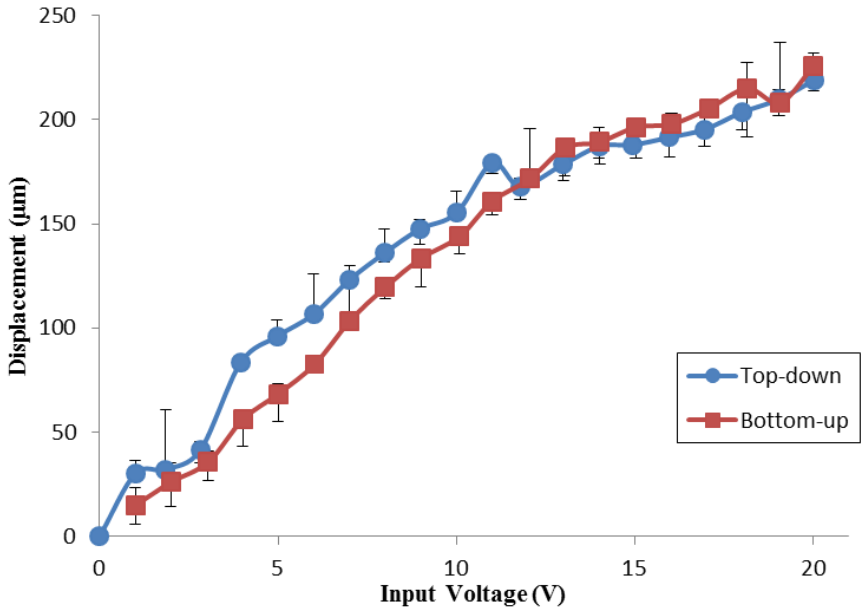

Fig. 2.26 Measurement of the end tip displacement of 750 µm long piezocantilever with oxide barrier trenches

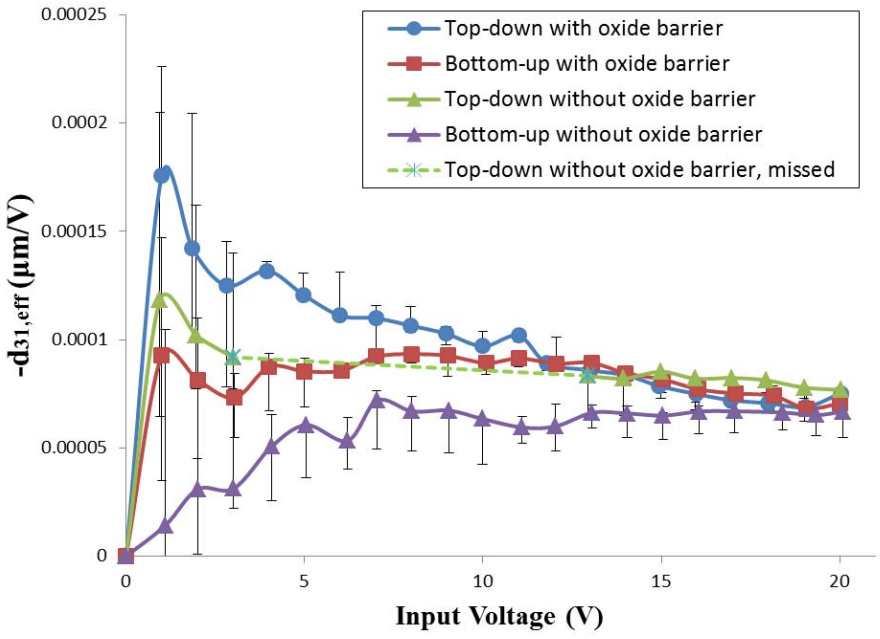

Fig. 2.27 Empirical effective electro-active piezoelectric strain coefficient curve at applied voltages.

In addition to the piezoelectric performance test, the yield of the microfabrication presented in section 2.4 was also measured. For the complex geometry devices with numerous thin-film PZT actuators, such a multi-DOF microrobotic leg, it is important to have the revised microfabrication reliable and to increase the yield rate for those numerous thin-film PZT actuators, compared to the previous microfabrication process. Single thin-film PZT actuator structures, of the type shown in Figure 2.1, were tested, and the yield comparison between the original fabrication process and the oxide trench barrier integrated fabrication process are shown in Table 2.1 and 2.2.The index for yield comparison was selected as:

$$\%\text{Yield} = \frac{\text{Number of undamaged and functional actuators in a chip}}{\text{Number of total actuators in a chip}} \times 100\% \qquad (2.2)$$

Results of the yield analysis on dies of 40-50 actuators from the original and revised process are shown in Tables 2.1 and 2.2. In Table 2.1, functionality of those devices that were attacked by XeF_2 due to photoresist encapsulation failure or pinhole failure on the base oxide layer under PZT thin film that protects the silicon structure from XeF_2 was considered as Not-Determined (N.D.) although the actuators were functional. In Table 2.2, the surface of the top gold layer or of the top platinum electrode was scratched for some devices and also resulted in those devices being considered as Not-Determined. The results show that the yield rate defined in Eq. 2.2 is 57% from Table 2.1 and is 78% from Table 2.2. Figure 2.28 shows the yield rate comparison between the previous original fabrication process by photoresist encapsulation and the improved

fabrication process by oxide barrier trench encapsulation approach, although the comparison result remains conservative as it is obtained from the sample actuators in a chip of the entire SOI wafer.

Moreover, the yield within complex devices is shown to be improved when compared to the device fabricated by revised microfabrication process flow. Within a microdevice actuated by numerous thin-film PZT actuators, the silicon tethers connected to the silicon connector of thin-film PZT actuator were lost during XeF_2 in the previous process due to variation in etch rate across the large device. This is shown in Figure 2.29. In contrast, all silicon tethers were intact after XeF2 in several micro-robotic leg joints with more than 20 actuators using the revised process, as shown in Figure 2.20. In one prototype hexapod robot, 5 out of 6 such robot legs were fully intact, an impossibility for the original process flow. Therefore, for even a single thin-film PZT actuated microdevice, the revised microfabrication process flow is found to dramatically reduce yield loss during isotropic XeF_2 gaseous etching.

Table 2.1 Yield of Individual Actuators from Original Fabrication Process

	1	**2**	**3**	**4**	**5**	**6**	**7**
A	Good	Broken	Good	N. D.	Good	Good	Broken
B	Good	Broken	Good	Good	Broken	Good	Broken
C	Good	Broken	Broken	Good	Good	Good	Broken
D	Broken	Good	Good	Good	Good	Good	Broken
E	Broken	Good	Good	Good	Broken	Broken	Broken
F	Good	N. D.	Good	Good	Good	N. D.	Broken
G	Broken	Good	Good	Broken	Good	Good	Broken

Table 2.2 Yield of Individual Actuators from Oxide Trench Barrier Integrated Fabrication Process

	Gold, 30%	Gold, 40%	Gold, 50%	Gold, 60%	Gold, 70%	Gold, 80%
M1	Good	Good	Good	Good	Good	Good
M2	Good	Good	Good	Good	Good	Good
M3	Good	Good	Good	N .D.	Good	Good
M4	Good	N. D.	Good	Good	Good	N. D.
M5	Good	Good	N. D.	Good	Good	Good
M6	Broken	Good	N. D.	Good	N. D.	N. D.

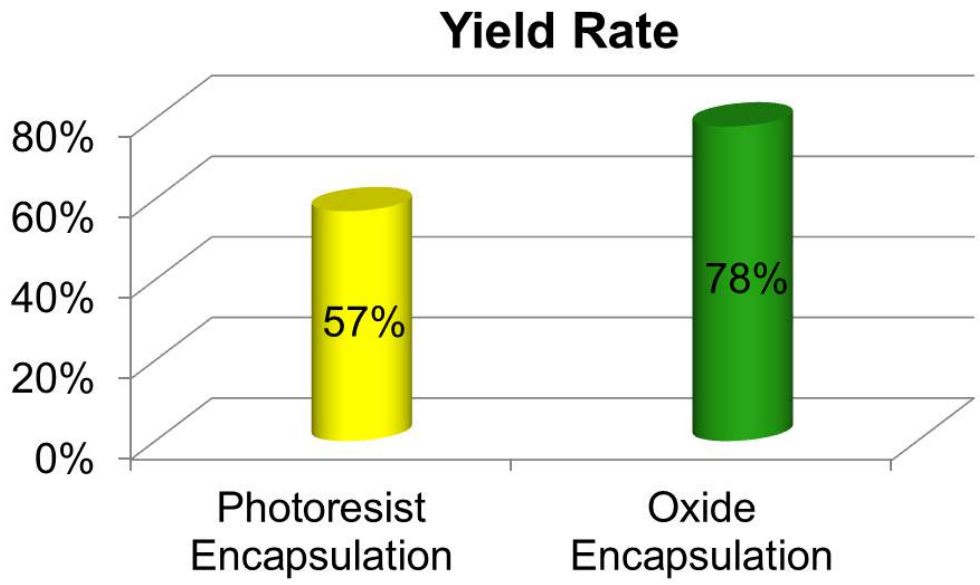

Fig. 2.28 Yield comparison between photoresist encapsulation and oxide barrier trench encapsulation approach

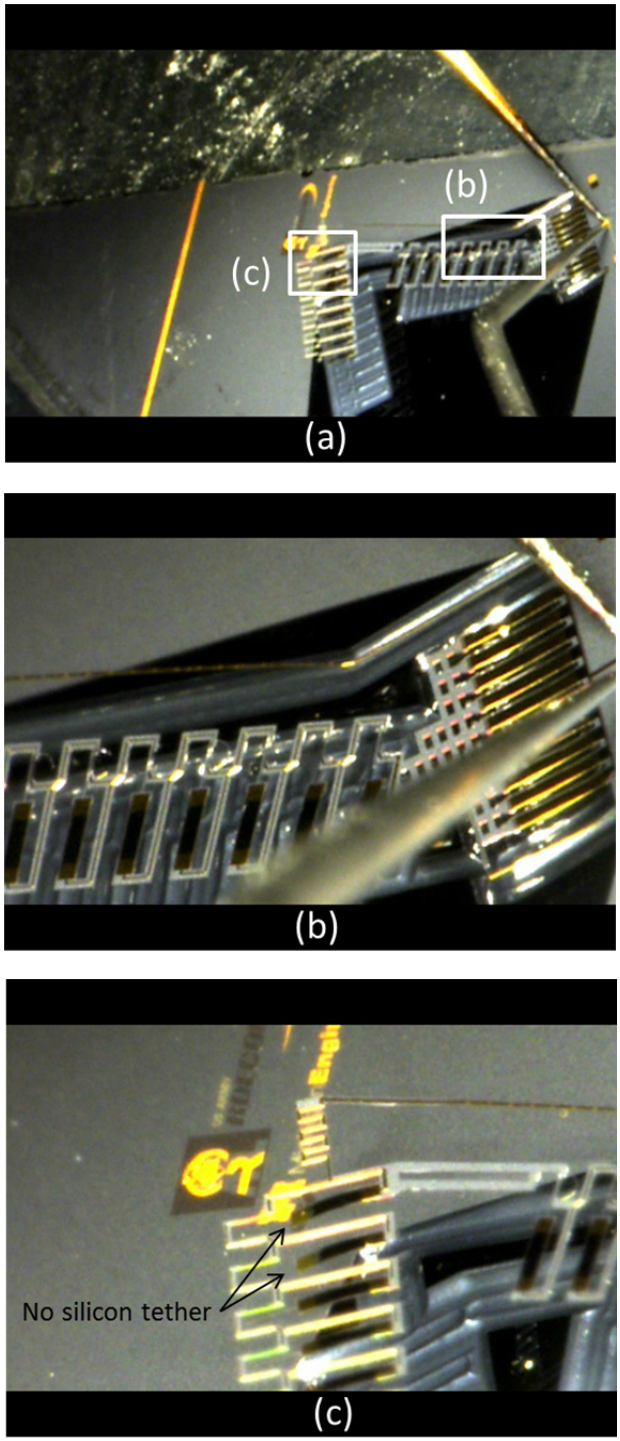

Fig. 2.29 A multi degree-of-freedom microrobotic leg fabricated by original microfabrication process: (a) the entire microrobotic leg, (b) the inner in-plane actuators array with intact silicon tether, (c) the outer in-plane actuators array with no silicon tether left after XeF_2 etching followed by photoresist encapsulation layer removal. Images courtesy of the U.S. Army Research Laboratory

2.6 Summary and Conclusion

Complex PZT processing with oxide barrier trenches was described in this chapter. Due to the chemical inertness of silicon oxide against XeF_2 gas, the complex geometry of silicon structures of the proposed applications was successfully protected and released with high yield rate compared to the devices manufactured by a previous photoresist encapsulation fabrication process. The performance of the piezoelectric devices was tested by measuring the curvature of the test piezo-cantilevers, and was found to be preserved in the revised microfabrication process. With various device designs completed, such as the multi-degree-of-freedom micro-robotic leg and various vertical translational z-axis focusing stages, it is shown that multiple piezo-MEMS applications can be produced with the proposed microfabrication process flow. Furthermore, these devices can achieve multi-layer geometries (front- and backside silicon structural patterning) that were impossible with previous fabrication procedures. Although other processing variability remains that influences the overall device functionality, such as residual stress of in PZT stack and the presence of the base oxide layer, the persistence in the actuator undercut length and the protection of complex geometry of silicon structures in thin-film PZT actuator application is considered a major achievement.

CHAPTER III

Modeling and Characterization of Multi Degree-of-Freedom Thin-Film PZT Leg

3.1 Introduction

Micro-robots are a frequently-discussed potential application of highly engineered microdevices, synthesizing microactuators, sensors, and processing circuitry [73]. Several previous researchers have demonstrated MEMS-based micro-robots of less than one centimeter in length using various actuation mechanisms. In [74], Ebefors et al. built a silicon walking robot with thermally-actuated, single degree-of-freedom, spin-coated polyimide leg joints. The actuators were sufficient to carry a load more than 30 times the weight of robot, such that a power supply could be maintained through tethered bonding wires. Large weight-bearing capacities for a thermally actuated robot have also been demonstrated by Murthy et al. [75]. In [76], Hollar et al. built electrostatic inch-worm motors to generate high forces in a two-legged microrobot from an on-board 50V high-voltage translator and solar cell. In [77], Bergbreiter et al. integrated electrostatic inchworm motors with molded elastomers to generate a rapid jumping motion from a similar power source. In [78], Donald et al. used electrostatic scratch drives, and in [79], Mohebbi et al. used thermally actuated silicon motors to drive high force motion, but the former approach limits mobility, while the latter requires large actuation power.

For high-speed, high-mobility, and low-power operation, piezoelectric actuators

have potential advantages. One candidate technology is thin-film lead-zirconate-titanate (PZT) actuators, as produced in the previous chapter, that produce comparatively large lateral displacements for a piezoelectric actuator through a novel combination of unimorph bending motions. From such elements, actuator arrays generating series rotational between 5° and 20° at 20V can potentially enable comparatively large range-of-motion appendages mechanisms for autonomous microrobotic platforms [80], [81]. However, previously used techniques for integrating thin-film PZT unimorph benders with high-aspect ratio structures has limited the complexity of potential micro-actuator joint arrays, preventing assembly into full robot chasses. Nonetheless, piezoelectric actuation remains a desirable candidate technology due to large force capacity, modest voltage requirements, and ability to recover much stored electrical energy using charge recovery techniques.

From the microfabrication procedure in Chapter II, improved micro-robotic leg joint arrays capable of producing multi-degree of freedom motion are produced. Modeling and experimental characterization are then conducted in this chapter. The resulting mechanisms harness the high force generation over low stroke lengths of thin-film PZT lateral actuators to produce total displacement on the order of 1 mm at the tip of a robotic leg.

As shown in Chapter II, low pressure chemical vapor deposition (LPCVD) of silicon oxide vertical barrier trenches prior to thin film PZT deposition enables the integration of thin-film PZT deposition with complex multi-layer silicon structures on silicon-on-insulator wafers Consistent undercut length of thin-film PZT actuators array was realized, which is essential for producing proposed micro-robotic platforms with

complex joint configurations. Furthermore, the effective piezoelectric performance measure, $d_{31,eff}$, of piezoelectric unimorph benders was measured with minimal change in magnitude compared to benders produced by previous photoresist encapsulation techniques [82].

In previous works, piezoelectric robot leg joint displacements have been modeled in a limited number of dimensions. The modeling of static in-plane displacement of a leg link and of eight-parallel in-plane actuators array was obtained in [81]. Also, the modeling of static vertical displacement of the vertical actuators was obtained in [82]. In [81], the static rotation angle for each leg link is obtained when the lateral displacement of the thin-film PZT actuator and the displacement of the silicon tether are considered. The modeling of an in-plane, eight-parallel-actuators array is obtained from a lumped second order dynamic model. In this chapter, new modeling is obtained of static displacement of compact in-plane arrays. These are joints β and γ as they are shown in Figure 3.1. In addition, the rigidity of a thin-film PZT interconnect between joints α and β is found to be non-negligible during experimental testing. Thus, the improved modeling also takes the rigidity of PZT interconnect into account when the estimation of the displacement generated by joint β is considered.

In [82], the static vertical displacement of a vertical thin-film PZT actuator was obtained, where a thin-film actuator consists of a downward and an upward bending segment. From the radii of curvature of each segment and with appropriate boundary conditions, the modeling of the vertical displacement is obtained. In this chapter, however, the vertical actuator of a prototype robot leg, joint α in Figure 3.1, is modeled in terms of small displacement relationships but in multiple dimensions because the length

of the vertical actuator is shorter than of the actuators in the previous example system in [82].

In the following sections, the analytical models for piezoelectric vertical and lateral actuators are introduced, and applied to the actuator arrays. In addition, experimental characterization of fabrication process and the kinematics and dynamics of a sample micro-robotic leg are conducted.

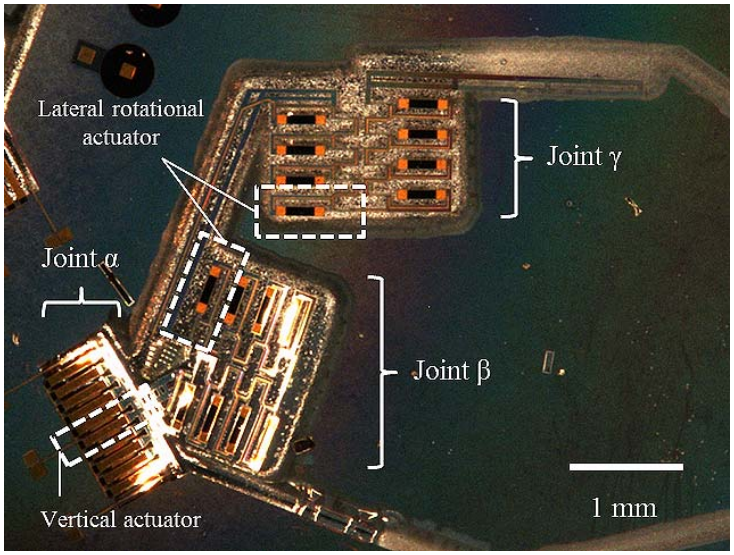

Fig. 3.1 A fully released multi-Degree of Freedom leg, with individual actuators and joint arrays marked

3.2 Basics of Thin-Film PZT Actuator Arrays

Two types of thin-film piezoelectric actuators are used to create multi-degree-of-freedom appendages in this work. These are the same types of actuators as discussed in the previous chapter: lateral (or in-plane) rotational actuators and vertical (or out-of-plane) unimorph bending actuators [85]. These are integrated into the robotic leg joint as shown in Figure 3.1. The first joint in the appendage, labeled joint α, moves in a vertical

direction, and consists of a parallel arrangement of ten 100μm-by-536μm PZT/Au unimorph actuators. Further down the leg, two in-plane actuator arrays, labeled joints β and γ, respectively, consist of series arrays of eight 102μm-by-479μm PZT lateral actuators attached to rotational flexure mechanisms.

Individual actuators within these arrays consist of unimorph bending segments: a single uniform segment for the vertical actuators, and a combination of two bend-down and two bend-up segments for the lateral actuators, as reported in [24]. Each segment contains a material stack of silicon dioxide, PZT thin films, and metal layers. In the material stack, the PZT thin film both imposes a contractive force, F_{act}, and a bend-down or bend-up moment, $M_{act,1}$ or $M_{act,2}$, under an applied voltage according to:

$$F_{act} = e_{31,eff} \frac{V}{t_{PZT}} A_{PZT} \tag{3.1}$$

$$M_{act,i} = e_{31,eff} \frac{V}{t_{PZT}} A_{PZT} \left(\bar{y}_{PZT} - \bar{y}_i \right) \tag{3.2}$$

where $e_{31,eff}$ is the effective field dependent electro-active stress coefficient, which is an effective ratio of stress to electric field rather than the exact linear piezoelectric coefficient of the material [24]. The coefficient is approximated using the nominal (short circuit) axial elastic modulus, E_{PZT}, of the PZT film in a free beam and the effective field dependent electro-active strain coefficient, $d_{31,eff}$. The empirical values of $e_{31,eff}$ and $d_{31,eff}$ include a number of effects associated with the effective piezoelectric coefficient, $d_{31,f}$, or effective piezoelectric stress coefficient, $e_{31,f}$, and nonlinear piezoelectric/ferroelectric and electro-active material responses [82]. V is the applied voltage, t_{pzt} and A_{pzt} are the

thickness and the cross-sectional area of PZT, $\bar{y}_{PZT}$ is the position of the PZT film midline in the unimorph material stack, and $\bar{y}_1$ and $\bar{y}_2$ are neutral axes of the bend-down (with Au) and bend-up (without Au) unimorph segments, respectively. Finally, $(EI)_1$ and $(EI)_2$ are the composite rigidity of respective thin-film PZT unimorphs. Table 3.1 lists the values of the parameters of the thin-film PZT actuators.

Table 3.1 Properties of Thin-Film PZT Lateral Rotational and Vertical Actuators

Parameter	Value	Parameter	Value
t_{Au}	1 (μm)	L_{PZT}	480 (μm)
t_{Pt}	0.105 (μm)	L_v	536 (μm)
t_{PZT}	0.8 (μm)	$w_{flexure}$	13 (μm)
$t_{Ti/Pt}$	0.08 (μm)	w_{tether}	10 (μm)
t_{SiO2}	0.17 (μm)	$(EI)_{flex}$	$1.693 \cdot 10^2$ (N·μm^2)
$\bar{y}_{PZT}$	0.62 (μm)	$(EA)_t$	11.20 (N)
$\bar{y}_1$	1.05 (μm)	$(EI)_1$	6.909 (N·μm^2)

3.3 Thin-Film PZT Vertical Actuator Array

Simple unimorph bending generates vertical motion from the first joint in the multi-degree-of-freedom appendages. Displacements of each actuator of the array can be expressed using six coordinates: $d = [x\ y\ z\ \theta_x\ \theta_y\ \theta_z]^T$, although only coordinates associated with significant motion are shown in each respective joint analysis. Since all vertical actuators are composed of identical silicon dioxide, PZT thin films, and metal layer, a multi-layer composite cantilever is an appropriate model to estimate the displacement of vertical actuator, $d_{(\alpha)}$. This model is given by

$$d_{(\alpha)} = \begin{bmatrix} z_{(\alpha)} \\ \theta_{x,(\alpha)} \end{bmatrix} = \begin{bmatrix} \frac{L_v^{\,2}}{2(EI)_1} \\ \frac{L_v}{(EI)_1} \end{bmatrix} M_{act,1} + \begin{bmatrix} \frac{L_v^{\,3}}{3(EI)_1} & \frac{L_v^{\,2}}{2(EI)_1} \\ \frac{L_v^{\,2}}{2(EI)_1} & \frac{L_v}{(EI)_1} \end{bmatrix} \begin{bmatrix} \frac{F_v}{N} \\ \frac{M_v}{N} \end{bmatrix} \tag{3.3}$$

where $z_{(\alpha)}$ and $\theta_{x,(\alpha)}$ are the vertical displacement and the rotational angle at the tip of joint α, L_v is the length of a vertical actuator, F_v and M_v are external force and moment, if present, due to the external loads applied at the tip of vertical actuators, and N is the number of vertical actuators connected in parallel. If desired, a lateral displacement at the tip of the joint, $y_{(\alpha)}$ component may also be estimated through numerical integration along the small angle displacement of $\theta_{x,(\alpha)}$.

3.4 Thin-Film PZT Lateral Rotational Actuators

Motion of lateral actuator arrays (joints β and γ) is driven by individual lateral PZT actuators [86] integrated with silicon flexural structures. The net motion at the tip of individual lateral actuators is ideally horizontal, as two bend-down and two bend-up segments are located symmetrically on either side of the actuator mid-point. However, due to residual stress in the thin films, unconstrained in-plane motion is not generally obtained, so the end of the actuator is connected to the high-aspect ratio silicon flexural structure that prevents out-of-plane bending, under most circumstances. The flexure structure also converts small translational piezoelectric displacements into rotational displacements.

Force-displacement curves for such lateral actuators have been previously described in [24]. For micro-robotic leg design, a region of small displacement and large

force is chosen to increase weight bearing capacity and locomotion speed of joint structures. In that region of behavior, the axial contraction in Eq. 3.1 dominates actuator motion, while the bending motion of beams that can lead to larger displacements against small forces has negligible influence on the present leg joint designs. Eq. 3.4 shows the in-plane, small displacement model for a single actuator rotary joint that consists of a high-aspect ratio elastic flexure and tether, a PZT actuator, and a rigid link as shown in Figure 3.2. The relation between the force generated by a single actuator and the displacement at the tip of the flexure in the rotary motion is as follow:

$$\left(\frac{k_{f,\theta} k_{t,\theta}}{k_{f,\theta} + k_{t,\theta}} + k_{act,\theta} \right) \theta = F_{act} L_{act} \tag{3.4}$$

$$k_{f,\theta} = \frac{(EI)_{flex}}{L_{flex}} \tag{3.5}$$

$$k_{t,\theta} = \frac{{L_{act}}^2 (EA)_t}{L_t} \tag{3.6}$$

$$k_{act,\theta} = k_{act} (F_{act}) {L_{act}}^2 \tag{3.7}$$

where $k_{f,\theta}$, $k_{t,\theta}$, and $k_{act,\theta}$ are the rotational spring stiffness of the flexure, tether, and actuator, k_{act} is the axial spring stiffness of the actuator, $(EI)_{flex}$ and $(EA)_t$ are the composite flexural rigidity of the composite silicon/silicon dioxide flexure and tether along transverse and axial directions, respectively, L_{act} is the distance between the tether and flexure joint, L_{flex} and L_t are the length of the flexure joint and tether as shown in Figure 3.1 and in Table 3.1, and θ is the rotary angle at the tip of the flexure. Because the actuator itself and the silicon tether experience the axial force generated by piezoelectric

film, the maximum rotary angle is represented in terms of the combined spring stiffness of the joint structure in Eq. 3.5 – 3.7 as shown in Figure 3.2.

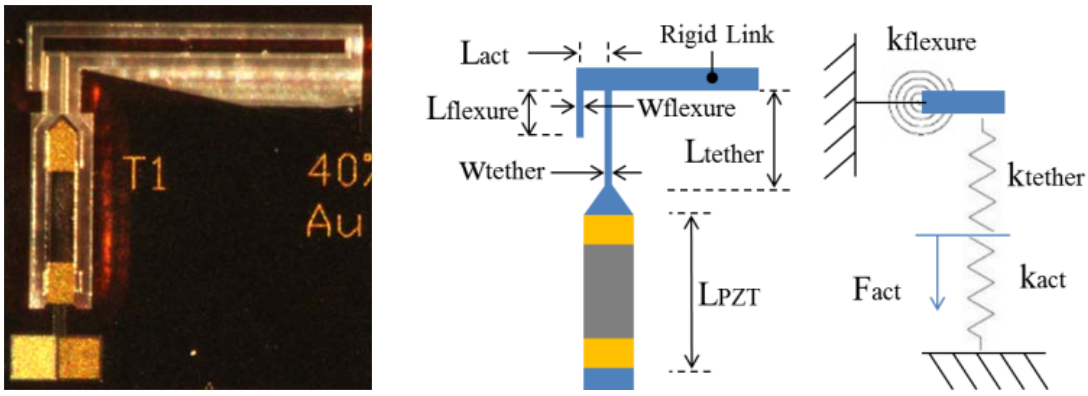

Fig. 3.2 A single thin-film PZT lateral rotational actuator connected to a high-aspect ratio silicon flexural structure; left: optical image; middle: schematic drawing; right: equivalent spring structure

3.5 High-Aspect Ratio Silicon Lateral Joint Arrays

Each array of in-plane actuators forming the in-plane joints of the leg is arranged to have two sets of four lateral actuators and flexural mechanisms facing each other in rows of four, as shown in Figure 3.3. Such arrays are intended to multiply rotational motion of individual actuators and to reduce out-of-plane deflection due to torsion from weight bearing of future micro-robotic platforms. This latter effect is accomplished by aligning the high-aspect ratio flexures towards the micro-robot's foot. The displacement of these arrays (referred to as a compact array) is represented in terms of the driving thin-film PZT actuation force and its equivalent rotary moment. From the schematics of local coordinates associated with individual silicon linkage structures in Figure 3.3, the displacement of each actuator can be expressed with a vector of coordinates. The i^{th} coordinate vector with respect to the i-1^{th} coordinate vector is obtained in Eq. 3.8 when

the axial force and the equivalent moment are applied at the silicon flexure. The resulting deflection at the i^{th} coordinate vector is given by:

$$d_i^{i-1}{}_{(\beta,\gamma)} = T \cdot f^{i-1}{}_{(\beta,\gamma)} + p^{i-1} + R_i^{i-1}{}_{(\beta,\gamma)} q^i \tag{3.8}$$

where $d_i{}^{i-1}$ is the local displacement of the origin of the i^{th} coordinate with respect to i-1^{th} coordinate within the compact array, T is the compliance matrix of the flexure structure, f^{i-1} is the forcing term generated by the actuator and, if present, external forces and moments, p^{i-1} is the initial position of flexure tip, R_i^{i-1} is the rotational matrix of the i^{th} coordinate from i-1^{th} coordinate, and q_i is the position vector between the i^{th} and i-1^{th} coordinates. The subscript, β or γ, indicates whether the model is referring to the inner or outer compact array,

When there is no exerted out-of-plane load and no external load applied, a simplified two-dimensional force-displacement relation for a compact in-plane array is obtained in Eq. 3.9:

$$\begin{aligned} d_i^{i-1}{}_{(\beta,\gamma)} = \begin{bmatrix} x_{(\beta,\gamma)} \\ y_{(\beta,\gamma)} \\ \theta_{z(\beta,\gamma)} \end{bmatrix}_i^{i-1} &= \begin{bmatrix} \frac{L_{flex}}{(EA)_{flex}} & 0 & 0 \\ 0 & \frac{L_{flex}{}^3}{3(EI)_{flex}} & \frac{L_{flex}{}^2 L_{act}}{2(EI)_{flex}} \\ 0 & \frac{L_{flex}{}^2}{2(EI)_{flex}} & k_{\theta,total}^{-1} L_{act} \end{bmatrix} \begin{bmatrix} F_{act} \\ 0 \\ F_{act} \end{bmatrix}_{(\beta,\gamma)}^{i-1} \\ &+ \begin{bmatrix} L_{flex} \\ L_{act} \\ 0 \end{bmatrix}^{i-1} + \begin{bmatrix} \cos\theta_{z,(\beta,\gamma)} & -\sin\theta_{z,(\beta,\gamma)} & 0 \\ \sin\theta_{z,(\beta,\gamma)} & \cos\theta_{z,(\beta,\gamma)} & 0 \\ 0 & 0 & 1 \end{bmatrix}_i^{i-1} \begin{bmatrix} x_{off} \\ y_{off} \\ 0 \end{bmatrix}^i \end{aligned} \tag{3.9}$$

where $(EI)_{flex}$ is the axial composite flexural rigidity of a oxide barrier-silicon flexure, $k_{\theta,total}^{-1}$ is the inverse of the composite spring stiffness of Eq. 3.5 – 3.7, the compliance matrix, T, in Eq. 3.8 is obtained in terms of axial and transverse rigidity of the flexure, the initial position, p^{i-1}, of flexure tip is offset by a distance L_{flex} and L_{act} from its origin, and the position vector, q_i, is obtained with x_{off} and y_{off}, which is the position component along the x and y direction in the i^{th} coordinate, as shown in Figure 3.3. The transverse deflection of each tether itself is treated as negligible under small rotational displacement and only axial force is applied along the tether.

To calculate total displacements, the displacement of the origin of the i^{th} coordinate with respect to the first coordinate is the summation of projections onto previous coordinates. So, displacement of the m^{th} coordinate with respect to the origin of the first flexure joint is represented as follows:

$$d^{1}_{m(\beta,\gamma)} = \sum_{n=1}^{m}\prod_{k=1}^{n} R^{k-1}_{k\ (\beta,\gamma)}\left(p^{n} + T\cdot f^{n}_{\ (\beta,\gamma)} + R^{n}_{n+1(\beta,\gamma)} q^{n+1}\right) \tag{3.10}$$

where $d_8^{\ 1}$ is the total local displacement of the compact array with the subscript, β or γ, that represents the inner or outer compact array, and $R_i^{\ j}$ is the rotational matrix of the i^{th} coordinate with respect to j^{th} coordinate by the angle of θ_i. For $i \geq 5$, $R_i^{\ 4}$ is a transformation combining reorientation of axis by π radians, $R(\pi)$, with rotational displacement by θ_i, $R(\theta_i)$. When $i = 1$, $R_1^{\ 0}$ is the identity matrix.

Eq. 3.9 can be applied directly to the outer in-plane actuator array (joint γ), but in the m-DoF device fabricated, motion of the inner lateral actuation array, joint β, is

limited by the need to deliver an electrical signal to joint γ. This signal is transferred via an elastic interconnect created from the PZT-metal stack. As the inner compact array and the interconnect are mechanically connected in parallel, the following relation is used to predict in-plane motion of the resulting combination, based on the assumption that only small angular displacements contribute non-negligible stiffness to the elastic interconnect:

$$M_{ic,z} = \frac{(EI)_{ic,z}}{L_{ic}} \sum_{i=1}^{8} \left(\theta_{z,(\beta)}\right)_i \tag{3.11}$$

where $(EI)_{ic,z}$ and L_{ic} are the composite in-plane rigidity and effective length of the material stacked PZT thin film interconnect, and $M_{ic,z}$ is the moment applied at the interconnect by the inner compact actuators. The displacement of the tip of the elastic interconnect from the center of in-plane compact array, δ_c, is estimated from the length of the PZT interconnect and the sum of rotational displacement of each link, $\Sigma(\theta_{z,(\beta)})_i$. Since the inner compact array and the PZT thin film are connected in parallel, the radius of rotation exerted by inner compact array is close to δ_c for the small displacement exerted by the parallel structure of the interconnect and inner compact array. The moment is equivalent to the force, which is the ratio of $M_{ic,z}$ to δ_c from the center of rotation, applied at the tip of 8th link of inner compact array. This force applied at 8th link, $f_{ic}^{\ 8}$, is then projected onto each flexure by $f_{ic}^{\ i}$ at i^{th} link in addition to the forcing component by individual actuators, F_{act}, in Eq. 3.9. This produces new forcing terms within the array:

$$f_{ic}^{8} \approx \frac{M_{ic,z}}{\delta_c}\begin{bmatrix} \sin\left(\theta_{z,(\beta)}\right)_8 \\ \cos\left(\theta_{z,(\beta)}\right)_8 \\ 0 \end{bmatrix}, \quad f_{ic}^{i} \approx \frac{M_{ic,z}}{\delta_c}\begin{bmatrix} \sin\left(\theta_{z,(\beta)}\right)_{i,8} \\ \cos\left(\theta_{z,(\beta)}\right)_{i,8} \\ 0 \end{bmatrix} \tag{3.12}$$

where $(\theta_{z,(\beta)})_{i,8}$ is the sum of rotational displacement from i^{th} link to 8th link. Then the forcing term, $f^{n}{}_{(\beta)}$, in Eq. 10 consists of $[F_{act}, 0, F_{act}]^{T}$ from Eq. 3.9 and $f_{ic}{}^{i}$ from Eq. 3.12, and the nonlinear system of equations from Eq. 3.8, 3.10, 3.11, and 3.12 is solved numerically for $(\theta_{z,(\beta)})_i$ [80].

It should be noted that even with high-aspect ratio flexure and tether structures, residual stress in the experimentally released prototype devices still leads to some out-of-plane bending from the in-plane actuators, causing the 4th and 5th coordinates to shift above the 1st and 8th coordinates in Figure 3.3. Thus, an addition to the lateral actuator model to account for out-of-plane deformation is obtained using empirical observations in Section 3.1.2.

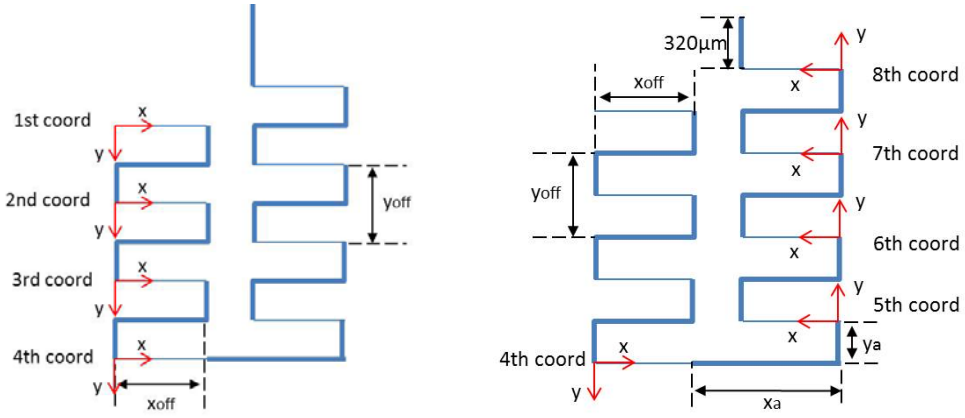

Fig. 3.3 Schematics of local coordinates of inner and outer actuators array in multi-degree of freedom robotic leg

3.6 Experimental Results

3.6.1 Trajectory Analysis

Completed multi-degree-of-freedom leg joints were characterized experimentally to verify functionality and vertical and lateral joint design performance. This experimental verification is based on kinematic descriptions of joint motion, with deformation of continuous beams (vertical unimorph actuators and elastic rotational flexures, for out-of-plane and in-plane motion, respectively) converted to motion of specified points on a prototype actuator in global coordinates [84]. This motion was captured by a high-speed camera above the device, and global coordinate (x_{global}, y_{global}) data are obtained from the optical images.

In the trajectory analysis, the following locations are used as reference frame of the local coordinates:

- Point 0 represents beginning of leg, at the fixed end of the vertical actuators, oriented along the long axis of the vertical actuators.
- Point A represents the tip of the vertical actuators (end of joint α), where a rigid silicon connection to joint β begins.
- Points β_0 and B represent the beginning and end of joint β, at the end of the rigid silicon connector between joints α and β.
- Points γ_0 and C represent the beginning and end, respectively, of joint γ, at the end of the rigid silicon connector between joints β and γ.
- Point D is the end tip of the multi-degree of freedom leg.
- Point E is the corner of the rigid silicon link between joints β and γ (which is comparatively easy to track with the camera for later joint displacement analysis).

Then, the local coordinate axes for each joint is chosen such that the y_0-axis is aligned along the lateral direction of the thin-film PZT actuators in the given joint, and local displacements are related to global displacements of points of interest using rotation matrices. Fixed rotation matrices are denoted by the notation $R(\theta_{i,b/a})$, where i corresponds to the local axis of rotation, and b and a indicate the ending and starting points of interest, respectively, that a change in orientation is taken from. As an example, for the first rotation matrix, from the global coordinates to the base of the vertical actuators, the rotational matrix is formed from $\theta_{z,A/0}$ which is the angle between global coordinates (x_{global}, y_{global}, z_{global}) and the local coordinates (x_0, y_0, z_0) at point 0, the beginning of the leg. From the measured distance of point A from 0, $\theta_{z,A/0}$ is estimated at 39.5^0, and coordinate transformation from the raw data to the desired coordinate (x_0, y_0, z_0) is obtained in Eq. 3.13:

$$X_{global} = R\left(\theta_{z,A/0}\right) X_0 \tag{3.13}$$

where X_{global} and X_0 are the position vectors with respect to the global and point 0 coordinates.

Rotations that may change with applied voltage are also written using standard rotation matrices, denoted by $H(\theta_{i,b/a})$, and generally their rotation angles consist of a fixed component, due to residual stress, and changing component due to applied voltage. For example, the rotation matrix used to transform coordinates about point A with respect to coordinates about point 0 is written $H(\theta_{x,A/0})$, with $\theta_{x,A/0}$ being the sum of vertical rotation at the tip joint α due to residual stress and due to an applied input voltage.

Displacements of any point of interest, as measured in global coordinates, can likewise be related to rotations and displacements of proceeding links in the robotic leg. For example, the displacement of the tip in terms of global coordinates, X_D, depends on all relevant rotations and displacements, as:

$$\begin{aligned} X_D &= H\left(\theta_{x,A/0}\right) R\left(\theta_{z,\beta_0/A}\right) H\left(\theta_{x,B/\beta_0}\right) H\left(\theta_{z,C/\gamma_0}\right) X_{D/C} \\ &+ H\left(\theta_{x,A/0}\right) R\left(\theta_{z,\beta_0/A}\right) H\left(\theta_{x,B/\beta_0}\right) s_{trans} \\ &+ H\left(\theta_{x,A/0}\right) R\left(\theta_{z,\beta_0/A}\right) w_{trans} + H\left(\theta_{x,A/0}\right) u_{trans} + v_{trans} \end{aligned} \tag{3.14}$$

where $H(\theta_{x,A/0})$, $H(\theta_{x,B/\beta 0})$ and $H(\theta_{z,C/\gamma 0})$, are the local coordinate transformations due to rotations at joints α, β, and γ, respectively, $R(\theta_{z,\beta 0/A})$ is a fixed rotation representing the difference in orientation between joint α and joint β. $X_{D/C}$ is fixed translational offset of the tip of the leg from the end of joint γ, s_{trans} is the nominal offset from the beginning of joint γ to end of joint γ plus any displacement of joint γ (i.e. ${d_8}^1{}_{(\gamma)}$) due to an applied voltage, w_{trans} is the nominal offset from the beginning of joint β to end of joint γ plus any displacement exerted by joint β (i.e. ${d_8}^1{}_{(\beta)}$), due to applied voltage, u_{trans} is the nominal offset of joint β from joint α, and v_{tran} is the nominal offset from the beginning to the end of joint α plus any displacement of joint α due to an applied voltage.

Figure 3.4 shows the top view of the device and the trajectory of E (knee) and point D (foot) taken by the stereoscope and high speed camera when the vertical actuators are activated by various input voltage. Figure 3.5 shows the trajectories of points D and E under applied voltage to joints α. Differences between the designed and measured trajectories of leg arise from various non-idealities in the fabrication process, particularly

(1) excess silicon dioxide that increases stiffness of some flexures and, especially, the interconnect across the inner lateral actuator and (2) residual stress in the actuator arrays. In Figure 3.5, the direction of motion of point D and E exerted by joint α is opposite to the intended direction. This is because residual stress causes the leg to start in an upward deflected position, such that downward rotation of the vertical actuator under an applied voltage causes the tip of the leg to move away from the base (in global (x,y) coordinates), rather than closer to the base if the leg had started in a flat, fully extended position. Furthermore, residual stress leading to deformation of joint β causes significant out-of-plane bending. Two major differences are indicated by Figure 3.6: first, increased stiffness of interconnect parallel to joint β significantly reduces it range of motion, and second, out-of-plane deflection of joint β resulting from residual stress pulling the two halves of the array out-of-plane from one another produces additional vertical, rather than planar, motion.

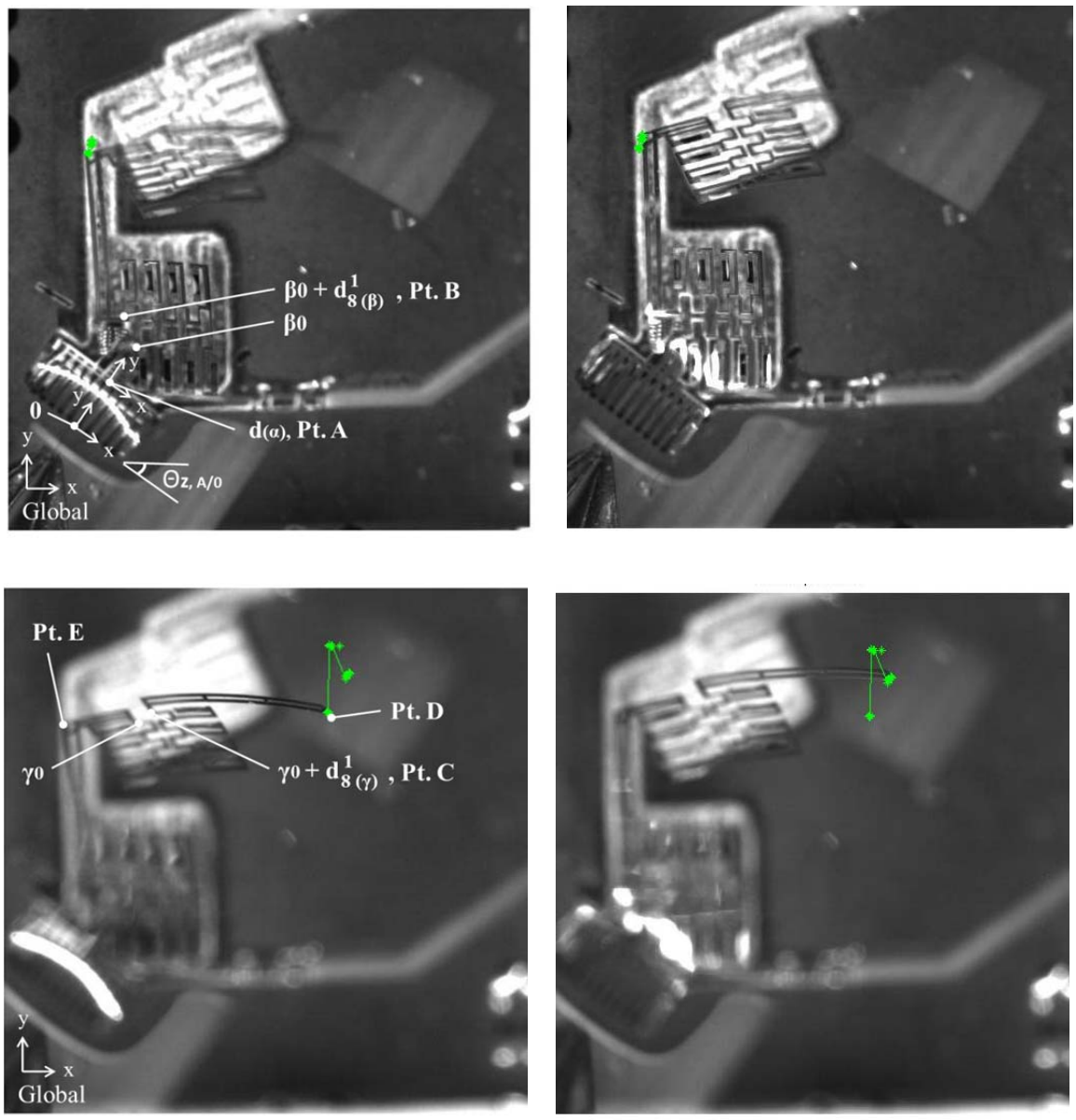

Fig. 3.4 Trajectory of point E (knee) between joint β and γ, and point D (foot) as the vertical actuators are activated by 15V DC. The stereoscope images are taken by 60 frames per second. The left images are at 0V, and the right images are at 15V.

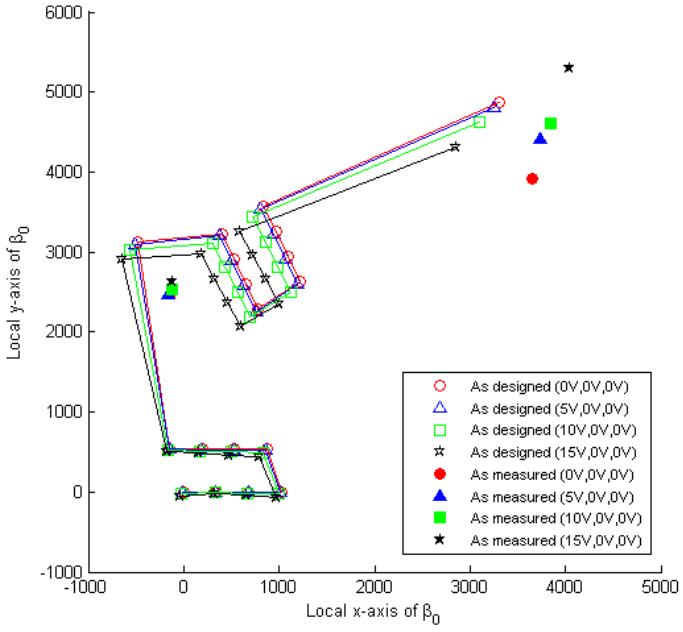

Fig. 3.5 Trajectory of two in-plane compact arrays with point D (foot) and E (knee) represented with hollow markers, as designed, and represented with solid markers, as measured, with respect to point β_0 when joint α is activated.

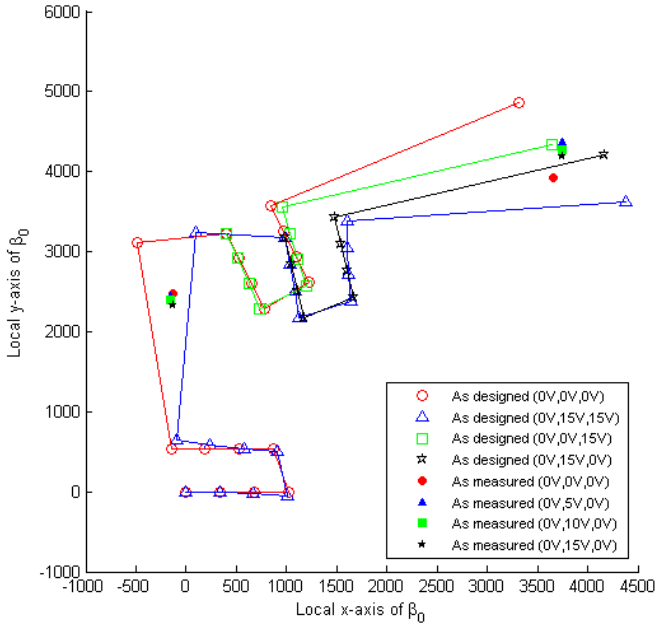

Fig. 3.6 Trajectory of two in-plane compact arrays with point D (foot) and E (knee) represented with hollow markers, as designed, when joint β and γ are activated separately, and represented with solid markers, as measured, with respect to point β_0 when joint β is activated.

3.6.2 Comparison to Actuator Models

From observed motion at the points of interest along the leg, mapping back their displacements to displacements at the actuator arrays allows actuator array performance to be verified. Beginning with the 8-coordinate system in Figure 3.3 and using the rotation matrices to represent initial orientations due to residual stress effects, static rotational displacements of the various actuator arrays can be obtained. As in the examples in Figures 3.4 and 3.5, any joints in the fabricated device can be represented by Eq. 3.13 and 3.14. Since the motion of multi-degree of freedom (m-DoF) microrobotic legs is generated by combinations of two in-plane compact actuators and vertical actuators, different sets of actuators were independently activated to verify actuator models. Three sets of displacements are shown in Tables 3.2, 3.3, and 3.4, for the three actuators. The first set of results shows displacement of an ideal leg design, which assumes a planar neutral position (no residual stress), no excess silicon dioxide, and negligible interconnect stiffness across the inner lateral actuator; this set of results is intended to demonstrate the ideal capabilities of the device. The second set of results shows the predicted displacements when residual stress effects are included, with extra oxide, and with full interconnect modeling. The third set of results is from the experimentally extracted actuator array displacements and rotations, when measureable.

In general there is good agreement between experimental and model results when non-idealities are taken into account. Angular rotation of the vertical actuator tip is closely matched to the model, though the initial curvature due to residual stress changes the associated tip displacements from the ideal case. Similarly, in-plane motions of the

two lateral actuators arrays (x, y, and θ_z displacements) are very similar to experimental results, so long as interconnect stiffness is accounted for in the design as fabricated.

Table 3.2 Displacement of Point A by Vertical Actuators

Degree of Freedom	As designed	As fabricated (from model)	As fabricated (from experiment)
x (μm)	0	0	1.86
y (μm)	-43	10.6	19.4
z (μm)	-189	-189	-148
θ_x (°)	-40	-40	-37
θ_y (°)	0	0	0
θ_z (°)	0	0	0

Table 3.3 Displacement of Point E with respect to Point A by Inner Compact Actuators

Degree of Freedom	As designed	As fabricated (from model)	As fabricated (from experiment)
x (μm)	230	4.9	3.8
y (μm)	65	-133	-143
z (μm)	0	843	798
θ_x (°)	0	18.9	18.1
θ_y (°)	0	0	Unable to measure
θ_z (°)	-4.7	-0.1	-0.1

Table 3.4 Displacement of Point C with respect to Point E by Outer Compact Actuators

Degree of Freedom	As designed	As fabricated (from model)	As fabricated (from experiment)
x (μm)	149	144	114
y (μm)	-208	-201	-186
z (μm)	0	0	108
θ_x (°)	0	0	17.7
θ_y (°)	0	0	Unable to measure
θ_z (°)	-4.7	-4.5	-3.85

However, one major adjustment must be made to array modeling under the influence of residual stress based on experiment observations. Specifically, vertical displacement is observed from the intended-to-be-lateral actuator arrays, as residual stress pulls the component actuators out of a purely planar arrangement. This is especially significant when the elastic interconnect is present, as a deformation similar to buckling is observed.

To account for the motion of the PZT interconnect in the model, an out-of-plane bending moment about x-axis at point A is estimated from non-uniform residual stress of PZT thin films on the actuators array and the rigidity of PZT thin film interconnect. This effect can be estimated by the offset distance, ε_{dist}, of the beginning of the rigid silicon link between joints β and γ along the local z-direction with respect to point A during the motion. This offset distance and in-plane actuation moment result in out-of-plane deflection, and thus, the resulting angle, $\theta_{ic,y}$, of the thin-film PZT interconnect about point A. Thus, a lumped spring model is used to estimate the displacement of the parallel structure of the elastic interconnect and joint β, which is represented by the displacement of joint β, $d_8{}^1{}_{(\beta)}$:

$$d^1_{8(\beta)} \approx \left(K_{ic,eq} G_{ic} + K_{array,eq} \right)^{-1} F_{act} \tag{3.15}$$

where $K_{ic,eq}$ and $K_{array,eq}$, are the lumped spring stiffness of the thin film interconnect and inner in-plane actuators array, and G_{ic} is a matrix projecting the additional spring force at the tip of the interconnect back to actuator locations. From Eq. 3.15, the stiffness matrix, $K_{ic,eq}$, for PZT interconnect is modeled as:

$$d_{ic} = \begin{bmatrix} x_{ic} \\ y_{ic} \\ z_{ic} \\ \theta_{ic,y} \\ \theta_{ic,z} \end{bmatrix} = K_{ic.eq}^{-1} F_{ic} = \begin{bmatrix} L_{ic}\left(EA\right)_{ic}^{-1} & 0 & 0 \\ 0 & 0 & L_{ic}^{2}\left(2\left(EI\right)_{ic,z}\right)^{-1} \\ 0 & -L_{ic}^{2}\left(2\left(EI\right)_{ic,y}\right)^{-1} & 0 \\ 0 & L_{ic}\left(EI\right)_{ic,y}^{-1} & 0 \\ 0 & 0 & L_{ic}\left(EI\right)_{ic,z}^{-1} \end{bmatrix} \begin{bmatrix} F_{ic,x} \\ M_{ic,y} \\ M_{ic,z} \end{bmatrix} \tag{3.16}$$

where F_{ic} is the forcing term applied at the tip of the interconnect with the axial force, $F_{ic,x}$, out-of-plane moment, $M_{ic,y}$, and rotational moment, $M_{ic,z}$, respectively. Then the relation of the forcing term, F_{ic}, to the lateral actuation force, F_{act}, within joint β is obtained from Eq. 3.11:

$$F_{ic} = \begin{bmatrix} L_{act}\delta_{c}^{-1}\cos\left(\sum_{i=1}^{8}\left(\theta_{z,(\beta)}\right)_{i}\right) \\ L_{act}\varepsilon_{dist}L_{ic}^{-1}\delta_{c}^{-1}\cos\left(\sum_{i=1}^{8}\left(\theta_{z,(\beta)}\right)_{i}\right) \\ L_{act} \end{bmatrix} N \cdot F_{act} = G_{ic}F_{act} \tag{3.17}$$

A lumped compliance matrix for the joint β is derived from Eq. 3.10 and 3.12 for the case when only very small displacements of point B are observed and joint displacements are assumed to be exerted equally by each actuator. This model, combining the motion at the 8 individual actuators into an approximate lumped model, becomes:

$$d^1_{8(\beta)} = \begin{bmatrix} x_{(\beta)} \\ y_{(\beta)} \\ z_{(\beta)} \\ \theta_{y,(\beta)} \\ \theta_{z,(\beta)} \end{bmatrix} \approx K^{-1}_{array,eq} F_{act} = \begin{bmatrix} L_{flex}\left(EA\right)_{flex}^{-1} & 0 & 0 \\ 0 & 0 & L_{flex}{}^2 L_{act}\left(2\left(EI\right)_{flex,z}\right)^{-1} \\ 0 & -L_{flex}{}^2\left(2\left(EI\right)_{flex,y}\right)^{-1} & 0 \\ 0 & L_{flex}\left(EI\right)_{flex,y}^{-1} & 0 \\ 0 & 0 & k^{-1}_{\theta,tot} L_{act} \end{bmatrix} N \cdot F_{act} \qquad (3.18)$$

It is seen that in the above model the measured planar motion of point B is constrained by the PZT thin film interconnect, and the lumped model of fabricated device shows that the axial directional rigidity of PZT thin film interconnect prevents inner compact actuators from achieving full in-plane rotation, and the out-of-plane bending effect is considerable when ε_{dist} is assumed to be larger than thickness of silicon layer. Under these circumstances, Table 3.3 shows that the expanded lumped-parameter model in Eq. 3.15 – 3.18 produces a good approximation of motion in joint β.

3.6.3 Frequency Response

Resonance analysis of the fabricated m-DoF microrobotic legs indicates that such a robotic appendage is capable of moving with a high bandwidth. Figure 3.7 shows the frequency response of point C measured with respect to the global coordinate defined the high speed camera under stereoscope when the vertical actuators array is activated. The input is a sinusoid where the offset and peak-to-peak voltage are chosen to be 3V and 2Vpp. The *Q*-factor of the vertical motion is approximately obtained as 8.58 at the first resonant frequency, 34.7Hz. Table 3.5 shows resonant frequencies of other points when

vertical actuator and compact actuator sets are independently activated. When the vertical actuator is activated, a 280-millisecond settling step time was observed at the foot.

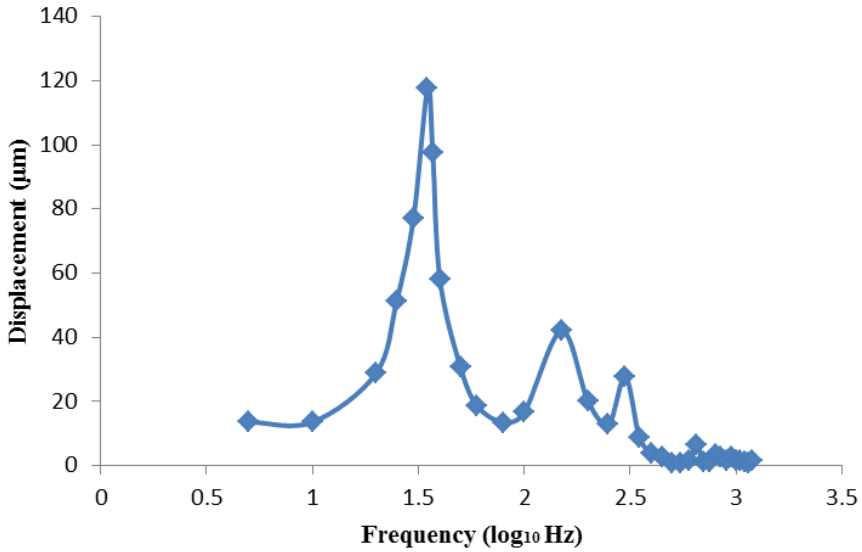

Fig. 3.7 Frequency response of point C (foot) measured with respect to global coordinates when the vertical actuators array is activated with driving sinusoidal input.

Table 3.5 Resonance Frequencies

Actuator	Measurement	1st and higher resonant frequency
Vertical actuator	Point A (hip)	300, 1500, 1810 Hz
	Point B (knee)	37, 300, 800 Hz
	Point C (foot)	35, 150, 300, 650 Hz
Compact actuator	Point A (hip)	1510, 1810 Hz
	Point B (knee)	800 Hz
	Point C (foot)	30, 150, 250, 650, 1150, 1450 Hz

3.6.4 Weight and Power Considerations

For use in producing terrestrial micro-robot locomotion, weight bearing and energy use of a given robot leg design are critical. As fabricated, the primary source of out-of-plane compliance to load at the leg tip is the vertical actuators. This compliance can be estimated from Eq. 3.3, using an external moment on the vertical actuator equal to the weight load times the leg length. Estimated compliance is 3080 rad/N. For the actuated motion of the foot to be greater than any bending of the vertical actuators during load bearing, this produces an absolute maximum weight capacity of 2.1 mg per foot, which is somewhat further reduced by out-of-plane compliance of the lateral actuator arrays. Fortunately, each actuator array has a capacitance of only 1.2 nF, such that power consumption of three actuators at 15 V with a 15 Hz step frequency is only 12 μW. This translates to an ability to operate with battery power densities as low as 5.7 W/kg, well below that of current battery technologies. In practice, the ability to successfully operate a robot leg of this type with a power supply that it can carry is more dependent on efficient use of energy in any control and energy conversion circuitry, than on its own fundamental power consumption [85].

Still, for the immediate development of micro-robotic prototypes, the current work's primary benefits are the increased reliability of thin-film PZT actuator arrays and verification of actuator array modeling techniques. This process has produced a prototype hexapod using the leg design analyzed has been produced with 5 out of 6 legs intact (one leg failing due to fracture of a flexure/tether unit during fabrication). Moving forward, however, more feasible robot prototypes for the next phase of further robot development will utilize millipede-style layouts, with larger numbers of legs, fewer actuators per leg,

and shorter distances to leg tips to be explored. These prototypes thus trade reduced mobility for larger weight bearing capacity (up to approximately 200 mg for an entire chassis) to allow greater flexibility in control and power systems. Nonetheless, the ability to create as complex leg geometries as described here while meeting fundamental needs for energy use versus weight bearing capacity, and the ability to predict leg behavior given fabrication constraints, appears encouraging for a long-term goal of highly-mobile, bio-inspired micro-scale robots.

3.7 Summary and Conclusion

Prototype micro-robotic leg joint arrays capable of producing multiple-degree of freedom motion are modeled and characterized in this chapter. Thin-film PZT lateral and vertical actuators are integrated with complex 3D silicon structures encapsulated by silicon oxide vertical barrier trenches that are deposited prior to PZT deposition. Consistent undercut length of thin-film PZT actuators array was obtained with minimal effect on the piezoelectric performance of the actuators, allowing the complex leg joints in this chapter to be formed. The intended motion generated by the proposed multi-DoF microrobotic leg is larger than the final leg structure due to the remained silicon oxide vertical barrier trenches. The final vertical actuators exert 37^0 rotational displacements at 15V DC, resulting in 148μm deflection of the hip joint. An inner lateral actuator array exerts 0.1^0 in-plane and 18^0 vertical rotation with respect to the hip joint, due to imperfections in the fabrication process impeding in-plane motion and accentuating out-of-plane motion, while the outer lateral actuator array exerts 3.85^0 in-plane rotation, more consistent with actuator array models. Improvement to this current design and fabrication

of thin-film PZT devices is intended to support future microrobotic chassis development. Micro-robotic joint modeling includes compensation for intrinsic residual stress of thin-film stacks that changes the initial deflection of the actuator arrays, the behavior of in-plane flexure joint array structures when the width of oxide trench barrier is taken into consideration, and the design of an electrical interconnect structure connected with the outer compact actuator array with less impact on the final device motion.

CHAPTER IV

Design for Robust Finite Duration Transient Response of Piezoelectric Micro Actuator Structures

4.1 Background

While the performance of many dynamic systems may deviate from designed specifications due to variation in actual system parameters from their designed values, this is a particular concern for micro-electromechanical systems (MEMS). MEMS components and devices often exhibit substantial variation from feature-to-feature or part-to-part due to relatively large variation in microfabrication processing outcomes. For example, it is common for deep reactive-ion etching (DRIE) to produce 10% or larger variations in etching distance or side-wall uniformity [101]. A large number of parametric variations due to such processing uncertainty or other factors, such as environmental conditions, can easily affect device performance. Nonetheless, many micro-scale dynamic systems are intended to produce repeatable, finite-duration, specified movements in response to specified stimulus. Substantial response variation due to parameter variation from device to device often forces relatively conservative device operation or leads to error in the device response. Examples of such systems where this occurs include micro-electromechanical switches, digital micro-mirrors, and micro-robotic appendages.

This chapter will explore a design technique for reducing variation in transient responses of microactuators that may arise due to geometric or material property variation. Typical performance measures for the transient response of a dynamic system include rising time, settling time, overshoot and stability. The transient behavior up to a specific point in time, such as the peak time or settling time, is of great interest for the application of MEMS switches [47], MEMS logic gates [71], [72], and micro-robots [70]. For example, since dielectric charging is the most important source of failure in MEMS capacitive switches [113], previous researches [113] [114] demonstrated a modeling approach as well as measurement approach that focused on the transient response of the charging model. Although the goal of the study in [113] [114] was not aimed at design of robust transient response of the switch devices, the study of transient behavior of the charging model was performed when the critical parameters are the gap, the dielectric thickness, and the air/dielectric conductivity. For the improvement of the device reliability, such as the switching lifetime of repetitive ohmic contact [47], the study is then useful in design optimization of new MEMS switch development.

In the micro-robotic application shown in Figure 1.1, the transient response is the most important dynamic behavior of piezoelectrically actuated legs. The micro-robotic legs are desired to exert faster peak time for high-speed forward or return motion of the robotic platform. Also, multiple legs are desired to have robust transient responses to coordinate motion in hexapod or millipede robotic platforms in the presence of processing variation during manufacturing, and against environmental variation or disturbances during walking operation. To achieve the robust transient responses of multiple legs when all legs are identical, previous works in [56] and [81] focused on

control strategies when optimal transient behavior is considered for a robotic leg, and a system-level optimization of power consumption is conducted. In this chapter, the finite-time transient behavior up to peak time is considered, as the maximum displacement of a damped dynamic response is obtained at the peak time under a given input voltage. Compared to previous works in [56] [81], the robustness of finite-time transient response is considered in the presence of the parametric uncertainties before control is implemented. For situations where feedback control is unavailable due to power constraints, the robust design of the open loop plant transient response is considered without control, although the ability to reduce sensitivity to model variation in purely open-loop operation is limited.

Here, analysis techniques inspired by the design of robust feedback controllers are applied to optimize design parameters of dynamic systems subject to substantial parametric variation, reformulating such techniques to emphasize finite duration and open-loop movements. In comparison, previous works on robust design techniques for micro-scaled dynamic systems can be grouped into two approaches: robust open-loop design and robust feedback control design approaches. The former approach is typically based on a multi-objective constrained optimization and open loop dynamics are directly optimized without feedback control implementation. One sample optimization problem is to match the natural frequency that is represented in a random vector to a predefined natural frequency when the effect of variant natural frequency is minimized [39]. An ellipsoidal approach to objective function minimization was also applied to obtain the optimal parametric dimensions of a dog-bone suspension structure in [4], and other device-specific performance objectives are chosen in [103], [104], and [105]. In robust

feedback control design approaches, robust design techniques, such as H_∞ minimization, mixed H_2/H_∞ control and μ-synthesis (structured singular values), are employed [43-45], [48], [50]. Li et al., for example, proposed an adaptive dynamic surface control and H_∞ control technique to ensure robust tracking of a parallel-plate electrostatic actuator in the presence of parametric uncertainty and external disturbance [48]. Zhu et al. used backstepping control design for an electrostatic actuator with uncertain parameters [50].

Meanwhile, other previous robust transient controller designs [31], [51] - [55] exist in the controls literature for non-microsystems applications. From the robust performance of the transient response perspective, a linear time-invariant system is represented in the form of a generalized plant in [31]. Uncertainties in parameters of the lumped modeled plant, linearization error, and unmodeled dynamics are assumed. And previous work on DIA (Disturbance and Initial-state Attenuation) control [106] was used to generate the initial controller in an iterative optimization, and a D-K iterative calculation for controller synthesis was applied with the initial controller being set up with H_∞ DIA in the iteration to attenuate the disturbances and the nonzero initial state uncertainties. In [51], an affine model of a perturbed system was considered and the solution matrices that satisfy sufficient conditions of finite-time boundedness were solved using a linear matrix inequality (LMI) to find the state feedback gain. Design methods for state feedback and observer-based output feedback with input constraints were proposed in [52] where a discrete-time system and physical limitations on feedback control are concerned. In [54], a high-gain observer-based controller recovered the performance of the tracking error in transient response under uncertainty by cancellation of estimated perturbation, and also had an integral action property to regulate the tracking error to zero

in the presence of non-vanishing perturbation. In [53], a proposed inner-loop controller and the overall closed-loop system were transformed to a singular perturbation form and the multi-variable circle criterion for the perturbed system matrix in the linear system.

One of the limitations of the aforementioned approaches of the controller design is that they are applicable for infinite horizon cases. In contrast, as noted earlier due to short operating duration of many MEMS devices, such as MEMS switches [47], MEMS logic gate [71], [72], micro-robots [70], transient behavior is often the most important aspect in dynamic performance [46], [47]. In response, finite-time control design, with fewer previous examples such as [52] where finite-time state feedback control and observer-based output feedback control are concerned, can be considered to overcome such a limitation.

This work proposes a design technique for improving robust finite-time transient response of a micro-fabricated mechanical structure. From the deterministic point of view, a simple estimated bound for the maximum possible deviation of the continuous finite-time response is obtained and a gradient-based optimization method is applied to minimize the estimated bound. For a solely open-loop system design, good performance is defined as a minimal maximum deviation from the nominal response. An optimal geometry for a micro-scaled mechanical structure is searched for over the possible range of feasible design parameters to minimize that deviation. To do so, the optimization problem is converted to an eigenvalue problem in which the bound of the good performance over a finite duration in time is obtained as a time-varying matrix. In addition, the system matrices are converted into an upper linear fractional transformation (LFT), which in turn is converted to a structured singular value (SSV) problem. From

conventional robust controller design techniques, a SSV solver used for robust stability analysis and for robust controller design via μ-synthesis is applied. Here, μ-synthesis is a technique for design of stabilizing controllers by minimizing the maximum structured singular value of the closed loop system [63]. Finally, in two test case studies MEMS components are optimized by the methods developed: these case studies consider the open- and closed-loop transient responses of a bulk-PZT actuated micro-robotic leg, and the open-loop transient response of a thin-film PZT actuated micro-robotic leg. In addition to transient response robustness for the second case study, the maximum stroke angle of the micro-robotic leg array is also considered in optimization, as a combination of nominal and perturbed objective functions.

4.2 Approach to Minimizing Upper Bound of Finite-Time Transient Error

4.2.1 Performance Objective for Robust Finite Time Transient Response

In this section, a technique for increasing robustness of transient responses of MEMS system dynamics to parameter variation is examined, both for open-loop operation and when control is implemented. This can simplify control tasks among MEMS devices where repeated transient motions are utilized. The optimization procedure is based on minimization of a robust performance measure over a finite duration, in continuous rather than discrete time, and then a search for the best nominal parameters. These parameters may include dimensions of structural elements during plant design or a feedback gains for control design. A Linear Perturbed System (LPS) is defined in Eq. 4.1, where A_Δ is n-by-n matrix defined as the sum of a nominal state

matrix, A_0, and a deviation term, ΔA, and B_Δ is n-by-1 matrix defined in as the sum of a nominal input matrix, B_0, and a deviation term, ΔB.

$$\begin{aligned} \dot{x} &= A_\Delta x + B_\Delta u \\ y &= Cx = x \end{aligned} \tag{4.1}$$

Given this system definition, the system design problem for the robust finite-time transient response of a LPS is defined in the following performance objective function:

$$\min_{\Theta} \max_{\Delta} J(t) = \min_{\Theta} \max_{\Delta} \int_0^t e(t)^T \, R \, e(t) \, dt \tag{4.2}$$

where $e(t)$ is defined as the difference between the perturbed state, $x_\Delta(t)$, and the nominal state, $x_0(t)$ of a system in Eq. 4.1, θ represents the design variables of the plant (such that A_0 and B_0 are functions of θ), and Δ represents the parametric perturbation of A_Δ and B_Δ.

The optimization problem in Eq. 4.2 can be approximately solved by the minimization of the maximum eigenvalue of a certain matrix, $Q(t)$, which in turn can be represented by a linear fractional transformation (LFT), $F_u\left(P(t), \Delta\right)$, where $P(t)$ and Δ are as follows:

$$P(t) = \begin{bmatrix} P_{11} & P_{12} \\ P_{21} & P_{22} \end{bmatrix}$$

$$P_{11} = \begin{bmatrix} M_{-M_1R^{-1}}\Big|_{11} & M_{-M_1R^{-1}}\Big|_{12} \cdot \left(augM^2_{M_2}\right)^T\Big|_{21} \\ 0 & \left(augM^2_{M_2}\right)^T\Big|_{11} \end{bmatrix}, \quad P_{12} = \begin{bmatrix} M_{-M_1R^{-1}}\Big|_{12} \cdot \left(augM^2_{M_2}\right)^T\Big|_{22} \\ \left(augM^2_{M_2}\right)^T\Big|_{12} \end{bmatrix} \tag{4.3}$$

$$P_{21} = \begin{bmatrix} M_{-M_1R^{-1}}\Big|_{21} & M_{-M_1R^{-1}}\Big|_{22} \cdot \left(augM^2_{M_2}\right)^T\Big|_{21} \end{bmatrix}, \quad P_{22} = M_{-M_1R^{-1}}\Big|_{22} \cdot \left(augM^2_{M_2}\right)^T\Big|_{22}$$

The relation between Eqs. 4.1 and 4.3 and the minimization problem of the eigenvalue of a matrix Q(t), as well as the conversion to upper LFT shown in Figure 4.1 are derived in the next section.

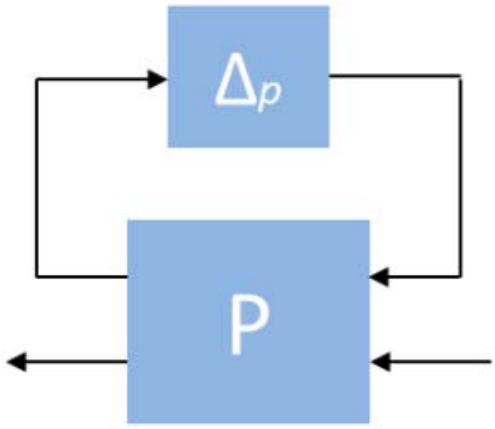

Fig. 4.1 Linear fractional transformation

4.2.2 Derivation of the Upper Bound of Performance Objective

In this section, the upper bound of the performance objective, *J*, for the linear perturbed system in Eq. 4.1 and 4.2 is obtained for the case without feedback control. The closed loop case with a state feedback gain is presented in Section 4.2.5. The performance index is reformulated to minimize the effects of parameter uncertainty on perturbed finite-time transient responses without a control effort. Uncertainties in initial conditions of the state and in input are assumed to be norm-bounded in this analysis.

For an n-dimensional linear system, a system with perturbed and nominal parameters is shown in Eq. 4.4:

$$\begin{aligned}
\dot{x}_{\Delta}(t) &= \left(A_0 + \Delta A\right)x_{\Delta}(t) + \left(B_0 + \Delta B\right)u(t) = A_{\Delta}x_{\Delta}(t) + B_{\Delta}u(t) \\
\dot{x}_0(t) &= A_0 x_0(t) + B_0 u(t) \\
y(t) &= Cx(t)
\end{aligned} \tag{4.4}$$

where x_{Δ} and x_0 are the perturbed and nominal states of a plant, A_0 and B_0 are nominal state and input matrices, ΔA and ΔB are deviation of A_0 and B_0, A_{Δ} and B_{Δ} are resulting perturbed state and input matrices respectively, and C is the output vector.

The difference, e, between the nominal, x_0, and perturbed response, x_{Δ}, of the system, and the weighted error, e_s, which is represented in terms of a weighting factor, κ, and a corresponding coordinate matrix, S, are defined as follows:

$$e = x_{\Delta} - x_0 \ , \ \ e_s = \kappa S\, e \tag{4.5}$$

A positive definite weighting matrix, R, is then defined to emphasize the importance of specific states in x_0 during the parametric optimization:

$$R = S^T \kappa^2 S \tag{4.6}$$

For a given specification of nominal, target transient behavior, the performance index, J, is proposed as a quadratic function of error between the nominal and perturbed output of the system over finite duration time t_p, and is represented by the following minimization:

$$\min_{\Theta} \max_{\Delta} J\left(t_p\right) = \min_{\Theta} \max_{\Delta} e\left(t_p\right)^T \, R \, e\left(t_p\right) \tag{4.7}$$

where θ is a set of design variables, and Δ represents the parametric uncertainty.

Given the objective function in Eq. 4.7, the quadratic function of error will be shown to be bounded from above by a bound $J_{ub}(t_p)$ on cost $J(t_p)$ that is itself obtained by solving an eigenvalue problem. The nominal state, $x_0(t)$, with initial condition, $x_0(0)$, is:

$$x_0\left(t\right) = \mathrm{e}^{At}\, x_0\left(0\right) + A^{-1}\left(\mathrm{e}^{At} - I\right)Bu \tag{4.8}$$

Differentiating the error, we obtain:

$$\dot{e}(t) = (A + \Delta A)e(t) + \Delta A x_0 + \Delta B u \tag{4.9}$$

$$\dot{e}_s(t) = S(A + \Delta A)S^{-1}e_s(t) + \kappa S \Delta A x_0 + \kappa S \Delta B u \tag{4.10}$$

And the cost and differentiated cost in terms of the *s* coordinate are:

$$J = e^T R\, e = e^T S^T \kappa^2 S\, e = {e_s}^T e_s \tag{4.11}$$

$$\begin{aligned} \dot{J} = {\dot{e}_s}^T e_s + {e_s}^T \dot{e}_s &= \left(S(A + \Delta A)S^{-1}e_s(t) + \kappa S \Delta A x_0 + \kappa S \Delta B u\right)^T e_s \\ &\quad + {e_s}^T \left(S(A + \Delta A)S^{-1}e_s(t) + \kappa S \Delta A x_0 + \kappa S \Delta B u\right) \\ &= {e_s}^T \left(\left(S(A + \Delta A)S^{-1}\right)^T + S(A + \Delta A)S^{-1}\right)e_s + \left(\kappa S \Delta A x_0 + \kappa S \Delta B u\right)^T e_s \\ &\quad + {e_s}^T \left(\kappa S \Delta A x_0 + \kappa S \Delta B u\right) \end{aligned} \tag{4.12}$$

The effect of unknown factors on initial condition and input are assumed to be norm-bounded:

$$\begin{aligned} \left\|x_0(0)\right\| \le x_{0,\max} \quad \text{or} \quad x_{0,i}(0)^2 \le {x_{0,i,\max}}^2 \\ \left\|u(t)\right\| \le u_{\max} \quad \text{or} \quad u(t)^2 \le {u_{\max}}^2 \end{aligned} \tag{4.13}$$

And the upper bound of the initial condition and input, x_{0max} and u_{max}, are obtained in Eq. 4.14, where the coordinate matrices, W_x and W_u, are defined in Eq. 4.15:

$$\begin{bmatrix} 1/{x_{0,1,\max}}^2 & & & \\ & \ddots & & \\ & & 1/{x_{0,n,\max}}^2 & \\ & & & 1/{u_{\max}}^2 \end{bmatrix} = \begin{bmatrix} {W_x}^T W_x & \\ & {W_u}^T W_u \end{bmatrix} \tag{4.14}$$

$$\begin{aligned} &x_0 = {W_x}^{-1} x_{0w}\ , \quad u = {W_u}^{-1} u_w \\ &x_{0w}(t) = \mathrm{e}^{W_x A {W_x}^{-1} t}\, x_{0w}(0) + \left(W_x A {W_x}^{-1}\right)^{-1} \left(\mathrm{e}^{W_x A {W_x}^{-1} t} - I\right)\left(W_x B {W_u}^{-1}\right) u_w \end{aligned} \tag{4.15}$$

Here, W_x and W_u satisfy the norm bound condition in Eq. 4.16, which ensure that the deviations of initial states and input are norm-bounded:

$$\begin{bmatrix} x(0)^T & u \end{bmatrix} \begin{bmatrix} W_x{}^T W_x & 0 \\ 0 & W_u{}^T W_u \end{bmatrix} \begin{bmatrix} x(0) \\ u \end{bmatrix} \le n+1 \tag{4.16}$$

From Eq. 4.11 and 4.12, the differentiated cost and the upper bound of the cost are represented in Eq. 4.17 and 4.19, respectively:

$$\dot{J} = \begin{bmatrix} e_s{}^T & x_{0w}(0)^T & u_w{}^T \end{bmatrix} M \begin{bmatrix} e_s \\ x_{0w}(0) \\ u_w \end{bmatrix} \tag{4.17}$$

where the components of a matrix, M, are:

$$\begin{aligned} M_{11} &= \left(S(A+\Delta A)S^{-1} \right)^T + S(A+\Delta A)S^{-1} \\ M_{12} &= M_{21}{}^T = \left(\kappa S \Delta A W_x{}^{-1} \mathrm{e}^{W_x A W_x{}^{-1} t} \right) \\ M_{13} &= M_{31}{}^T = \left(\kappa S \Delta A W_x{}^{-1} \left(W_x A W_x{}^{-1} \right)^{-1} \left(\mathrm{e}^{W_x A W_x{}^{-1} t} - I \right) \left(W_x B W_u{}^{-1} \right) + \kappa S \Delta B W_u{}^{-1} \right) \\ M_{22}, M_{23}, M_{32}, M_{33} &= 0 \end{aligned} \tag{4.18}$$

Leading to upper bound:

$$\begin{aligned} J &= \begin{bmatrix} e_s{}^T & x_{0w}(0)^T & u_w{}^T \end{bmatrix} blkdiag(I,0,0) \begin{bmatrix} e_s \\ x_{0w}(0) \\ u_w \end{bmatrix} \le \begin{bmatrix} e_s{}^T & x_{0w}(0)^T & u_w{}^T \end{bmatrix} W \begin{bmatrix} e_s \\ x_{0w}(0) \\ u_w \end{bmatrix} \\ &\le J + n + 1 = J_a \end{aligned} \tag{4.19}$$

where

$$W = \begin{bmatrix} I & & \\ & W_x{}^T W_x & \\ & & W_u{}^T W_u \end{bmatrix} \tag{4.20}$$

By introducing the diagonal W-matrix, a quotient ratio is obtained with respect to a concatenated unified vector of e_s, x_{0w} and u_w in Eq. 4.21, below:

$$\dot{J}/J_a \le \lambda_{\max}\left(M\,W^{-1}\right) = \lambda_{\max}\left(Q_a\right) \tag{4.21}$$

Therefore, the estimated upper bound of the cost with respect to the concatenated coordinate of e_s, x_{0w}, and u_w is obtained from the maximum eigenvalue of time-varying matrix, Q_a. More details of the optimization procedure are discussed in section 4.3.

4.2.3 Conversion of Performance Objective Upper Bound to Linear Fractional Transformation

In this section, an upper linear fractional transformation (LFT) form of the eigenvalue minimization problem is obtained in terms of nominal and perturbed parameters. All nominal system parameters are shown in the P matrix while parametric uncertainty description is separated into the Δ matrix [59], [60]. This can be useful in the case of high-order systems with many sources of uncertainty for formulating the perturbed parameter model. In addition to the upper bound estimation of a cost with norm-bound initial condition perturbation and input from the previous section, the worst case analysis of a cost with parametric uncertainty can be further obtained when the maximum eigenvalue of a time-varying matrix is represented in an upper LFT form.

From Eq. 4.21, Q_a is represented in LFT:

$$Q_a = F_u\left(P,\Delta\right) = \begin{bmatrix} M_{11} & M_{12}\left(W_x{}^T W_x\right)^{-1} & M_{13}\left(W_u{}^T W_u\right)^{-1} \\ M_{21} & 0 & 0 \\ M_{31} & 0 & 0 \end{bmatrix} \tag{4.22}$$

where P and Δ are split into partitioned matrices:

$$P_{22} = \begin{bmatrix} \left(SAS^{-1}\right)^T + SAS^{-1} & 0 & 0 \\ 0 & 0 & 0 \\ 0 & 0 & 0 \end{bmatrix} \tag{4.23}$$

$$P_{21} = \begin{bmatrix} \begin{bmatrix} \left(S^{-1}\right)^T & S \end{bmatrix} & \kappa S & \begin{bmatrix} \kappa S & \kappa S \end{bmatrix} & 0 & 0 \\ 0 & 0 & 0 & \left(W_x^{-1} \mathrm{e}^{W_x A W_x^{-1} t}\right)^T & 0 \\ 0 & 0 & 0 & 0 & \begin{bmatrix} W_x^{-1}\left(W_x A W_x^{-1}\right)^{-1}\left(\mathrm{e}^{W_x A W_x^{-1} t} - I\right)\left(W_x B W_u^{-1}\right) \\ W_u^{-1} \end{bmatrix}^T \end{bmatrix} \tag{4.24}$$

$$P_{12} = \begin{bmatrix} \begin{bmatrix} S^T \\ S^{-1} \end{bmatrix} & 0 & 0 \\ 0 & W_x^{-1} \mathrm{e}^{W_x A W_x^{-1} t}\left(W_x^T W_x\right)^{-1} & 0 \\ 0 & \begin{bmatrix} W_x^{-1}\left(W_x A W_x^{-1}\right)^{-1}\left(\mathrm{e}^{W_x A W_x^{-1} t} - I\right)\left(W_x B W_u^{-1}\right)\left(W_u^T W_u\right)^{-1} \\ W_u^{-1}\left(W_u^T W_u\right)^{-1} \end{bmatrix} & \\ \left(\kappa S\right)^T & 0 & 0 \\ \begin{bmatrix} \left(\kappa S\right)^T \\ \left(\kappa S\right)^T \end{bmatrix} & 0 & 0 \end{bmatrix} \tag{4.25}$$

$$\Delta = diag\left(\left[\Delta_A^T, \Delta_A, \Delta_A, \Delta_A, \Delta_B, \Delta_A^T, \Delta_A^T, \Delta_B^T\right]\right) \tag{4.26}$$

and P_{11} is a zero matrix. Then, minimizing the upper-bound of the eigenvalue of $Q_a(t_p)$ under uncertainties can be achieved by minimizing the structured singular value of M_Q matrix with respect to an augmented uncertainty structure, which can reduce the complexity of setting up the optimization problem for high-order systems. Still, the separation of the nominal parametric terms, represented in P-matrix with the expanded diagonal P_{21}, and the perturbed terms, represented in Δ-matrix, has potential limitations,

such as increasing in the size of the *P*-matrix and making μ-synthesis results more conservative.

4.2.4 Conversion of LFT-Represented Upper Bound to Structured Singular Value

The structured singular value (SSV) of a matrix is defined in [59], where $\mu_{\Delta V}$ is the structured singular value of V with respect to Δ_V, and $\bar{\sigma}$ is the maximum singular value:

$$\mu_{\Delta_V}(V) = \frac{1}{\min_{\Delta}\left(\bar{\sigma}(\Delta_V) : \Delta_V \in \mathbf{B}\Delta,\ \det(I - M\Delta_V) = 0\right)} \tag{4.27}$$

It is known from the Main Loop Theorem [59], that when $\beta > 0$ is given,

$$\mu_{\Delta_{aug}}(P) < \beta \quad \Leftrightarrow \quad \begin{cases} \mu_{\Delta_P}(P_{11}) < \beta \\ \max_{\Delta_P} \mu_{\Delta_{fic}}\left(F_u(P, \Delta_P)\right) < \beta \end{cases} \tag{4.28}$$

where Δ_P and Δ_{fic} are the uncertainty blocks that are compatible in size to P_{11} and P_{22}, respectively, and Δ_{aug} is defined:

$$\Delta_{aug} = \begin{bmatrix} \Delta_P & 0 \\ 0 & \Delta_{fic} \end{bmatrix} \tag{4.29}$$

The spectral radius, ρ, of V is intimately related to the SSV when the uncertainty block satisfies the condition:

$$\text{If } \Delta_V = \{\delta I : \delta \in C\}, \quad \text{then } \mu_{\Delta_V}(V) = \rho(V) \tag{4.30}$$

Thus, the relation of spectral radius to SSV is used to minimize the proposed performance index by the condition in Eq. 4.30:

$$\text{Let } \Delta_{fic} = \{\delta I : \delta \in C\}, \text{ then } \mu_{\Delta_{fic}}\left(F_u(P, \Delta_P)\right) = \rho\left(F_u(P, \Delta_P)\right) \tag{4.31}$$

Therefore, minimizing weighted error in the transient response over finite duration is converted to minimization of the upper bound of the structured singular value with respect to uncertainty structure, Δ_{aug}:

$$\mu_{\Delta_{aug}}(P) < \beta \quad \Leftrightarrow \quad \begin{cases} \mu_{\Delta_P}(P_{11}) < \beta \\ \max\limits_{\Delta_P} \rho(F_u(P, \Delta_P)) = \max\limits_{\Delta_P} \rho(Q_a) < \beta \end{cases} \tag{4.32}$$

In turn, a design simulation of robust finite-duration transient response based on SSV is equivalent to the conventional robust performance analysis available in MATLAB [63]

4.2.5 Design Technique for Robust Finite Time Transient Response with State Feedback

Although all states in the dynamic response of micro-devices are not always measurable, in this section the comparable optimization problem to the previous sections is formulated when state feedback is available to the system. The quadratic cost function is formulated as the sum of error components over a finite time span, with the optimization problem of minimizing the least upper bound of the quadratic function represented in terms of the eigenvalue of a certain matrix. Similar to the design technique in section 4.2.1 – 4.2.4, this allows for a linear fractional transformation form by which the nominal and uncertain parameters are separated into P and Δ matrices, analogous to standard LFT representations for robust controller design. The structured singular value, μ_Δ, is replaced by the spectral radius of the LFT-expressed matrix in the P-Δ configuration.

For an n-dimensional linear system where all states are assumed to be measurable during controller design, a system with perturbed and nominal parameters and a feedback signal with state feedback gain, K_{FB}, are represented:

$$\left.\begin{aligned}
&\dot{x}_{p\Delta}(t) = \left(A_0 + \Delta A\right)x_{p\Delta}(t) + \left(B_0 + \Delta B\right)u(t) \\
&\qquad = A_\Delta x_{p\Delta}(t) + B_\Delta u(t) \\
&\dot{x}_{p0}(t) = A_0 x_{p0}(t) + B_0 u(t) \\
&y(t) = Cx(t) \\
&u\left(t\right) = r + K_{FB}x\left(t\right)
\end{aligned}\right\} \qquad (4.33)$$

$$\dot{x}_{cl}\left(t\right) = \left(A_\Delta + B_\Delta K_{FB}\right)x_{cl}\left(t\right) + B_\Delta r$$

where $x_{p\Delta}$ and x_{p0} are the perturbed and nominal states of a plant, x_{cl} is the nominal state of a closed loop system, A_0 and B_0 are nominal state and input matrices, ΔA and ΔB are deviation of A_0 and B_0, respectively, A_Δ and B_Δ are resulting perturbed state and input matrices, and r is the reference input. The output vector, C, is assumed to be invertible, producing a vector of outputs that are linear combinations of the states, y.

Similar to the previous sections, the optimization problem can be converted to a minimization problem of the maximum eigenvalue of a certain matrix, $Q(t)$, which is also converted to linear fractional transformation (LFT). Here, the initial states are assumed to be non-perturbed nominal initial conditions. Then as shown in Eq. 4.32, the optimization problem can be converted to minimizing the structured singular value of P matrix with respect to an augmented uncertainty structure, Δ_{aug}, which allows simple preparation of the optimization problem for high-order systems:

$$P = \begin{bmatrix} P_{11} & P_{12} \\ P_{21} & P_{22} \end{bmatrix}, \quad \Delta_P = \begin{bmatrix} \Delta & & & \\ & \Delta & & \\ & & \Delta^T & \\ & & & \Delta_f \end{bmatrix}, \quad \Delta_{aug} = \begin{bmatrix} \Delta_P & \\ & \Delta_{fic} \end{bmatrix}$$

$$P_{11} := \begin{bmatrix} \begin{bmatrix} M_{MK_{11}} & \\ & M_{MK_{11}}{}^T \end{bmatrix} & \begin{bmatrix} M_{MK_{12}} C^{-1} R^{-1} \\ M_{MK_{21}}{}^T C \end{bmatrix} \Gamma_K \\ & \begin{bmatrix} \begin{bmatrix} 0_n & \\ & 0_{nx1} \end{bmatrix} & \\ & I_n \end{bmatrix} \end{bmatrix}, \quad P_{12} := \begin{bmatrix} \begin{bmatrix} M_{MK_{12}} C^{-1} R^{-1} Z \\ M_{MK_{21}}{}^T CZ \end{bmatrix} \\ \begin{bmatrix} \begin{bmatrix} RC \end{bmatrix}^T \\ \begin{bmatrix} RC \end{bmatrix}^T \end{bmatrix} \\ 0_n \end{bmatrix} \tag{4.34}$$

$$P_{21} := \begin{bmatrix} \begin{bmatrix} RC M_{MK21} & C^{-1} M_{MK12}{}^T \end{bmatrix} & \Omega_K \Gamma_K \end{bmatrix}, \qquad P_{22} := \Omega_K Z$$

where all terms, such as Δ, Δ_f, M_{MK}, Γ_K, Ω_K and Z, are functions of the nominal system or uncertainty structure, as defined in Appendix B.

The difference between the nominal, x_{cl0}, and perturbed response, $x_{cl\Delta}$, of the closed loop system and a positive definite weighting matrix, R, are defined as follows, assuming the same initial conditions:

$$\begin{aligned} e &= \left(x_{cl\Delta} - x_{cl0} \right) \\ &= \left(\exp^{\left(A+\Delta A+BK_{FB}+\Delta BK_{FB}\right)t} x_{cl\Delta}(0) - \exp^{\left(A+BK_{FB}\right)t} x_{cl0}(0) \right) \\ R &= \begin{bmatrix} \alpha_1 & & 0 \\ & \ddots & \\ 0 & & \alpha_n \end{bmatrix} \end{aligned} \tag{4.35}$$

where the positive real numbers, α_1 to α_n, are weighting factors for error components in each output. Then, the quadratic function of error will be shown to be bounded from above by the bound $J_{ub}(t_p)$. Differentiating the error, we obtain:

$$\begin{aligned} \dot{e} &= \left(A + \Delta A + BK_{FB} + \Delta BK_{FB} \right) \exp^{\left(A+\Delta A+BK_{FB}+\Delta BK_{FB}\right)t} x_{cl\Delta}(0) \\ &\quad - \left(A + BK_{FB} \right) \exp^{\left(A+BK_{FB}\right)t} x_{cl0}(0) \\ &= \left(A + BK_{FB} + \Delta A + \Delta BK_{FB} \right) e + M_0 \end{aligned} \tag{4.36}$$

where

$$M_0 = \left(\Delta A + \Delta B K_{FB}\right) \exp^{\left(A + B K_{FB}\right) t} x_{cl0}\left(0\right) \tag{4.37}$$

Note that the exponential term is no longer dependent on parameter variation and can be obtained only in terms of the nominal system during worst-case performance analysis. In addition, for small time response, M_0 can be reduced to a sum of matrices by Picard series:

$$M_0 \cong \left(\Delta A + \Delta B K_{FB}\right)\left(I + \left(A + B K_{FB}\right) t\right) x_{cl0}\left(0\right) \quad \text{for } t \ll 1 \tag{4.38}$$

By differentiating the performance index with respect to time, it can be shown that the ratio of the derivative of the performance index to itself is bounded by the minimum and maximum eigenvalues of a certain matrix, $Q(t)$, by Rayleigh's quotient as follows:

$$\begin{aligned}
\dot{J}\left(t\right) &= e^T R\, \dot{e} + \dot{e}^T R\, e \\
&= e^T R \left(A_\Delta + B_\Delta K_{FB}\right) e + e^T \left[\left(A_\Delta + B_\Delta K_{FB}\right)\right]^T R\, e \\
&\quad + e^T R M_0 + \left[M_0\right]^T R\, e \\
&= -e^T M_1\, e + \left(e^T M_2 + {M_2}^T e\right)
\end{aligned}$$

where

$$\begin{aligned}
M_1 &= -R\left(A + B K_{FB} + \Delta A + \Delta B K_{FB}\right) \\
&\quad - \left[\left(A + B K_{FB} + \Delta A + \Delta B K_{FB}\right)\right]^T R \\
M_2 &= R\left[M_0\right]
\end{aligned}$$

$$\therefore -\frac{\dot{J}(t)}{J(t)} = \frac{-e^T M_1 e + \left(e^T M_2 + {M_2}^T e\right)}{e^T R\, e} \geq \lambda_{\min}\left(Q\left(t\right)\right) \tag{4.39}$$

Now the derivation is very similar to of the open-loop case. Here, M_1 is a real symmetric matrix and $\lambda_{\min}$ is the minimum eigenvalue of Q(t) (and the negative of the maximum eigenvalue of Q(t)). To find the relation between Q(t) and the ratio of the

derivative of the performance index to itself, an augmented vector, $\vec{1}_{n\times 1}$, whose elements are 1 in its first entry and 0 in the remaining, is introduced to produce a quadratic form in terms of error, and the equivalent performance index is defined in terms of $e' := \begin{bmatrix} e^T & \vec{1}^T \end{bmatrix}^T$:

$$\begin{aligned}
&\dot{J}(t) = -e^T M_1 e + \left(e^T M_2 + {M_2}^T e\right) \\
&= \begin{bmatrix} e^T & \vec{1}^T \end{bmatrix} \begin{bmatrix} -M_1 & \begin{bmatrix} M_2 & 1_{n\times(n-m)} \end{bmatrix} \\ \begin{bmatrix} {M_2}^T \\ 1_{(n-m)\times n} \end{bmatrix} & 0_{n\times n} \end{bmatrix} \begin{bmatrix} e \\ \vec{1} \end{bmatrix} \\
&\Rightarrow e'^T M' e' = \dot{J}(t) \\
&J(t) = e^T R e = \begin{bmatrix} e^T & \vec{1}^T \end{bmatrix} \begin{bmatrix} R & 0 \\ 0 & I_{n\times n} \end{bmatrix} \begin{bmatrix} e \\ \vec{1} \end{bmatrix} - 1 \\
&= e'^T R' e' - 1 = J'(t) - 1
\end{aligned} \tag{4.40}$$

producing a relation in terms of Q(t):

$$\begin{aligned}
&-\frac{\dot{J}'(t)}{J'(t)} = \frac{e'^T M' e'}{e'^T R' e'} \geq \lambda_{\min}\left(Q(t)\right) = \lambda_{\min}\left(M' R'^{-1}\right) \\
&J'(t) \leq J'_0 \exp\left(-\lambda_{\min}\left(Q(t)\right) \cdot t\right) = J'_{ub}(t)
\end{aligned} \tag{4.41}$$

where M' is a real symmetric and R' is a positive definite real symmetric matrix, so that the sufficient conditions for Rayleigh's quotient are satisfied. Then, the lower bound of the ratio is the minimum eigenvalue of Q, and this becomes an optimal design variable that determines the upper bound of equivalent performance index J' at a finite end time. From the definition, the maximum and minimum eigenvalues of Q have the same magnitude but different signs, and therefore minimization of the proposed performance index is converted to the almost equivalent and easier to solve minimization of spectral radius of Q, $\lambda_{max}(Q)$:

$$\min_{\Theta} \max_{\Delta} \lambda_{\max}\left(Q(t)\right) \tag{4.42}$$

The conversion of the upper bound of the performance objective represented in Eq. 4.42 can be converted to Linear Fractional Transformation and to Structured Singular Value similar to the previous sections. The LFT representation is already shown in Eq. 4.34.

4.3 Parameter Optimization Procedure

In a general optimization procedure, an objective function, *f(x)*, is minimized subject to certain constraints, $g_i(x)$. For the specific optimization to minimize finite duration transient error, the objective function in Eq. 4.43 corresponds to the quadratic function of the error with a positive definite weighting matrix or a norm bounded signal of the error in Eq. 4.2, and the nonlinear inequality constraint function, $g_i(x)$, in Eq. 4.43 is defined as the deterministic lower and upper bound of the design parameters, $\bar{\theta}_{lb}$ and $\bar{\theta}_{ub}$, and any performance of the resulting structure. In the initialization step, the weighting matrix, *R*, and the reference design parameters, $\bar{\theta}^1$ are first chosen. Optimization is performed with two calculation loops. In the inner loop of optimization, the maximum perturbation of the upper bound of *J* is achieved via SSV computation over the uncertainty, Δ. More specifically, the uncertain parameters are defined in terms of nominal values and deviations in the Robust Control Toolbox in MATLAB. The Q_a matrix or A_Δ is then separated into a nominal matrix and an uncertainty matrix, and maximum deviation of parameters in Δ-matrix of SSV is extracted to compute the corresponding parameters of the maximum perturbation. Then the upper bound of

performance index is obtained. In the outer loop of optimization, the design parameters are updated, $\bar{\theta}^k$, at the kth step.

$$\begin{aligned} &\text{minimize } f(x) \\ &\text{subject to } g_i(x) \le 0, \quad i = 1,...,m \end{aligned} \tag{4.43}$$

4.4 Case Study I: Bulk PZT Actuated Micro-Robot Platform Design

4.4.1 Objectives

The first case described is that of finite-time transient response of a bulk-PZT ceramic actuator driven micro-robot with 0.92cm-by-1.02cm footprint as shown in Figure 4.2. This robotic leg joint is taken from a 100μm-thick silicon flexure joint micro-robot fabricated and assembled with bulk PZT ceramic actuator for prototyping purposes. This type of robot prototype is intended for early testing of robot gaits and power systems.

These robots feature enhanced weight-bearing capability of the joint structure compared to thin-film-actuated micro-robots, in order to produce prototype micro-robots with larger weight-bearing capacities and simpler fabrication requirements than the eventual thin-film PZT robots. By finding the optimal parametric dimension of the actuation structure and the feedback gain, the robust finite-time transient behavior of the closed loop response is co-optimized between structural dimensional design and controller parameters. This case study is intended to verify that the design technique in Eq. 4.42 reduces variability by using the upper bound of the performance measure in Eq. 4.2. Not only the planar motion but also the vertical motion of an example system is considered in the finite-time transient behavior when both planar and vertical motions of the system are determined by the dimension parameters. The standard H_∞ approach is

also considered as an optimization method for the open-loop case to compare the proposed technique in Eq. 4.42. Since this type of robot prototype possesses larger weight-bearing capacities and is capable of carrying power systems, design of feedback controller parameter is also performed in this case study.

The appendages of a bulk-PZT actuated micro-robot in Figure 4.2 and 4.3 consist of a base silicon understructure and flexure joint that are fabricated on an SOI wafer with a Cr/Au deposition, and bulk PZT stripes that are diced and bonded on top of the base silicon understructure with epoxy resin. Similar to the design of piggy-back actuators proposed for some hard disk drives [107], [108], the PZT-assembled silicon understructure is bended up and down along z-axis, and rotates along θ-axis by the input voltage shown in Figure 4.3.

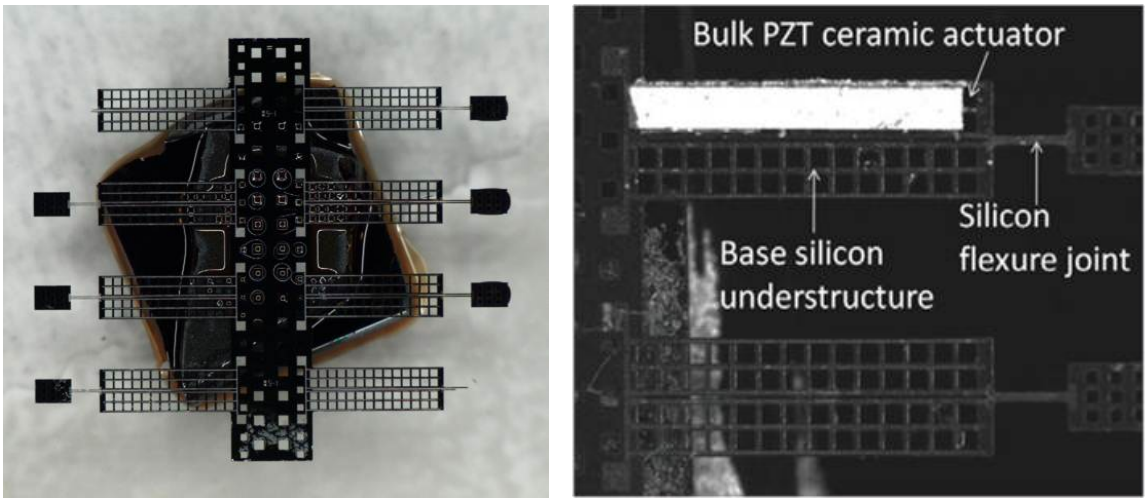

Fig. 4.2 Bulk PZT actuated micro-robotic platform with 0.92cm-by-1.02cm footprint (left), and an appendage of bulk PZT assembled silicon understructure (right)

For these bulk-PZT robot prototypes, a sample fabrication process, introduced in Appendix A, is used, and parametric error is introduced by hand assembly of a bulk PZT ceramic actuator to a base silicon understructure connected to the flexure joint, as well as

variance in silicon etching. Therefore, the design procedures will seek target dimensions of PZT ceramic actuator and of silicon flexure joint for the open-loop case, and the state feedback gain coefficient in addition to the structural dimensions for the closed-loop case so that transient motions of the joint are minimally sensitive to unknown dimensions or misalignment.

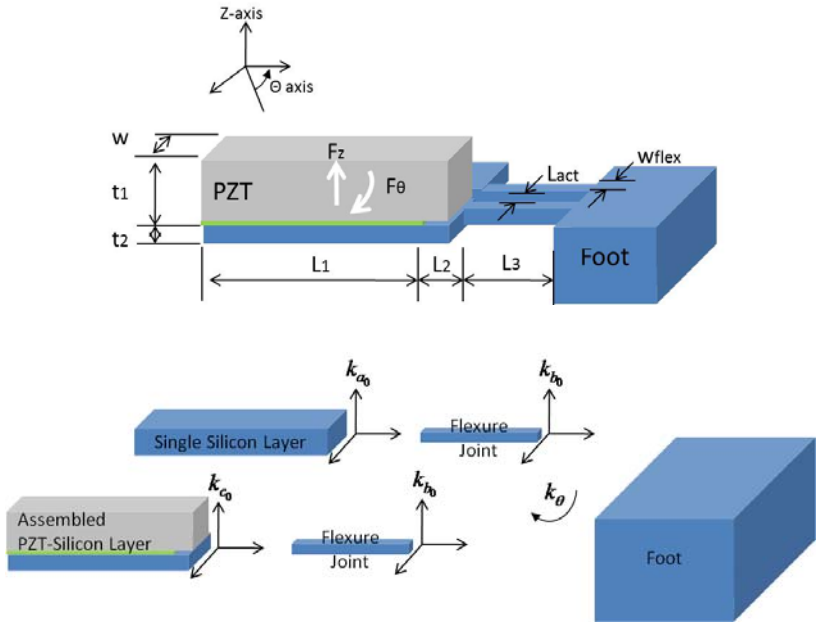

Fig. 4.3 Schematics of assembled PZT ceramic actuator on silicon flexure

4.4.2 Modeling of Bulk-PZT Actuated Micro-Robotic Leg

To perform a simulation study of leg joint parameter optimization, the dynamic equations of lateral and vertical motion are obtained in Eq. 4.44 and 4.49, where θ and z are the in-plane lateral angular displacement and out-of-plane vertical linear displacement, respectively. The set of nominal parameters are shown in Table 4.1. The design parameters are the width of PZT ceramic actuator, w, and of silicon flexure joint, w_1, the length of silicon base, L_1, and of silicon flexure joint, L_3, and the state feedback gain coefficient, K_{FB}.

The lumped parameter model for in-plane system dynamics is

$$J_{leg}\ddot{\theta} + b_{\theta}\dot{\theta} + k_{\theta}\theta = F_{\theta}^{'} \tag{4.44}$$

where J_{leg} is approximated by using lumped equivalent mass parameters, such as a micro-robotic foot, m_{foot}, the base silicon structure assembled with a PZT actuator, m_{Act+Si}, the base silicon structure without a PZT actuator, $m_{NoAct+Si}$, the silicon flexure joint, m_{flex}, and L_{CM} is the length of the center of mass of an entire leg:

$$J_{leg} \approx \left(m_{foot} + \frac{m_{Act+Si}}{3} + \frac{m_{NoAct+Si}}{3} + \frac{m_{flex}}{3} \right) L_{CM}^{\ 2} \tag{4.45}$$

The rotational spring stiffness, k_{θ}, is calculated from the system parameters as a combination of springs according to:

$$k_{\theta}^{\ -1} = f\left(L_1, L_3, L_{act}, w, w_{flex}\right) \tag{4.46}$$

where $f(L_1, L_3, L_{act}, w, w_{flex})$ are shown in Appendix B.

The out-of-plane dynamics are

$$m_{leg}\ddot{z} + b_{tot}\dot{z} + k_{tot}z = F_{z}^{'} \tag{4.47}$$

where m_{leg} is the total mass of a leg including a foot, two joint flexure, an assembled PZT-Si layer, and a single Si layer:

$$m_{leg} \cong m_{foot} + \frac{m_{Act+Si}}{3} + \frac{m_{NoAct+Si}}{3} + \frac{m_{flex}}{3} \tag{4.48}$$

The vertical spring stiffness, k_{tot}, is calculated from the individual spring stiffness and its deviation:

$$k_{tot} = f\left(k_{a0}, k_{b0}, k_{c0}, \Delta k_a, \Delta k_b, \Delta k_c\right) \tag{4.49}$$

The individual nominal spring stiffness, k_{a0}, k_{b0}, and k_{c0}, with perturbed terms, Δk_a, Δk_b, and Δk_c, are the vertical stiffness of a single base silicon understructure, of a flexure

joint, and of an assembled PZT-Si layer, respectively, as shown in Appendix B.

4.4.3 Robust Design Optimization of Bulk PZT Actuated Micro-Robotic Leg

Given the dynamic system defined by Eq. 4.44 and 4.47, with parametric uncertainties, the following design variables are optimized based on the framework introduced in section 4.2.5 to minimize finite-duration error in the leg response in a closed loop scenarios:

- Width of the PZT actuator, w
- Width of the silicon flexure joint, w_{flex}
- Length of the bonded PZT actuator onto the base silicon structure, L_1
- Length of the silicon flexure joint, L_3
- Feedback gain matrix, K_{FB}

In addition, a version of the optimization was done without a controller present to explore the ability to minimize error in open-loop responses. For a closed-loop reference design, used for comparison in Table 4.2, a constant gain negative state feedback controller was considered where gain matrix, K_{FB}, is designed with desired poles at [-500+164.3j; -500-164.3j; -400; -1] for less overshoot and smaller settling time compared to the reference open loop design. For the open-loop robust design, K_{FB} is eliminated and only the four structural dimensions are considered in gradient-based optimization. The weighting matrix, R, is chosen as [50 0 0 0; 0 100 0 0; 0 0 25 0; 0 0 0 50] in both open- and closed-loop cases to emphasize the maximization of in-plane rotational motion compared to the vertical displacement, and attenuate the velocity components compared

to the displacement components.

The results of the optimization show that increasing robustness of the design significantly reduces variation in the response due to parameter variation, even without changing the controller dramatically. While this can be useful for improving robustness of a controller even using simple controller designs, it should be noted that non-zero order robust controllers, such as H_∞ or mixed H_2/H_∞, should be compared in place of the state feedback controller. This would allow comparison of designing for robustness in just the controller or just the physical design, but that comparison will be shown in section 4.4.4.

Tables 4.2 shows the structural dimensions of a pre-existing reference design, which were selected prior to the work in this section to optimize weight-bearing capacity while reaching a target joint angle. Dimensions in the robust designs are obtained to minimize variation in dynamic response over individual steps. It should be noted that the parameters found as robust for both closed and open loop are locally optimum as different initial design parameters of the reference design could result in different optimal parameters in Table 4.2. Table 4.3 shows the comparison of the sum of errors in a finite time interval and the relative errors at the finite time.

Optimization results show that the newly designed values tend to give less deviation both over a time interval and at a finite final time, which is further reduced by applying the design technique proposed in this section for a feedback. In this optimization, dimensions of the structure in the closed-loop case show significant changes, while state feedback gain coefficients vary only slightly. This appears to be due to the fact that the uncertainties result from parametric deviation of structural dimensions.

As the robust design method only considers the optimization with respect to parametric uncertainties of structure, the controller will tend to have the same effect on the various plants that have reduced variation between themselves, and less change may be expected in the controller design.

For this test case, designs were constrained by minimal or maximal dimensions that might be fabricated, which are set as bounds in constrained optimization, but weight-bearing capacity was not explicitly included. As some of the optimized parameter are at the dimension constraints, this result shows that true local optimum, at least for purely minimizing dynamic variation, was not present within the design spaces that are likely to be physically possible to build. Figure 4.4 shows the cost level which is reduced over iteration steps, represented in the red-dash line, and the sampled evaluations of original cost function which are represented in solid-color lines.

Table 4.1 Reference Design Dimension of Bulk PZT Actuator Leg Joint

Symbol	Quantity	Reference Design
E_1	Elastic modulus of PZT [32]	100 GPa
E_2	Elastic modulus of Si [69]	170 GPa
d_{31}	Effective piezoelectric stress coefficient [32]	210
V	Applied voltage	30 V
L_1	Length of bonded PZT actuator onto base Si	2125 μm
L_2	Length of un-bonded PZT actuator onto base Si	375 μm
L_3	Length of Si flexure joint	544 μm
L_{act}	Length between two Si flexure joints	10 μm
w	Width of PZT actuator	458 μm
w_{flex}	Width of Si flexure joint	10 μm
t_1	Thickness of PZT actuator	150 μm
t_2	Thickness of base Si	100 μm

Table 4.2 Dimension Parameters of Bulk PZT Actuator Leg Joint

	Reference Design	**Robust Design Closed loop**	**Robust Design Open loop**
Width of PZT stripe	458 μm	1832 μm	115 μm
Width of Si flexure	10 μm	5 μm	5 μm
Length of PZT actuator onto base Si	2125 μm	10000 μm	2338 μm
Length of Si flexure	544 μm	624 μm	598 μm
K_{FB}	$\begin{bmatrix} -6.6491 \\ -0.0048 \\ -0.0001 \\ 0.0001 \end{bmatrix} 10^{10}$	$\begin{bmatrix} -6.6491 \\ -0.0048 \\ -0.0002 \\ 0.0001 \end{bmatrix} 10^{10}$	N.A.

Table 4.3 Sum of Error and Relative Error

	Sum of Error (Angle/Force)	**Relative Error (%)**
Reference Design - OL	48.6	0.249
Robust Design - OL	42.5	0.236
Improvement	12%	5%
Reference Design - CL	0.3688	0.25
Robust Design - CL	0.1929	0.16
Improvement	48%	36%

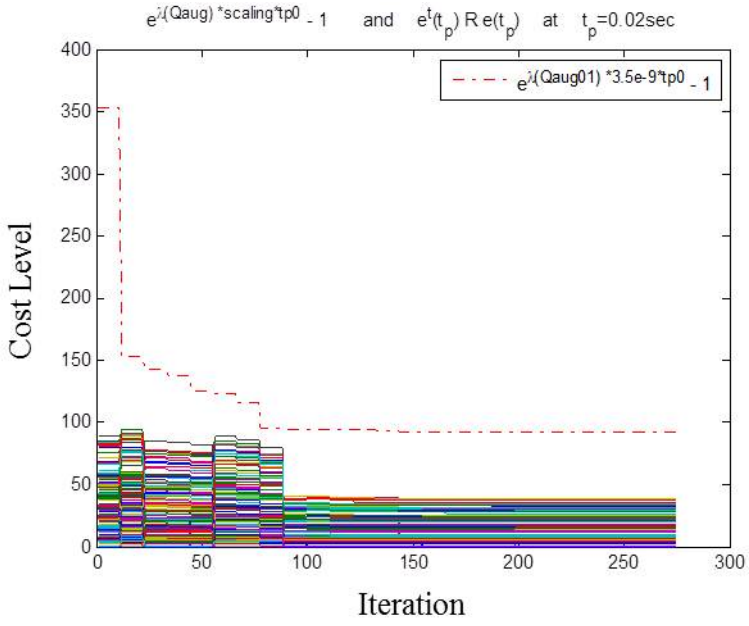

Fig 4.4 Minimization of the structured singular value of Q_a

4.4.4 Comparison to Other Conventional Approach for Open-Loop Scenario

For the parametric design of the structure with the open-loop scenario, the other approach to minimize the maximum perturbation in finite-time transient response is considered in this section. The conventional robust control design technique is H_∞ optimization that minimizes the worst case norm in the frequency response, as shown in Eq. 4.50. As in Eq. 4.43, maximizing the difference between the perturbed plant, G_Δ, and the nominal target plant, G_0, over the maximum uncertainty is performed by the frequency-wise computation, mainly nearby the bandwidth frequency for the transient behavior. Its formulation can be depicted as Linear Fractional Transformation shown in Figure 4.5:

$$\min_{\Theta}\max_{\Delta}\left\|G_\Delta(jw)-G_0(jw)\right\|_\infty=\min_{\Theta}\max_{\Delta}\left\|F_u\left(G_{lft}(jw),\Delta\right)-G_0(jw)\right\|_\infty \tag{4.50}$$

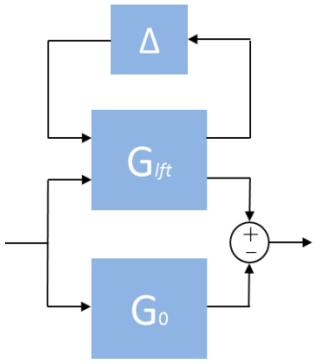

Fig. 4.5 LFT representation of the difference between G_Δ and G_0

Tables 4.4 shows the structural dimensions of a pre-existing reference design, which were selected to optimize weight-bearing capacity while reaching a target joint angle, and the structured dimensions of the robust designs obtained by the structured

singular value based approach and by H_∞ optimization, respectively, where w_{foot} and L_{foot} are the width and length of a foot structure. It is shown that the robust design parameters by H_∞ optimization approach, which is the frequency-wise computation of the sampled difference between G_Δ and G_0,, are locally found near the reference design parameters with minimal changes while the robust design parameters by the structured singular value based approach, which computes the maximum deviation between the nominal and perturbed response, are found at the limit of allowable parameters. Figure 4.6 shows the evaluation of the upper bound of robust finite-time transient response represented in terms of the structured singular value of Q_a matrix, and Figure 4.7 shows the evaluation of H_∞ minimization.

Table 4.4 Parameters for Open-Loop Case: $\mu(Q_a)$ Minimization and H_∞ Minimization

Symbol	Reference design	Robust design $\mu(Q_a)$ approach	Robust design H_∞ approach	Lower bound	Upper bound
w	900 μm	600 μm	899.4 μm	600 μm	1350 μm
w_{flex}	30 μm	30 μm	36.8 μm	30 μm	45 μm
L_1	4000 μm	6000 μm	3946 μm	2667 μm	6000 μm
L_3	400 μm	600 μm	399.9 μm	266 μm	600 μm
L_{act}	75 μm	74.1 μm	74.1 μm	50 μm	112.5 μm
Width of a foot	600 μm	900 μm	599.7 μm	400 μm	900 μm
Length of a foot	740 μm	1110 μm	738.5 μm	493 μm	1110 μm

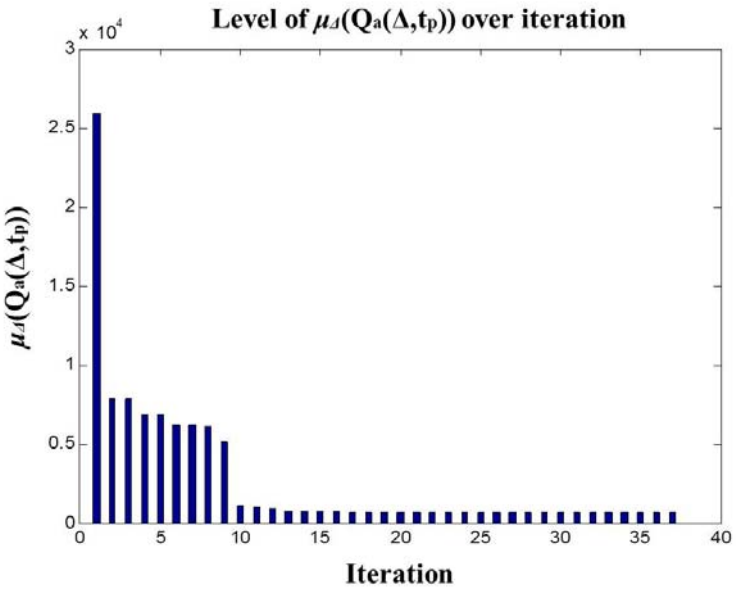

Fig. 4.6 Minimization of the upper bound of robust finite-time transient response represented by structured singular value of Q_a

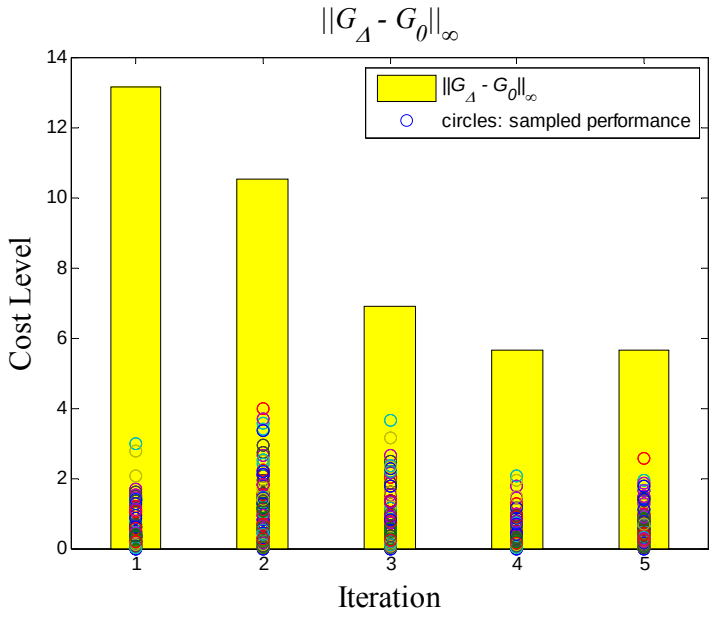

Fig. 4.7 Minimization of the upper bound of robust finite-time transient response by H_∞ norm obtained by the frequency-wise computation

4.4.5 Case Study I Conclusion

In the open- and closed-loop design for robust finite-time transient response of a bulk-PZT actuated micro-robotic leg, the interior-point algorithm of nonlinear optimization is applied to find the local minima of design parameters within the bounds by minimizing the upper bound of the structured singular value in MATLAB. This optimization procedure has not considered the closed loop stability while searching for optimal parameters, and different reference designs or a weighting matrix, R, could result in unstable system over the finite time although this could be solved by constraints on the feedback gain matrix. Nonetheless, the optimization algorithm significantly reduces variation in transient responses in open- and closed-loop scenarios as shown in Section 4.4.3. The design is also somewhat analogous to the design of finite-horizon LQ regulators where closed loop stability may not be conserved.

A conventional robust design method such as H_∞ minimization is also applied. Although pre- and post-weighting filters are often applied for the robust control design and the closed loop system becomes higher order system, the difference between the nominal and perturbed plant nearby the bandwidth of the system is only considered for the structural parametric design. When frequency weighting filters are introduced for such open-loop plant design procedure, the dynamics of those filters should be included in the resulting structural dynamic behavior to meet the performance objective that is minimized, such that the increment in the order of dynamic response and the addition of masses and springs are inevitable in the design of the structure. In this study, the parametric optimization limits those increment and addition for the given reference structures, which is analogous to the fixed order controller design techniques.

4.5 Case Study II: Thin-Film PZT Actuated Micro-Robot Platform Design

4.5.1 Objectives

The second robust design problem motivating transient response optimization is the operation of thin-film PZT actuated micro-robotic leg joints with extremely limited controller complexity, allowing only predefined inputs such as an open-loop step input. The design problem is to find the locally optimal structural dimensional parameters that minimize the performance objective of robust finite-time transient response and maximize the additional performance objective of the in-plane stroke angle. Although larger weight-bearing capacities are required for the development of the eventual thin-film PZT actuated micro-robotic platform, which will be equipped with the control system, sensing, and power circuitry, piezoelectric thin-film actuators that are integrated in silicon joint array have potential to serve as an enabling technology for insect-like bio-inspired robots [24]. For example, piezoelectric thin-film actuators apply exceptionally large forces to silicon structures at low voltage and low power, and the capability of energy harvesting enables to transform drained power consumption to reusable energy [109] on a 1.45cm-by-1.4cm footprint chip of the micro-robotic platform during walking operation.

As introduced in Chapter II, a prototype thin-film PZT-actuated, insect-like bio-inspired micro-robot platform was manufactured by reliable integrating microfabrication of high-aspect ratio silicon structures with thin-film PZT actuators on 10μm-thick silicon-on-insulator wafers. The appendages of thin-film PZT micro-robot, shown in Figure 4.8, consist of two sets of eight-link in-plane actuators arrays in which eight identical PZT-Si actuator structures are connected in series. The inner in-plane actuator array is connected

to the vertical actuator set at the one side, and to the outer in-plane actuator array at the other side. The outer in-plane actuator array, which is remarked in a yellow dashed box in Figure 4.8, is connected to the inner in-plane actuator array. The end bar that is etched from the backside keeps the body of the hexapod distant from the ground.

The robust design procedure will seek target dimensions of thin-film PZT actuator, of silicon flexure joint and tether structure for the open-loop case so that transient motions of the joint are minimally sensitive to perturbed dimensions. Here, a sample fabrication process inducing parametric deviation is the footing exerted by reactive ion etching of high-aspect ratio complex silicon structure. An 8-link in-plane actuators array is also desired to generate large stroke angle while keeping the robust transient behavior, and thus, the maximization of the stroke angle is merged in the design technique. Also the dimension of the thin-film actuation structure in Figure 4.9 is constrained for manufacturability, such as the minimum and maximum allowable dimensions, so that the performance of thin-film PZT lateral actuator could be maintained as in [24].

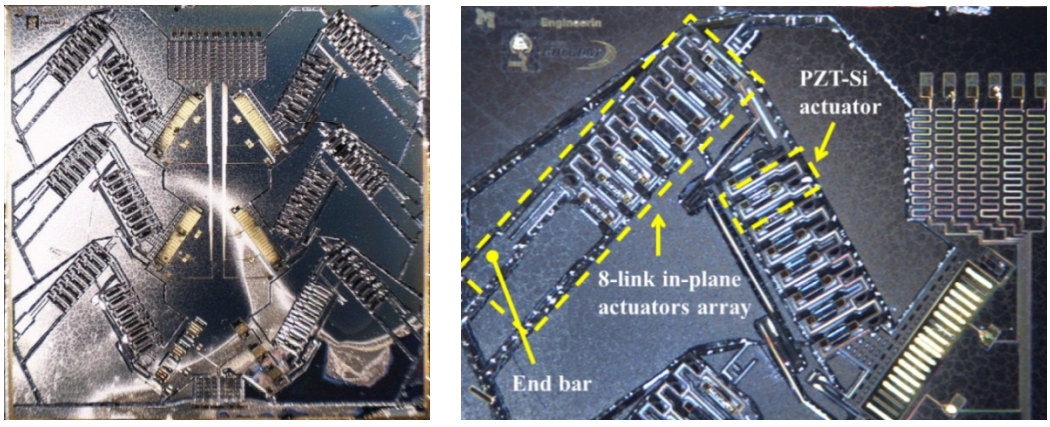

Fig. 4.8 Thin-film PZT actuated hexapod micro-robotic platform with 1.45cm-by-1.4cm footprint (left), and an appendage of two sets of 8-link in-plane actuators array (right)

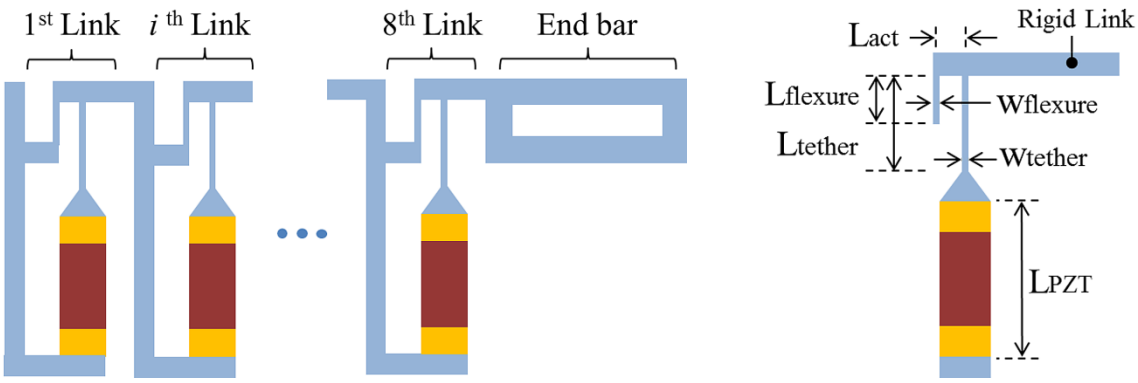

Fig. 4.9 Schematic of a 8-link in-plane actuators array (left) and a thin-film PZT-silicon actuator structure in each link (right)

4.5.2 Modeling of Thin-Film PZT Actuated Micro-Robotic Leg

The structural parameters that determine the transient response of in-plane actuators array in thin-film PZT micro-robotic leg are shown in Figure 4.9: L_{act} which is the length between the flexure and tether structure, L_f and L_t that are the length of flexure and tether structure, w_f and w_t that are the width of flexure and tether structure, and L_{PZT} and w_{PZT} that are the length and width of thin-film PZT actuator.

Table 4.5 Nomenclature of thin-film PZT actuated micro-robotic leg parameters

Symbol	Quantity	Values
E_{Si}	Elastic modulus of Si	150 GPa
$d_{31,eff}$	Effective piezoelectric stress coefficient	230
V_{nom}	Applied voltage	20 V
L_{act}	Length between Si tether and flexure	105 μm
L_{PZT}	Length of thin film PZT actuator	4000 μm
L_t	Length of Si tether	500 μm
L_f	Length of Si flexure	400 μm
w_t	Width of Si tether	900 μm
w_f	Width of Si flexure	30 μm
t_{Si}	Thickness of base Si	100 μm

To obtain the model dynamics of 8-link in-plane actuators array, the stiffness of PZT-silicon actuator structure is considered. The axial stiffness of PZT actuator, K_{PZT}, is obtained from the regime of small displacement-large force of thin-film PZT actuation, and the axial stiffness of silicon tether, K_t, and rotational stiffness of silicon flexure, K_f, are obtained as follow:

$$K_{PZT} = \frac{(EA)_{PZT}}{L_{PZT}} \tag{4.51}$$

$$K_t = \frac{E_{Si} t_{Si} w_t}{L_t} \tag{4.52}$$

$$K_f = \frac{E_{Si} t_{Si} w_f{}^3}{12 L_t} \tag{4.53}$$

The nomenclatures and parametric values are summarized in Table 4.5. The dynamic behavior of 8th link is then obtained as 2nd order system:

$$J_8 \ddot{\theta}_8 = -F_{act,8} L_{act} - K_f (\theta_8 - \theta_7) - b_8 \dot{y}_8 \tag{4.54}$$

$$F_{act,8} = F_{\max} - K_{PZT} \left(L_{act} (\theta_7 - \theta_8) + \frac{F_{act,8}}{K_{tether}} \right) \tag{4.55}$$

where the actuation force applied at 8th link, $F_{act,8}$, is represented as the difference between the blocking force of PZT ceramics, F_{max}, which is defined at zero displacement of PZT ceramics and represents the maximum force that PZT ceramics can generate, and the axial reaction force exerted along the direction of silicon tether. In Eq. 4.55, the axial reaction force consists of the force that requires elongating the silicon tether along the direction of tether and the force that requires rotating the rigid link with respect to the tip of silicon flexure.

By defining α and F_{max} as:

$$\alpha^{-1} = 1 + \frac{K_{PZT}}{K_{tether}} \tag{4.56}$$

$$F_{\max} = Gu_8 \tag{4.57}$$

where G is the input gain of on-off input signal u_8 by either 0 or 1, the dynamics of each link becomes as shown in Eq. 4.58 – 4.60:

$$J\ddot{\theta}_8 = -\alpha L_{act} G u_8 + \left(\alpha K_{PZT,8} {L_{act}}^2 + K_f\right)\theta_7 - \left(\alpha K_{PZT,8} {L_{act}}^2 + K_f\right)\theta_8 - b_8\dot{\theta}_8 \tag{4.58}$$

$$\begin{aligned} J_i\ddot{\theta}_i = {} & \alpha L_{act} G u_{i+1} - \alpha L_{act} G u_i + \left(\alpha K_{PZT,i} {L_{act}}^2 + K_f\right)\theta_{i+1} \\ & - 2\left(\alpha K_{PZT,i} {L_{arm}}^2 + K_f\right)\theta_i + \left(\alpha K_{PZT,i} {L_{act}}^2 + K_f\right)\theta_{i-1} - b_i\dot{\theta}_i \end{aligned} \tag{4.59}$$

$$J_1\ddot{\theta}_1 = \alpha L_{act} G u_2 - \alpha L_{act} G u_1 + \left(\alpha K_{PZT,1} {L_{act}}^2 + K_f\right)\theta_2 - 2\left(\alpha K_{PZT,1} {L_{act}}^2 + K_f\right)\theta_1 - b_1\dot{\theta}_1 \tag{4.60}$$

Then the nominal state and input matrices, A and B, of a leg array in Eq. 4.8 are obtained as follows:

$$A = \underset{i=2,\ldots,7}{block}\left(A_1, A_i, A_8\right) = a_{(m,n)} \tag{4.61}$$

$$B = \underset{i=i,\ldots,7}{block}\left(B_i, B_8\right) = b_{(m,n)} \tag{4.62}$$

$$\begin{aligned} A_1 &= \begin{bmatrix} 0 & a_{(1,2)} & 0 \\ a_{1,21} & a_{1,22} & a_{1,23} \end{bmatrix}, \; A_i = \begin{bmatrix} 0 & 0 & 0 & a_{(2i-1,2i)} & 0 \\ a_{i,21} & 0 & a_{i,23} & a_{i,24} & a_{i,25} \end{bmatrix} \\ A_8 &= \begin{bmatrix} 0 & 0 & 0 & a_{(15,16)} \\ a_{8,21} & 0 & a_{8,23} & a_{8,24} \end{bmatrix} \end{aligned} \tag{4.63}$$

$$B_i = \begin{bmatrix} 0 & 0 \\ b_{(2i,i)} & b_{(2i,i+1)} \end{bmatrix}, \; B_8 = \begin{bmatrix} 0 & 0 \\ 0 & b_{8,22} \end{bmatrix} \tag{4.64}$$

where A_1, A_i, and A_8, are 2-by-3, 2-by-5, and 2-by-4 matrices and B_i and B_8 are 2-by-2 matrices. The components of the matrices in Eq. 4.61 – 4.64 are shown as:

$$
\begin{aligned}
&a_{(1,2)}\,,\ a_{(2i-1,2i)}\,,\ a_{(15,16)} = 1 \\
&a_{1,23}\,,\ a_{i,21}\,,\ a_{i,25}\,,\ a_{8,21} = \frac{\alpha K_{PZT,i} {L_{act}}^2 + K_f}{J_i} \\
&a_{1,21}\,,\ a_{i,23}\,,\ \ a_{8,23} = -\frac{2\left(\alpha K_{PZT,i} {L_{act}}^2 + K_f\right)}{J_i} \\
&a_{1,22}\,,\ a_{i,24}\,,\ a_{8,24} = -\frac{b_i}{J_i}
\end{aligned}
\tag{4.65}
$$

$$
b_{(2i,i)},\ b_{8,22} = -\frac{\alpha L_{act} G}{J_i},\ \ b_{(2i,i+1)} = \frac{\alpha L_{act} G}{J_i} \tag{4.66}
$$

4.5.3 Robust Design Optimization of Thin-Film PZT Actuated Micro-Robotic Leg

The design procedures to be tested seek target dimensions of the thin film PZT actuator and of silicon flexure and tether such that transient motions of the joint are minimally sensitive to dimensional variation or misalignment, based on the framework introduced in section 4.2.1 – 4.2.4. In the design procedure of the micro-robotic leg structure, it is also desirable to increase the magnitude of velocity for maximum stroke displacement over the finite time, t_p, and to keep the positive velocity such that the loss of displacement by the backward motion of the link is avoided. Thus, in addition to the upper bound of robust finite time transient response, the stroke amplitude of the end tip joint angle needs to be taken into account. In the following sections, various performance objectives are defined such that the maximum stroke velocity is achieved while the effect of parametric perturbation on the finite time transient response is minimized.

4.5.3.1 Maximization of Stroke Amplitude

The stroke amplitude of the end tip joint angle, θ_8, is considered for the optimum micro-robotic leg operation, and the objective of design parameter optimization is defined as:

$$\min_{\Theta} J_1 = \min_{\Theta} -\left\{ \frac{\theta_8(t_p)}{t_p} \right\} \tag{4.67}$$

The design parameters are constrained by minimal or maximal dimensions that might be fabricated. The local minimum of the allowable parametric dimension is shown in Table 4.6, and Figure 4.10 shows the perturbed quadratic error samples when the variation of w_t, L_t, w_f, L_f, and the damping coefficients, b_i, is considered. The results show that the minimization of quadratic error over iteration is not preserved while the maximum angular displacement is obtained. To reduce the effect of error performance in the optimization, the modified performance objective includes the upper bound of the original performance objective in Eq. 4.7, as shown in the next sections.

Table 4.6 Local optimal design parameters by minimization of J_1

Design parameter, Θ	Initial value	Optimal value	Lower bound, Upper bound
$\mathbf{L_{arm}}$	12 μm	36 μm	7 μm, 36 μm
$\mathbf{w_{act}}$	100 μm	300 μm	50 μm, 300 μm
$\mathbf{L_{act}}$	500 μm	1000 μm	100 μm, 1000 μm
$\mathbf{w_t}$	4 μm	20 μm	2.5 μm, 20 μm
$\mathbf{L_t}$	290 μm	250 μm	250 μm, 1450 μm
$\mathbf{w_f}$	6 μm	3 μm	3 μm, 30 μm
$\mathbf{L_f}$	128 μm	192 μm	64 μm, 192 μm

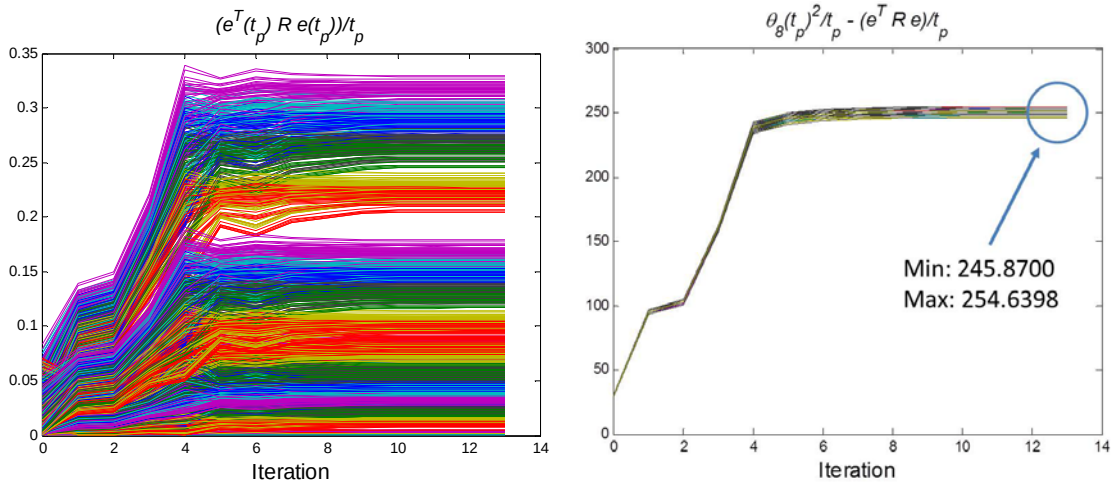

Fig. 4.10 Perturbed quadratic error samples at the finite time by minimization of J_1

4.5.3.2 Maximization of Stroke Amplitude and Minimization of Sampled Quadratic Average Error Performance Index

When the objective function is considered only with the relative errors with respect to the nominal response, local minima tend to be found as the response is decreasing. In the thin-film PZT actuated micro-robotic leg mechanism, it is desired that the angular displacement of leg mechanism subject to error due to model perturbation is maximized. An objective function, therefore, is formulated in terms of maximizing the end tip angle minus the worst case scenario objective of the perturbed finite time response:

$$\min_{\Theta} J_2 = \min_{\Theta} -\left\{ \frac{\theta_8^{\,2}(t_p)}{t_p} - \max_k \frac{e_k{}^T R\, e_k}{t_p} \right\} \tag{4.68}$$

where k is the number of samples of the transient response. Here the weight matrix, R, is chosen such that the deviation of the response of the end tip angle is underlined in the objective function:

$$\max_{\Theta} J_2 = \max_{\Theta} \left(\frac{\theta_8^{\,2}}{t_p} - \max_{k} \left(e^2 + \dot{e}^2 / \omega_n^{\,2} \right) \right) \tag{4.69}$$

where e and $\dot{e}$ are the error and its derivative, and ω_n is the natural frequency of the entire robotic leg.

Table 4.7 Local optimal design parameters by minimization of J_2

Design variable, Θ	Initial value	Optimal value	Lower bound, Upper bound
L_{arm}	12 μm	7 μm	7 μm, 36 μm
w_{act}	100 μm	300 μm	50 μm, 300 μm
L_{act}	500 μm	999 μm	100 μm, 1000 μm
w_t	4 μm	20 μm	2.5 μm, 20 μm
L_t	290 μm	250 μm	250 μm, 1450 μm
w_f	6 μm	3 μm	3 μm, 30 μm
L_f	128 μm	168 μm	64 μm, 192 μm

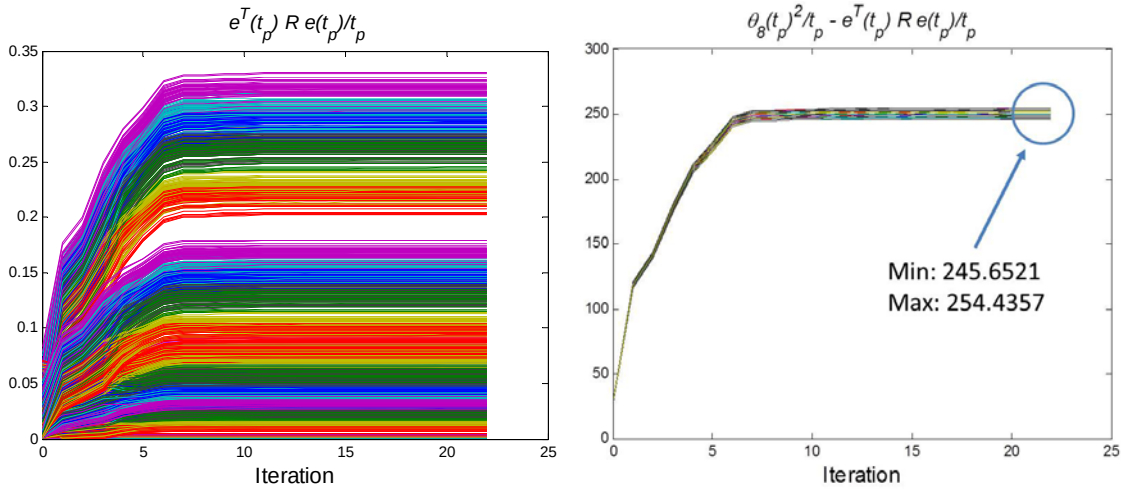

Fig. 4.11 Perturbed quadratic error samples at the finite time by minimization of J_2

4.5.3.3 Maximization of Stroke Amplitude and Minimization of Structured-Singular-Value-Represented Upper Bound

In this case study, the modified performance objective in Eq. 4.69 is optimized so that the worst case stroke amplitude of the end tip joint angle is maximized. This is done using the upper bound of the original performance objective that is obtained from the structured singular values of Q_a matrix. The local minimum of the allowable parametric dimension is shown in Table 4.8, and Figure 4.12 shows the perturbed quadratic error samples when the variation of w_t, L_t, w_f, L_f, and the damping coefficients, b_i, is considered. Similar to the two cases shown in Section 4.5.3.1 – 4.5.3.2, the results also show that the minimization of quadratic error over iteration is not preserved while the maximum angular displacement is obtained.

$$\min_{\Theta} J_3 = \min_{\Theta} -\left\{ \frac{\theta_8^2(t_p)}{t_p} - \max_{\Delta} \frac{\left(1+\rho(Q_a)t_p\right)J_a(0)}{\max_k \left(e_k^T R e_k\right) t_p} \right\} \tag{4.70}$$

Table 4.8 Local optimal design parameters by minimization of J_3

Design variable, Θ	Initial value	Optimal value	Lower bound, Upper bound
$\mathbf{L_{arm}}$	12 μm	7 μm	7 μm, 36 μm
$\mathbf{w_{act}}$	100 μm	50 μm	50 μm, 300 μm
$\mathbf{L_{act}}$	500 μm	1000 μm	100 μm, 1000 μm
$\mathbf{w_t}$	4 μm	2.5 μm	2.5 μm, 20 μm
$\mathbf{L_t}$	290 μm	1450 μm	250 μm, 1450 μm
$\mathbf{w_f}$	6 μm	3 μm	3 μm, 30 μm
$\mathbf{L_f}$	128 μm	192 μm	64 μm, 192 μm

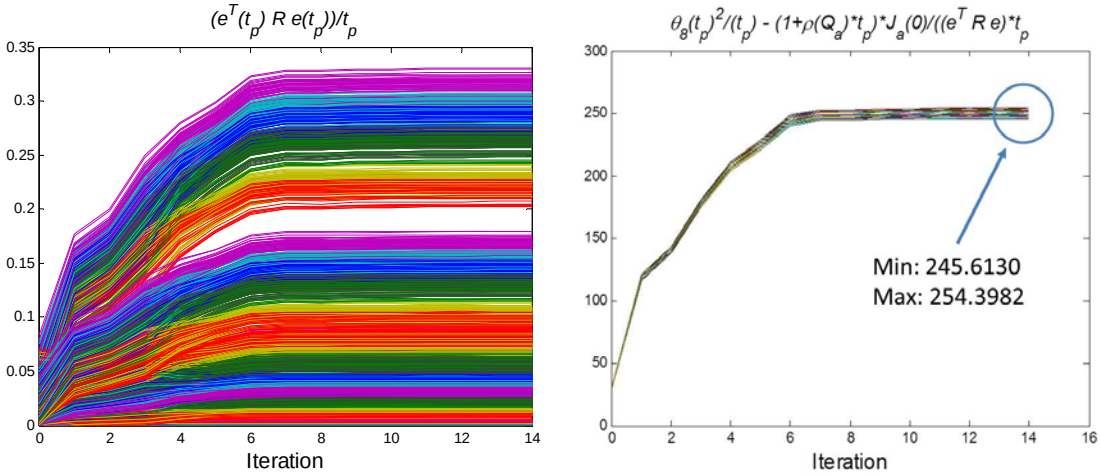

Fig. 4.12 Perturbed quadratic error samples at the finite time by minimization of J_3

4.5.4 Case Study II Conclusion

In the open-loop design for robust finite-time transient response of a thin-film PZT actuated micro-robotic leg array, again the interior-point algorithm of nonlinear optimization is applied to find the local minima of design parameters within feasible bounds by minimizing the upper bound of the structured singular value in MATLAB. The maximization of a nominal performance goal, that of stroke angle, is merged in the design technique by which the maximum perturbation of the finite-time transient response are obtained when the constraint function is chosen to limit the dimensions of thin-film actuation structure. When the maximum stroke length is obtained within the allowable range of the dimension that might be microfabricated, the quadratic error term at the finite time is not minimized. When the performance objective in Eq. 4.7 is considered for the optimization of thin-film PZT actuated micro-robotic leg with the maximum stroke angle, the results show that the structural dimensions tend to be found at the limit of the allowable parametric range, either lower or upper bound of the design

parameters. Although the result obtained by the performance objective defined with the sampled quadratic average error performance index shows that a set of structural parameters satisfying the local minimum could be found, the robustness of finite-time transient response could not be minimized. By introducing a coefficient for weighting between the maximum stroke angle and the maximum deviation of transient response represented in the quadratic error term in the modified performance objective, the existence of the local minimum that maximizes the stroke angle and minimizes the quadratic error term at the finite time might be verified. However, a systematic method of finding the coefficient for weighting the two terms of the stroke angle and the original performance objective has not been studied. Nonetheless, the computation effort when the upper bound of the performance objective of robust finite-time transient behavior is obtained by LFT-represented eigenvalue and computed by μ-analysis is shown to be efficient compared to other randomly selected maximum perturbed response scenario, as shown in Table 4.9.

Table 4.9 Comparison of different objective function in optimization

Approach	Computation Time
J_1	3.7×10^0 (sec)
J_2	1.2×10^4 (sec)
J_3	2.7×10^3 (sec)

4.6 Summary and Conclusion

An upper bound for the maximum perturbed transient response behavior of dynamic systems over a finite duration is obtained in this chapter, and applied to two case

studies from the field of MEMS. As a first example case study, open- and closed-loop design for robust finite-time transient response of a bulk-PZT actuated micro-robotic leg is conducted. The interior-point algorithm of nonlinear optimization is applied to find the local minima of design parameters within the bounds by minimizing the upper bound of the structured singular value in MATLAB. When the feedback controller is implemented, the sum of the error and its relative error are significantly changed when compared to the open-loop case. Also, dimensions of the structure in the closed-loop case show significant changes, while state feedback gain coefficients vary only slightly. This appears to be due to the fact that the uncertainties result from parametric deviation of structural dimensions.

When the performance objective is considered for the optimization of thin-film PZT actuated micro-robotic leg with the maximum stroke angle, the results show that the structural dimensions tend to be found at the limit of the allowable parametric range, either lower or upper bound. Although a weighting coefficient between the maximum stroke angle and the maximum deviation of transient response represented in the quadratic error term could help finding a local minimum that maximizes the stroke angle and minimizes the quadratic error term at the finite time, various weighting factor numbers should be performed in the simulation.

By the case studies, it could be summarized that with proper constraint functions defined to ensure the system performance requirement, one could obtain the locally optimal structural parameters of micro-electromechanical systems by using LFT-represented upper bound of the eigenvalue of Q-matrix such that the robustness of the finite-time transient response behavior is obtained. By μ-analysis, the maximum perturbation is computed effectively when compared to the sampled computation which

may not guarantee the maximum perturbation, although one should balance the robustness of finite-time transient response behavior of the system with other objectives to be met in the design optimization. And the increase in size of the P-matrix and conservativeness of μ-analysis remain as the limitation of the proposed design technique.

CHAPTER V

Conclusion and Future Direction

5.1 Contribution and Summary

Among many challenges for complex piezoelectric micro-electromechanical systems, this dissertation addresses two important tasks:

- Production of complex thin-film piezoelectric microdevices requiring high-yield chip-level process robustness
- Design for robustness against feature-level parametric variation that improves the finite-time dynamic performance reliability of such devices.

The related results of the first task were reported to peer-reviewed journals and conferences:

- The fabrication and characterization of thin-film PZT actuated microdevice produced by the original fabrication was reported, “Large Displacement Vertical Translational Actuator Based on Piezoelectric Thin-Films,” and published at Journal of Micromechanics and Microengineering.
- The previous modeling technique of parallel eight in-plane actuator array for static displacement was reported, “Lateral Thin-film Piezoelectric Actuators For Bio-Inspired Micro-Robotic Locomotion,” and was accepted and presented at

ASME International Design Engineering Technical Conferences in Micro- and Nano-Systems.

- The new device fabrication and characterization produced by the proven, revised fabrication was submitted, "Multi-Degree-of-Freedom Thin-Film PZT Actuated Micro-robotic Leg," at Journal of Microelectromechanical System, and currently under revision.
- The results of device fabrication and characterization for bulk piezoelectric microdevice, which is shown in Appendix A, was reported, "Amplifying Transmission and Compact Suspension for a Low-Profile, Large-Displacement Piezoelectric Actuator," at Journal of Micromechanics and Microengineering.

In addition, the related results of the second task were also reported to peer-reviewed conferences:

- The design techniques of solely plant design case were performed by three methods; the first method is based on simple damping ratio and natural frequency calculations, while the second and third methods are based on state-space and transfer function models, respectively. All three approaches reduce error in transient dynamics compared to nominal designs based solely on static weight-bearing or fabrication considerations, with the state-based being identified as usable to a wide range of systems. This result was reported, "Robust Design of A Micro-electromechanical System in the Presence of Assembly Uncertainty," and was accepted and presented at ASME Dynamic Systems and Control Conference.
- The design technique considering the closed loop system with a state feedback gain was also reported, "Robust Finite-Time Transient Response of Micro-

electromechanical System," and was accepted and presented at American Control Conference.

In this dissertation, to achieve the first task, it is demonstrated that various piezo-MEMS applications can be integrated using a proven microfabrication process flow with conserved piezoelectric performance and high yield rate. The process was also able to achieve multi-layer complex micro-mechanical structures despite complex PZT processing. Using the chemical inertness of a silicon dioxide vertical barrier layer against XeF_2 gas, silicon structures in the proposed applications were successfully protected and released with higher yield rate than devices manufactured by earlier photoresist encapsulation fabrication processes for integrating thin-film PZT and single crystal silicon structures. The performance of the piezoelectric devices was tested by measuring the curvature of the test piezo-cantilevers, and was determined experimentally to be preserved. For a variety of different device designs, such as multi-degree-of-freedom micro-robotic legs and various vertical translational z-axis focusing stages, it is concluded that various piezo-MEMS devices can be integrated in the process flow.

With regards to the process application, two prototype piezo-MEMS devices are characterized experimentally. The first prototype device is a combination of micro-robotic leg joint arrays capable of producing multiple-degree of freedom motion, in which thin-film PZT lateral and vertical actuators are integrated with complex 3D silicon structures using the silicon oxide vertical barrier trenches that are deposited prior to PZT deposition. Consistent undercut length of thin-film PZT actuators array was obtained. The designed motion generated by the proposed multi-DoF microrobotic leg is larger than that of the final leg structure due to remaining silicon oxide layers. Nonetheless,

relatively large joint angles are achieved: the final vertical actuators produce 37^0 rotational displacements at 15V DC, resulting in 148μm deflection of the hip joint; an inner lateral actuator array produces 0.1^0 in-plane and 18^0 vertical rotation with respect to the hip joint, due to imperfections in the fabrication process impeding in-plane motion and accentuating out-of-plane motion; the outer lateral actuator array produces 3.9^0 in-plane rotation, more consistent with actuator array models. The improvement to this current design and fabrication of thin-film PZT devices is intended to support future microrobotic chassis development. Micro-robotic joint modeling included compensation for intrinsic residual stress of thin-film stacks that changes the initial deflection of the actuator arrays, the behavior of in-plane flexure joint array structures when the width of oxide trench barrier is taken into consideration, and the design of an electrical interconnect structure connected with the outer compact actuator array with less impact on the final device motion.

The second prototype device is vertical translational z-axis focusing stages, capable of producing large displacement with faster response time, in which thin-film PZT vertical actuators are integrated with complex multi-layer silicon structures encapsulated by silicon oxide vertical barrier trenches that are deposited prior to PZT deposition. Consistent undercut length of multi-fold thin-film PZT vertical actuators was again obtained with minimal effect on the piezoelectric performance of the actuators. The motion generated by the proposed vertical translational z-axis focusing stage is larger than 200μm, and the transient response of two-fold stage showed that faster transient response behavior can be obtained, compared to other actuation types for into-tissue scanning of endoscopic micro-mirror platforms, with 3.8 ms peak time and 55.2 ms

settling time.

To address the second task, it is demonstrated that the maximum perturbed finite-time transient behavior of piezoelectric micro-electro-mechanical systems can be effectively reduced through a representation as a spectral radius of a compact matrix form, which allows the efficient computation of the worst-case scenario of perturbed finite-time transient response. It is also demonstrated that design for feature-level parametric robustness improves the finite-time dynamic performance reliability of piezoelectric microdevices.

For case studies, thin-film PZT actuated microdevice and bulk-PZT actuated microdevices are considered for feature-level parametric robustness and in the design case study, such that variation in transient dynamic variation due to the remaining variability of fabrication processes, which cannot be completely dealt with the chip-level process elaboration, could be accessed by the feature-level optimization.

The open- and closed-loop design for robust finite-time transient response of a bulk-PZT actuated micro-robotic leg is first conducted. The interior-point algorithm of nonlinear optimization is applied to find the local minima of design parameters within the bounds by minimizing the upper bound of the structured singular value in MATLAB. Since the optimization procedure has not considered the closed loop stability while searching for optimal parameters, different reference designs or a weighting matrix, R, could result in unstable system over the finite time. Nonetheless, the optimization algorithm significantly reduces variation in transient responses in open- and closed-loop scenarios.

The open-loop design for the optimization of thin-film PZT actuated micro-robotic leg with the maximum stroke angle is secondly conducted. The simulation results show that the structural dimensions tend to be found at the limit of the allowable parametric range, either lower or upper bound. Although a weighting coefficient between the maximum stroke angle and the maximum deviation of transient response represented in the quadratic error term could help finding a local minimum that maximizes a combination of the stroke angle and a penalty for the quadratic error term at the finite time, various weighting factor numbers should be performed in the simulation.

By both case studies, with proper constraint functions defined to ensure the system performance requirement, one could obtain locally optimal structural parameters of micro-electromechanical systems by using LFT-represented upper bound of the eigenvalue of Q-matrix such that the robustness of the finite-time transient response behavior is obtained. By μ-analysis, the maximum perturbation is computed effectively when compared to sample computation results, which in contrast may not guarantee the maximum perturbation.

5.2 Future Directions

Possible future works relating to the research tasks performed in this dissertation may include:

- Characterization of the piezoelectric sensing performance compared to the performance measured from the original fabrication process
- Integration of thin-film smart material-based actuation structure into the proposed microfabrication process flow

- Parametric design of a state estimator as all states of a micro-electromechanical system are not available to measure
- Co-optimization of the plant and other types of robust feedback controller design by μ-synthesis

Other features that could be integrated into the microfabrication process presented include piezoelectric sensing structures for feedback control application. Since the first task in this dissertation only focuses on the actuation capability of thin-film PZT layer, characterization of the sensing performance should be performed and compared to the performance measured from the original fabrication process.

In addition to piezoelectric actuation for micro-electromechanical system, other smart material-based actuation mechanisms can be applied in MEMS applications. For example, in [67], sputter-coated TiNi thin films are reported in MEMS devices. Since the thickness of TiNi films enough for the shape memory effect and to carry other complex microstructures connected to the actuator is required, a microfabrication process integrating silicon dioxide barrier trenches with thin-film TiNi layer could be performed to obtain the benefits presented in this dissertation, although the adhesion of TiNi film on SiO2 layer is reported to be unreliable. Additional layer depositions, such as silicon nitride, on top of silicon dioxide layer could be conducted.

From the second area of research, only a state feedback controller has been considered in spite of the assumption of the measurability of all system states. Based on the separation principle between the design of the state feedback gain and of the state estimator gain, one could pursue a compact matrix-represented upper bound of robust

finite-duration transient behavior of a dynamic system with a state estimator, which can be useful to the actual physical system integration. Furthermore, discrete time systems should also be studied.

When the plant model is fixed while the parameters are optimized, co-optimization of the plant and other types of advanced robust feedback controller design can be considered as another direction in the research of robust finite-time transient response. Moreover, it is needed to understand the optimization algorithm to know when accounting for robustness will change the parametric design results.

APPENDICES

Appendix A

Section 1: Microfabrication of Amplifying Mechanism of Two-Photon Endoscopic Imaging Micro-Piezoelectric Actuator

In contrast to the thin-film process where the micofabrication of thin-films are integrated in the entire micromachining process, bulk PZT actuators use piezoelectric ceramics that are shaped separately from the micromachining process, which defines amplifying mechanisms only. A design of an amplification and suspension mechanism with a bulk-piezoelectrically-deriven microactuator is proposed in [38] to achieve very large stroke lengths within the size constraints suitable for certain endoscopic microscopy application and weight bearing capacity of a 20-mg micro lens. Thus the proposed mechanism is designed for a low spring constant in actuation direction and a high spring constant in vertical and transverse direction. High-aspect ratio elastic structure is then needed not only to satisfy the requirement of displacement but also to avoid stress-induced bending along the vertical direction. In [38], the amplification and suspension mechanism is designed in such a way that the lateral displacement of the PZT ceramic is transformed by leverage mechanism into a large transverse displacement of the two lever-tips, which is re-transformed by chevron bridge-structure into a lateral displacement of the lens holder. Details in design analysis and optimization results can be found in [38].

Figure A.1 shows the microfabrication process flow for the amplifying mechanism silicon structures of the two-photon endoscopic imaging micro-device. In step A), a pre-furnace cleaned silicon-on-insulator (SOI) wafer is coated with low pressure chemical vapor deposited (LPCVD) silicon dioxide with the thickness of 1.2μm, which is used as a hard mask during deep reactive ion-etching (DRIE) process. Due to the selective etching of silicon dioxide in hydrofluoric acid (HF), the oxide is first etched away then chromium and gold are deposited by lift-off process to provide electrical conduction to the underside of the PZT ceramic in step B) – E). A single-layer photoresist mask is patterned to define the geometry of the amplification structure that consists of lever-arm and chevron bridge-structure, and of the platform that consists of micro lens holder with double spring system, as shown in step F).

The LPCVD silicon dioxide layer is etched during a reactive ion-etching (RIE) process, followed by a DRIE process of the top device silicon layer in step G). However, the variation of etching rate and thus selectivity of photoresist to silicon, and erosion of photoresist are expected in 100μm- and 500μm-deep DRIE process of the top and handle layers of SOI wafer, respectively. The aforementioned problems can be avoided by the hard mask provided in step A). Before the backside etching process, amplification and platform structures in the top silicon layer of SOI wafer should be protected since high-aspect ratio lever-arm, chevron bridge-structure, and double spring structures can be damaged during dicing step between step H) – I), and detachment process of SOI wafer from the carrier between step J) – K). Polymer materials, such as SPR-220 photoresist or conformal-deposited parylene without adhesion promoter, can be used to hold and protect the structures shown in step H). After dicing of the samples with pre-defined size, a STS

carrier mounting procedure is performed using a silicon carrier wafer: 3μm SPR-220 is spin-coated on a carrier wafer and polymer-protected side of SOI wafer is faced on the top of unbaked 3μm SPR-220, positioned, and baked at 90^0C for 2 minutes. The backside is then patterned and etched by 500μm depth in step I) – J). The SOI sample is detached from the carrier in step K), and 49%-HF is used to etch the SiO_2 by a timed etch, followed by critical point drying (CPD). In the final step M), the oxygen plasma can be used to remove photoresist and oxygen RIE can be used to remove parylene.

The drawbacks of using photoresist (PR) protection in step H) are that some air voids can be trapped inside the trench during spin-coating and that relatively thick PR layer has higher heat capacity than of thin layer PR. A relatively thin PR layer can result in poor step coverage for 100μm-deep trenches and failure of PR protection for chevron bridge-structure and double spring structure. Although some of trapped air voids can be removed by long-hour oven baking at 90^0C, relatively thick PR layer can result in poor heat transfer to the chilled chuck during 500μm-deep DRIE process, which also consequences the irregular etching of silicon layer from the side of a wafer and the burning of photoresist mask in step J). Figure A.2 shows the backside hole image of PZT-silicon connector and movable lens holder. Figure A.3 shows the fully released amplifying transmission mechanism.

In contrast, parylene is well known for conformal deposition by physical vapor deposition (PVD) and low thermal mass (heat capacity). It can be used as a good protection material to avoid the trapped air voids by conformal deposition and for better heat transfer than thick PR layer. Although both photoresist and parylene layers can be chemical mechanical polished (CMP) to improve heat transfer during DRIE process, the

CMP process may be eliminated from the fabrication process flow if parylene protection can solely avoid the drawbacks of photoresist protection, such as irregular etching from the side of a SOI wafer and photoresist mask burning during the backside etching.

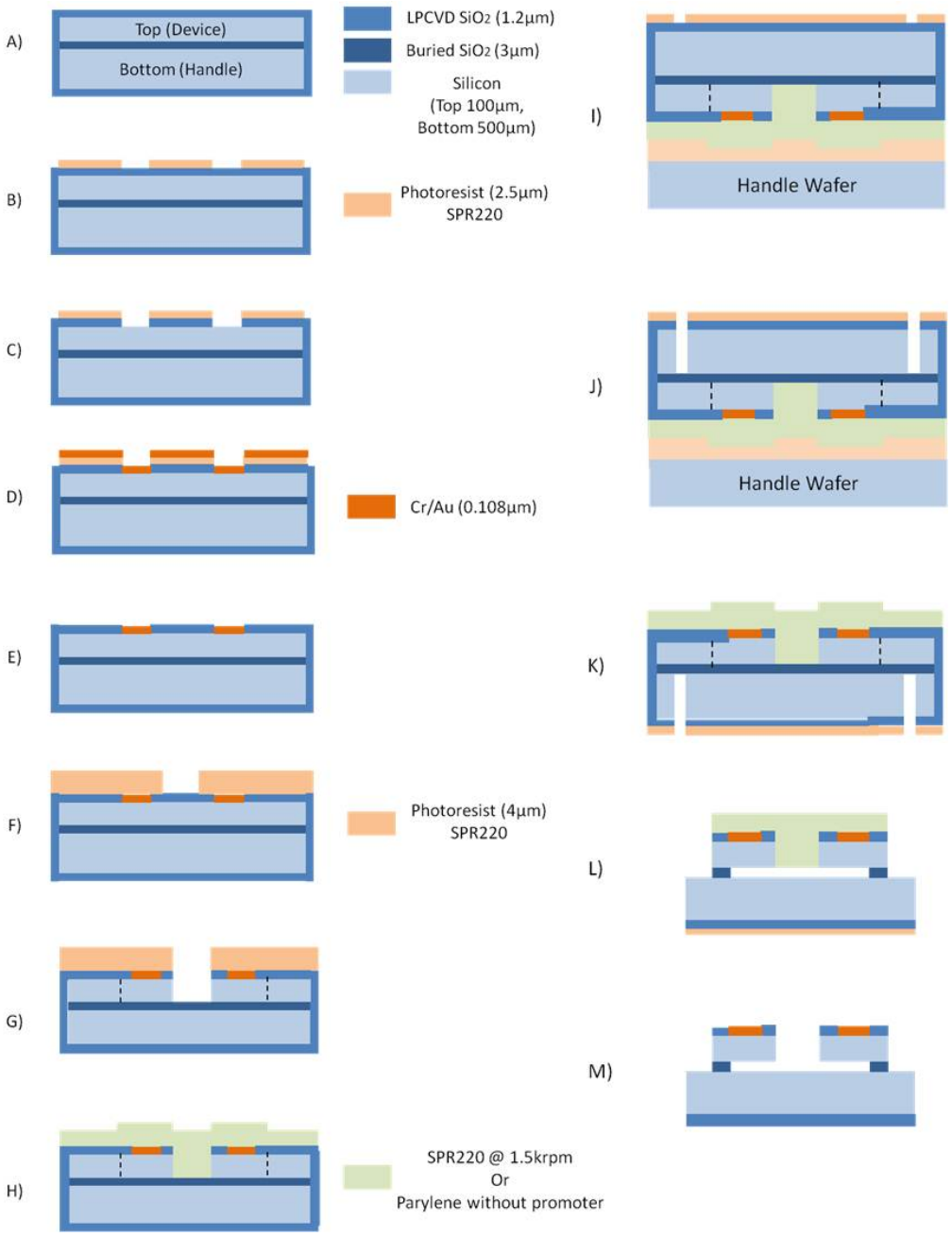

Fig. A.1 Microfabrication process flow of bulk PZT actuated silicon transmission amplification structure

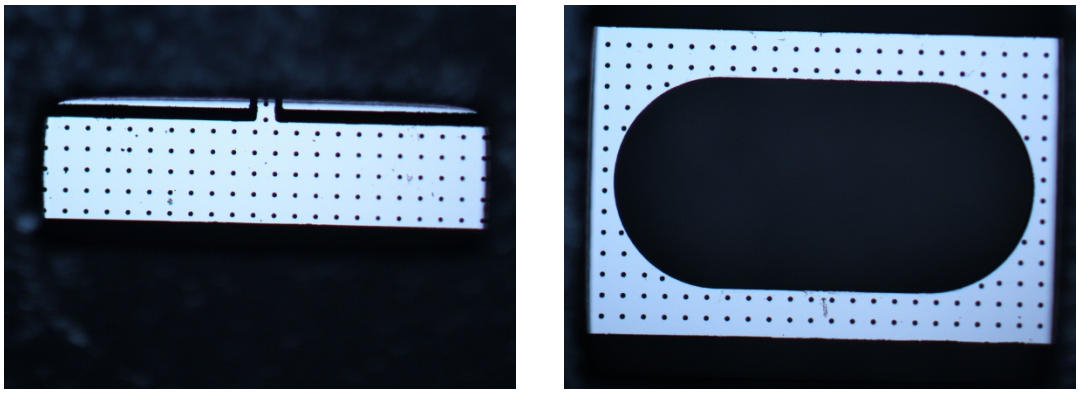

Fig. A.2 Backside image of PZT-Si connector (left) and lens holder moving stage (right)

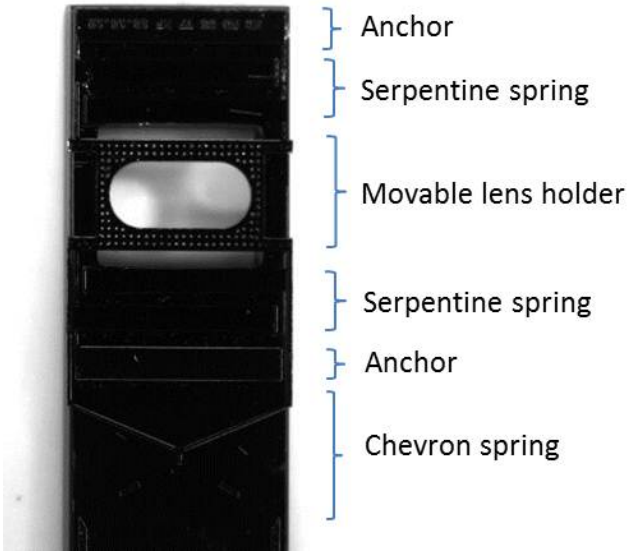

Fig. A.3 Top view of bulk PZT actuated amplifying transmission silicon structure

Section 2: Etching Technique of Thin-Film PZT Layers

In this section, the experimental results of 1μm-thick PZT layer etching by both wet-chemical and dry etching techniques are presented. By dry etching technique, it is known that the gases containing chlorine and fluorine are very effective in making the volatile compounds from PZT layer [10]. However, forming volatile species from PZT layer at room temperature is difficult, and increment in substrate temperature and in ion bombardment energy is required [10] [11]. By wet-chemical etching, it is known that etching solution with different compositions is a conventional and effective way due to its high etching rate and low cost [115] although the property of the PZT film might be degraded during wet etching due to hydrogen diffusion, and undercut is unavoidable.

Section 2.1 and 2.2 present the experimental results of wet and dry etching techniques, which are found from the literature, at UM LNF. Figure A.4 shows the layers of test samples used for PZT wet-chemical and dry etching experiments.

Fig. A.4 Layers of test samples for PZT etching experiment

Section 2.1: Experimental Result of PZT Wet Etching

From [115] to [116], two-step etching process of 10:1 BHF followed by $2HCl:1H_2O$ at 45^oC was performed with PZT samples using presented chemicals at UM LNF. Because the metal-fluoride residues remain on the surface of PZT layer when 10:1 buffered HF solution is used, HCl dip was performed to remove the residues from BHF

etching step. From [115] [116], the etching rate of PZT film is 1000A/min and the selectivity of PZT film to photoresist is 1:2. The experiment was performed under the wet etching operational conditions as shown in Table A.1, and Figure A.5 to A.7 show the results of wet-chemical etching of three PZT monitor samples from 20-second etching to 60-second etching. As the solution etches the opened area of 1-μm PZT layer for 60 seconds, the gap between serpentine structures of the first (Figure A.5) and third samples (Figure A.7) is vanished as the photoresist mask layer is attacked by HF concentration. Figure A.8 shows the scanning electron microscopic images of the first and third samples where the sidewall of etched PZT layer is irregular due to the effect of BHF on photoresist mask. Although the addition of NH_4Cl helps weaken the effect of BHF on photoresist and reduce the undercut, and design rules to compensate the undercut length to obtain the target dimension of patterned PZT structure, the experiment of dry etching technique is also performed in the next section.

Table A.1 PZT wet etching operational condition

Parameters	**Numeric Values**
10:1 buffered HF	20 – 60 seconds
DI rinse	3 minutes
2HCl:1H_2O	30 seconds
DI rinse	3 minutes

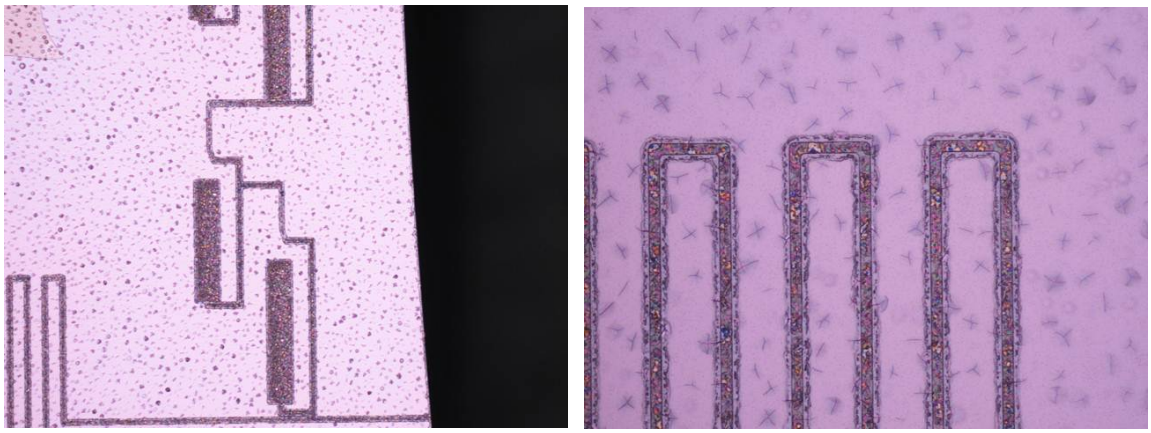

Fig. A.5 Wet-chemical etching in 10:1 BHF, 20 seconds

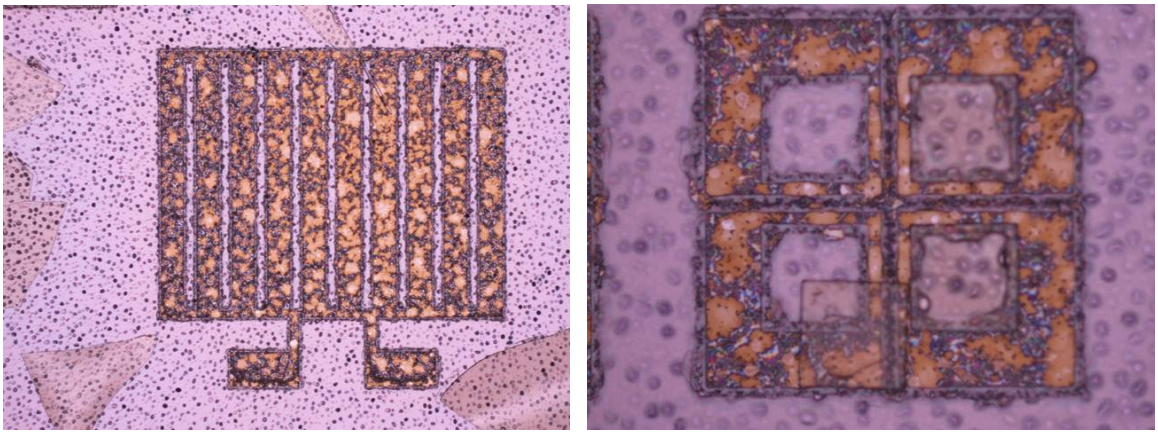

Fig. A.6 Wet-chemical etching in 10:1 BHF, 40 seconds

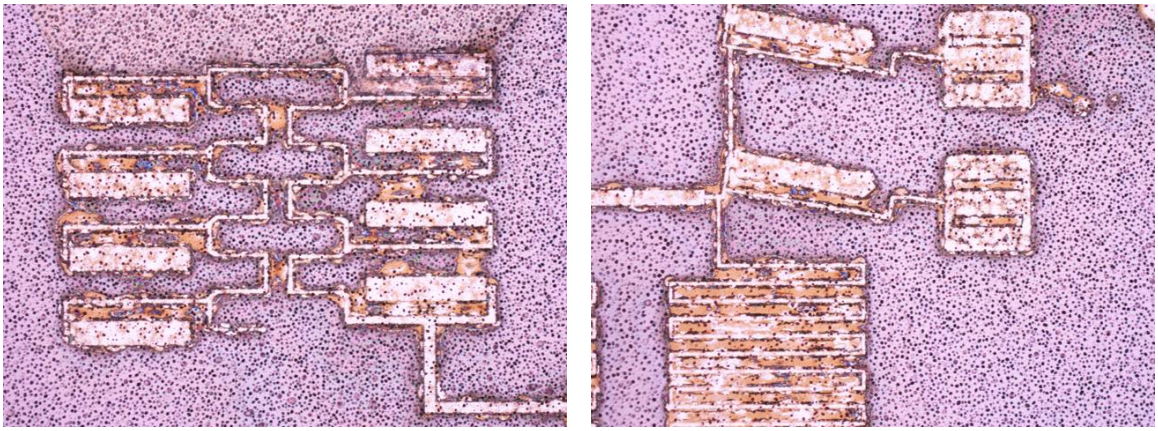

Fig. A.7 Wet-chemical etching in 10:1 BHF, 60 seconds

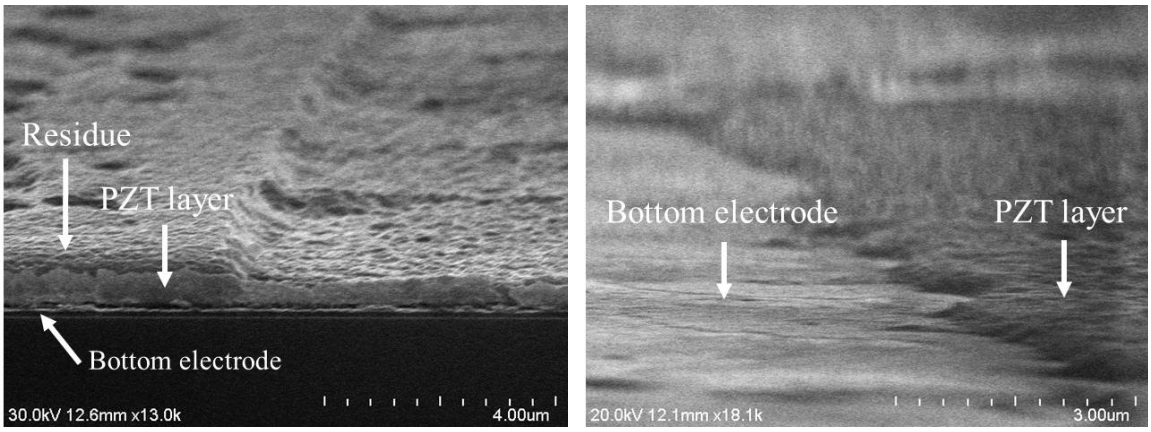

Fig. A.8 Wet-chemical etching in 10:1 BHF: 20 seconds (left), 60 seconds (right)

Section 2.2: Experimental Results of PZT Dry Etching

The various techniques of dry etching process of thin film PZT have been reported in literature [117], [118], [119], and [120]. In the experiment, the operation parameters of STS Glass Etcher are tuned as shown in Table A.2. The result is obtained that the selectivity of PZT to AZ9260 is measured to be 1:4, and the etch rate is measured as 1000 – 1600 angstrom per minutes by the profilometer. The sidewall angle was also measured to be approximately 108 degree shown in Figure A.9.

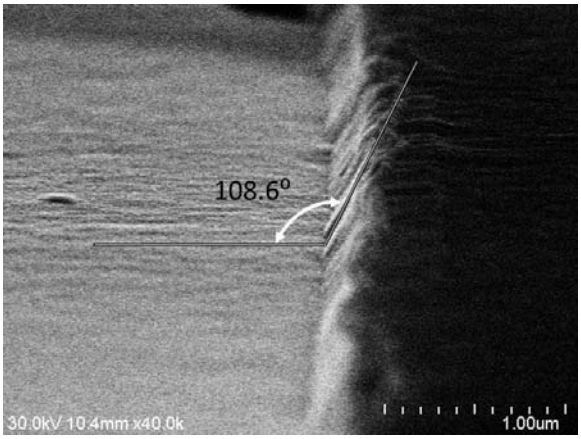

Fig. A.9 Sidewall angle of etched PZT layer

Table A.2 STS Glass Etcher operation parameters

Parameters	Numeric Values
High Frequency Coil Generator 13.56MHz	1220 W
High Frequency Platen Generator 13.56MHz	320 W
Flow rate of Ar	64 sccm
Flow rate of SF_6	25 sccm

Appendix B

Section 1: Derivation of Bulk PZT Actuated Micro-Robotic Leg

From Eq. 4.46,

$$k_\theta^{-1} = f\left(L_1, L_3, L_{act}, w, w_{flex}\right) = \frac{C}{c} + \left[\left(\frac{1}{c}\right)D - \left(\frac{H}{c^2}\right)d\right] \tag{4.46}$$

where the parameters c and C are nominal parameter terms, d and D are the perturbed parameter terms, H is defined in Eq. B2 and E_1 and E_2 are elastic modulus of PZT and Si materials:

$$\begin{aligned}
&C = \beta_1 w L_1 \ , \ \ \beta_1 = 6L_3 L_{act} d_{31} E_1 \\
&c = \beta_2 t_1 w + \beta_3 t_2 w + E_1 w_{flex}{}^3 t_2 L_1 \ , \ \beta_2 = 3L_3 L_{act}{}^2 E_1 \ , \ \beta_3 = 3L_3 L_{act}{}^2 E_2 R \\
&D = \left(\pm\beta_1 w L_1\right)\delta w - \left(\beta_1 w\right)\Delta L \\
&d = \left(\pm\beta_2 t_1 w\right)\delta t_1 + \left(\pm\beta_3 t_2 w \pm E_1 w_{flex}{}^3 t_2 L_1\right)\delta t_2 + \varepsilon\,\delta w - \left(E_1 w_{flex}{}^3 t_2\right)\Delta L \\
&\varepsilon = \pm\beta_2 t_1 w \pm \beta_3 t_2 w + 3E_1 w_{flex}{}^3 L_1 t_2
\end{aligned} \tag{B1}$$

The vertical spring stiffness, k_{tot}, is calculated from the individual spring stiffness and its deviation:

$$k_{tot} = f\left(k_{a0}, k_{b0}, k_{c0}, \Delta k_a, \Delta k_b, \Delta k_c\right) = \frac{H+S}{h+s} \tag{4.49}$$

where H, S, h and s are defined as:

$$\begin{aligned}
H &= \left(k_{a0} + k_{b0}\right)\left(k_{c0} + k_{b0}\right) \\
S &= \left(k_{a0} + k_{b0}\right)\left(\Delta k_c + \Delta k_b\right) + \left(k_{c0} + k_{b0}\right)\left(\Delta k_a + \Delta k_b\right) \\
&= \left(k_{c0} + k_{b0}\right)\Delta k_a + \left(k_{a0} + k_{c0} + 2k_{b0}\right)\Delta k_b + \left(k_{a0} + k_{b0}\right)\Delta k_c \\
h &= k_{a0} + k_{c0} + 2k_{b0} \\
s &= \Delta k_a + \Delta k_c + 2\Delta k_b
\end{aligned} \tag{B2}$$

$$\begin{aligned}
&k_{a0} = \left(k_{NoAct+Si}\right)_0 = \frac{E_2 w t_2{}^3}{4(L_1 + L_2)} \quad , \quad k_{b0} = \left(k_{flex}\right)_0 = \frac{E_2 w_{flex} t_2{}^3}{4L_3{}^3} \\
&k_{c0} = \left(k_{Act+Si}\right)_0 = \frac{\frac{E_1}{2}\left(w t_1{}^3 + 3t_1 t_2{}^2\right) + \frac{E_2}{2}\left(w t_2{}^3 + 3t_2 t_1{}^2\right)}{3L_1{}^2 L_2 + 2L_1{}^3}
\end{aligned} \tag{B3}$$

$$\Delta k_a = \Delta k_{NoAct+Si} = \left(\pm \frac{3E_2 t_2^{\,3}}{4(L_1 + L_2)} \right) \delta t_2 + \left(\pm \frac{E_2 w t_2^{\,3}}{4(L_1 + L_2)} \right) \delta w$$

$$\Delta k_b = \Delta k_{flex} = \left(\pm \frac{3E_2 t_2^{\,3}}{4L_3^{\,3}} \right) \delta t_2 + \left(\pm \frac{E_2 w_{flex} t_2^{\,3}}{4L_3^{\,3}} \right) \delta w$$

$$\Delta k_c = \Delta k_{Act+Si} = \left(\frac{6}{3L_1^{\,2}L_2 + 2L_1^{\,3}} \right) \left[\sum_{j=1}^{2} \left(\alpha_{E1tj} + \alpha_{E2tj} \right) \delta t_j + \left(\alpha_{E1w} + \alpha_{E2w} \right) \delta w \right] \qquad \text{(B4)}$$

$$- \left(\frac{\frac{E_1}{2}\left(w t_1^{\,3} + 3 t_1 t_2^{\,2} \right) + \frac{E_2}{2}\left(w t_2^{\,3} + 3 t_2 t_1^{\,2} \right)}{\left(3L_1^{\,2}L_2 + 2L_1^{\,3} \right)^2} \right) \left(3L_1^{\,2} - 6L_1 L_2 - 6L_1^{\,2} \right) \Delta L$$

where

$$\begin{aligned}
\alpha_{E1t1} &= \pm 3 w t_1^{\,3} \pm 3 w t_1 t_2^{\,3} \\
\alpha_{E2t1} &= \pm 3 w t_2^{\,3} \pm 3 w t_2 t_1^{\,3} \\
\alpha_{E1t2} &= 2 w t_1 t_2^{\,2} \\
\alpha_{E2t2} &= 2 w t_2 t_1^{\,2} \\
\alpha_{E1w} &= \pm w t_1^{\,3} \pm w t_1 t_2^{\,2} \\
\alpha_{E2w} &= \pm w t_2^{\,3} \pm w t_2 t_1^{\,2}
\end{aligned} \qquad \text{(B5)}$$

Appendix C

Section 1: Introduction

As a second sample application of complex thin-film PZT processing, a z-axis focusing stage, or z-stage for endoscopic microscopy instruments is described and characterized. The target system performance, implications for the process flow, and experimental test results of a completed z-stage are presented.

MEMS-based instruments for endoscopy that integrate light sources, optical fibers, and miniaturized scanners are being developed to provide images of tissues at various wavelengths to enable real-time, *in vivo* diagnosis of cancer during endoscopy [89], such as in the system shown in Figure C.1. These instruments may provide higher resolution, greater depth-of-view into tissue, and/or greater field-of-view scanning capabilities than conventional optical endoscope imaging techniques. To date, commercial MEMS-based optical instruments have been equipped with planar mirror scanning technology, which is relatively well developed. However, the ability to change the focal depth when substantial depth-of-penetration into tissue is possible is a new direction for microactuator research. Several previous researchers have demonstrated endoscopic imaging instruments using various miniature and MEMS actuation mechanisms. As examples of meso-scaled actuator-driven endoscopic instruments, [95] and [96] show the potential and limits of commercially available linear direct-current motors and piezoelectric squiggle motors, respectively. These actuation mechanisms have the dimensional limitation when the miniaturized endoscopic instrument is desirable, particularly in their length, which limits endoscopic maneuverability. In [97], Volder et al. demonstrated that a cylinder-piston type of fluidic actuation mechanism

produces up to 1200mm/s speed with 11mm displacement. Although 1-Newton actuation force could be exerted, the fluid-assisted actuation mechanism reported in [97] presents only +/- 30μm positioning accuracy. For MEMS-based endoscopic instruments, Sandner et al. used electrostatic out-of-plane actuation structure [98], Chen et al. [99] and Wu et al. [100] used thermally actuated actuator to drive high force motion with large displacement, but the former example system exerts 600μm large displacement but only at resonance and with a footprint too large for endoscopic use, and the latter faces challenges to heat dissipation and from slow thermal time constants when used for real-time scanning *in vivo*.

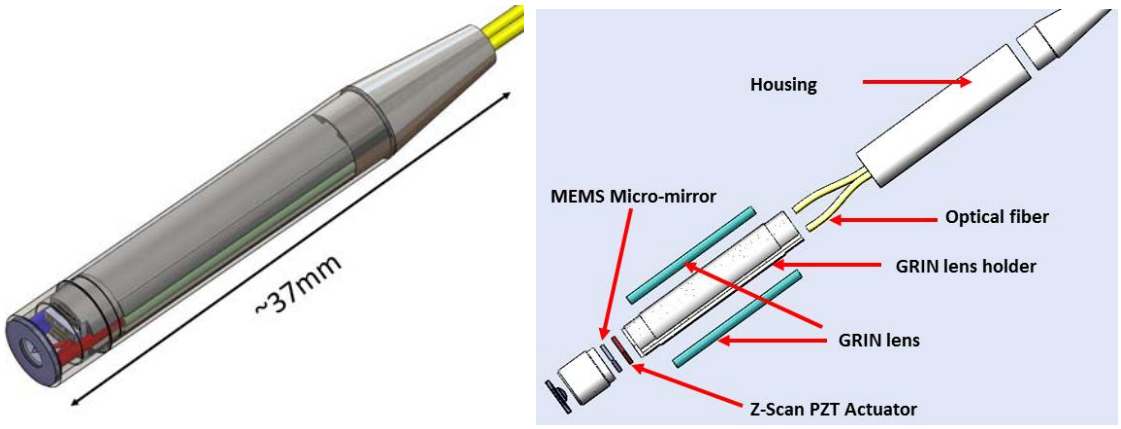

Fig. C.1 Hand-held MEMS-based instrument (left) that integrates MEMS micro-mirror driven by comb-drive actuator, vertical translational z-axis focusing stage driven by thin-film PZT actuator, GRIN lens and optical fiber for light source transmission (Courtesy Z. Qiu)

For high-speed and large displacement with high positioning resolution, multi-fold vertical piezoelectric actuators have potential advantages. Although, as mentioned in Chapter III, previously used techniques for integrating thin-film PZT unimorph benders with high-aspect ratio structures has limited the complexity of potential micro-actuator structure, piezoelectric actuation remains a desirable candidate technology due to its large

force capacity, modest voltage requirements, and ability to increase the z-axis translational displacement and the bandwidth compared to the electrostatically and thermally actuated optical micro-devices at comparable voltage or power levels.

Figure C.2 shows the proposed vertical translational z-axis focusing stage, actuated by two-fold vertical thin-film PZT actuators connected to each corner of the central mirror stage platform. Actuators with four folds at each corner are also discussed, later in this chapter.

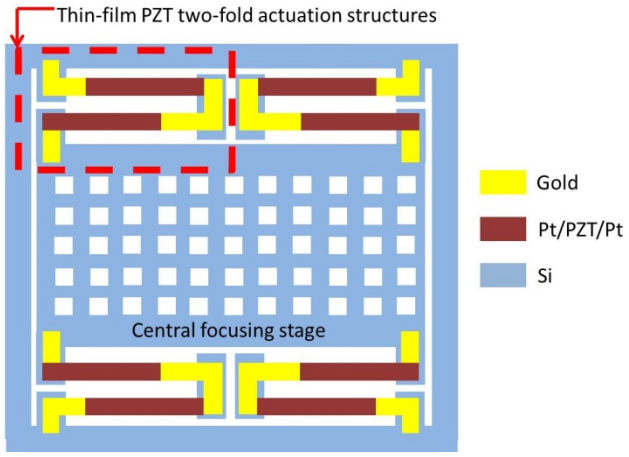

Fig. C.2 Schematic of vertical translational z-axis focusing stage: two-fold thin-film PZT vertical actuators at each corner of the central stage platform

From the microfabrication procedure in Chapter II, which increases yield of PZT actuator arrays, improves uniformity of the individual actuators and associated rigid silicon structures with a simple release process, and enables multi-layer silicon structures with backside and frontside etching, prototype vertical translational z-axis focusing stages were produced. Experimental characterization of these actuators is conducted in this appendix. The resulting mechanisms are designed to act as the structural foundation for miniature axial scanning (z-axis) of a dual-axes confocal microscope. They have

achieved translational deflections exceeding 200 μm and unloaded stages have a demonstrated bandwidth of near 200 Hz.

As shown in Chapter II, low pressure chemical vapor deposition (LPCVD) of silicon oxide vertical barrier trenches prior to thin film PZT deposition enables the integration of thin-film PZT deposition with silicon structures over large chip or wafer areas, serving as a robust encapsulation of silicon structures and a base layer of PZT thin film. An additional benefit of LPCVD oxide deposition on SOI wafers is to provide a hard-mask layer on the backside of the wafer, allowing multi-layer silicon structures through backside silicon etching handle layer of silicon-on-insulator wafers. Consistent undercut length of thin-film PZT actuators array, as realized by these processes, is also essential for producing the proposed vertical translational focusing stages having multi-fold vertical actuators at each corner of central mirror stage platforms.

For the vertical image scanning operation as well as three-dimensional imaging operation, the translational z-axis focusing stage is operated not only in the resonant motion but also in the quasi-static motion. For empirical characterization of microfabricated z-axis focusing stages, experimental testing of initial position, static displacement, resonant behavior, and transient response are conducted in the following sections.

Section 2: Experimental Characterization

Section 2.1: Static Displacement of Z-Axis Focusing Stage

For static displacement characterization, the initial position of the focusing stage connected to thin-film PZT multi-folding vertical actuators at each corner is first measured to obtain the perturbed vertical position of each multi-fold vertical actuators

located at each corner of the mirror platform at 0V. The variation in vertical positions of each actuator is caused by different residual stress of the layers due to local heating effect and different thermal expansion coefficient of the deposited materials during the fabrication process. Figure C.3 show two-fold and four-fold thin-film PZT vertical actuators for the initial flatness test of the central focusing stage. The initial positions of the central stage in the reference coordinates, (x_0, y_0, z_0), are obtained with respect to the outer silicon frame on which the gold bonding pads are located. An x_1-y_1 plane perpendicular to the vertical z-axis of the central stage is obtained by measuring three corners of the central stage that the gold layer is deposited, as shown in Figure C.3. Then, the initial points in (x_0, y_0, z_0) are obtained with respect to the coordinate of the central stage, (x_1, y_1, z_1), in terms of the homogenous coordinate transformation matrices:

$$R_x = \begin{bmatrix} 1 & 0 & 0 \\ 0 & \cos(\psi) & -\sin(\psi) \\ 0 & \sin(\psi) & \cos(\psi) \end{bmatrix}, \quad R_y = \begin{bmatrix} \cos(\phi) & 0 & \sin(\phi) \\ 0 & 1 & 0 \\ -\sin(\phi) & 0 & \cos(\phi) \end{bmatrix} \tag{C1}$$

The homogenous transformation matrix, H, is represented as a composition of rotations about current axes of each transformed coordinates, (x_{Rx}, y_{Rx}, z_{Rx}) and (x_{Ry}, y_{Ry}, z_{Ry}), where (x_{Rx}, y_{Rx}, z_{Rx}) and (x_{Ry}, y_{Ry}, z_{Ry}) are the coordinates obtained by the rotation transformation, R_x and R_y, respectively:

$$\begin{bmatrix} x_0 \\ y_0 \\ z_0 \end{bmatrix} = H \begin{bmatrix} x_1 \\ y_1 \\ z_1 \end{bmatrix}, \quad \text{where } H = R_y \cdot R_x \tag{C2}$$

Table C1. Initial vertical position of the central stage of 2-folding leg z-scanner

	Vertical Position (μm)
z_1 of Pt. 1	135.95
z_1 of Pt. 2	73.349
z_1 of Pt. 3	6.7366
z_1 of Pt. 4	-36.006

Table C2. Initial vertical position of the central stage of 4-folding leg z-scanner

	Vertical Position (μm)
z_1 of Pt. 1	67.839
z_1 of Pt. 2	53.407
z_1 of Pt. 3	-88.972
z_1 of Pt. 4	-110.27

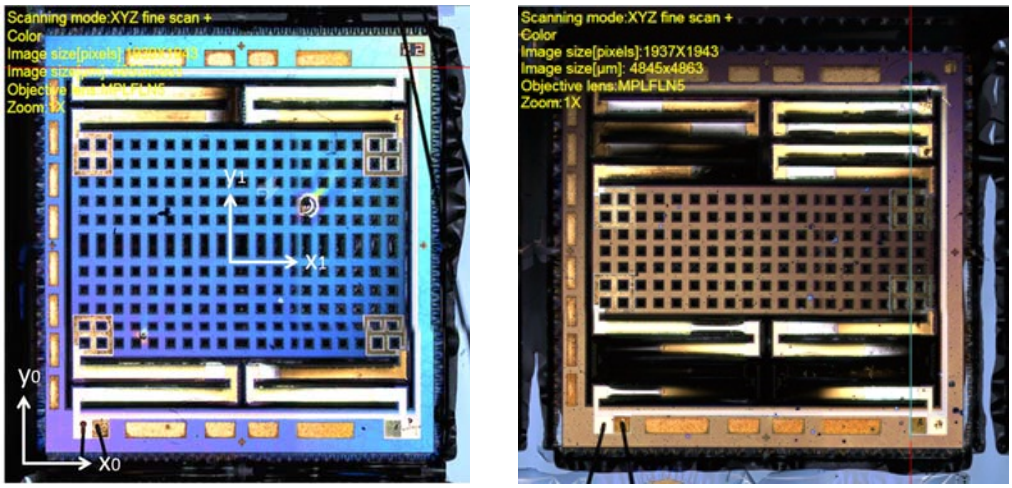

Fig. C.3 Two-folding (left) and four-folding (right) thin-film PZT vertical actuators connected to the central focusing stage: Initial flatness test of the central focusing stage

Thus, the initial positions of two-fold and four-fold z-axis focusing stages are obtained from Eq. C1 and C2, and are shown in Table C1 and C2. In addition to the initial flatness of the focusing stage, the static displacement at different driving voltage input is also obtained. Figure C4 shows the vertical motion of four-fold vertical actuators at 0V and 18V measured by the displacement sensor. For measurement of pure actuator

motion, a laser displacement sensor is aimed at the interconnect between the central mirror stage platform and the end of each multi-fold vertical thin-film PZT actuator.

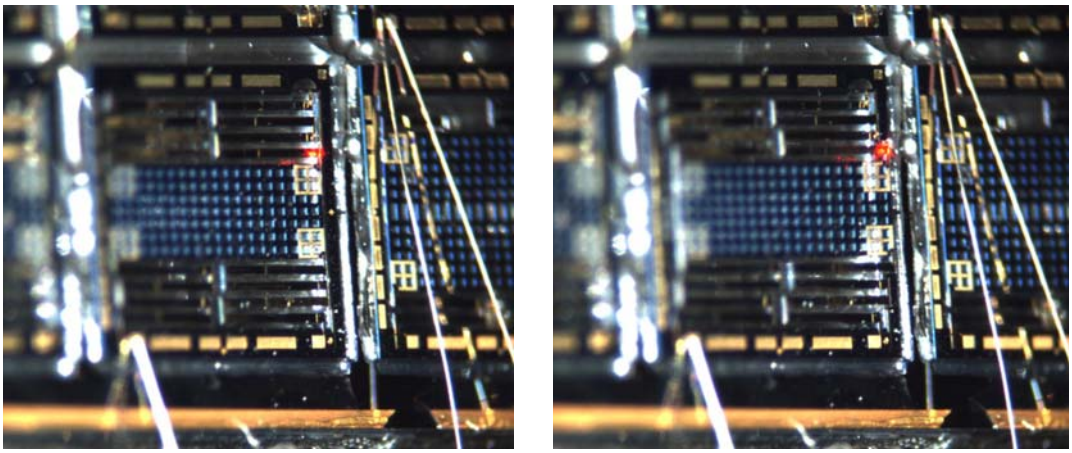

Fig. C4 Vertical motion generated by four-folding z-axis focusing stage at 0V (left) and 18V (right)

Section 2.2: Dynamic Behavior of Z-Axis Focusing Stage

The characterization of the dynamic behavior of produced z-axis scanning stage devices is performed in this section, using the experimental setup shown in Figure C5. The frequency sweep with driving voltage input of 2Vpp $\sin(f \cdot t) + 3V_{offset}$ is performed, and the vertical displacement of a multi-fold vertical actuator at the corner of the central mirror platform is obtained in Figure C6, where f is the driving frequency. The first resonance of the two-fold z-axis focusing stage was measured near 150Hz. In transient operation, Figure C7 shows the step response under 18V input voltage, demonstrating 3.8 ms peak time and 55.2 ms settling time; sampling time of the data is set to 20μsec per sample.

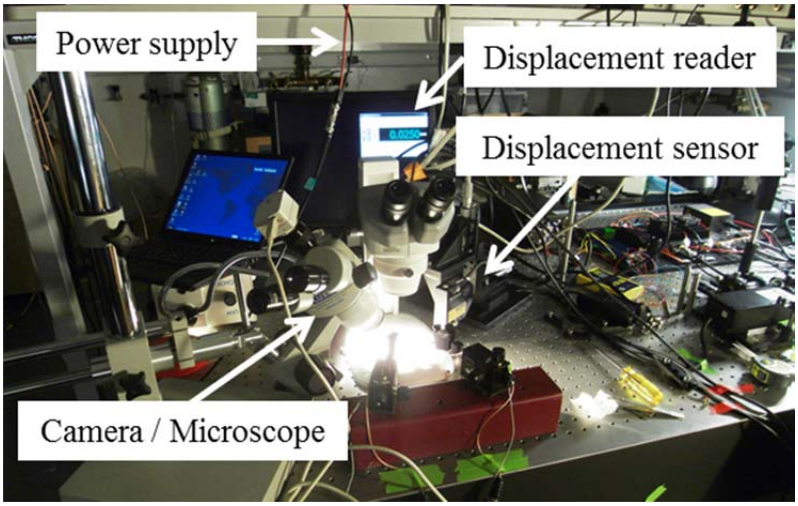

Fig. C5 Experiment station for displacement measurement

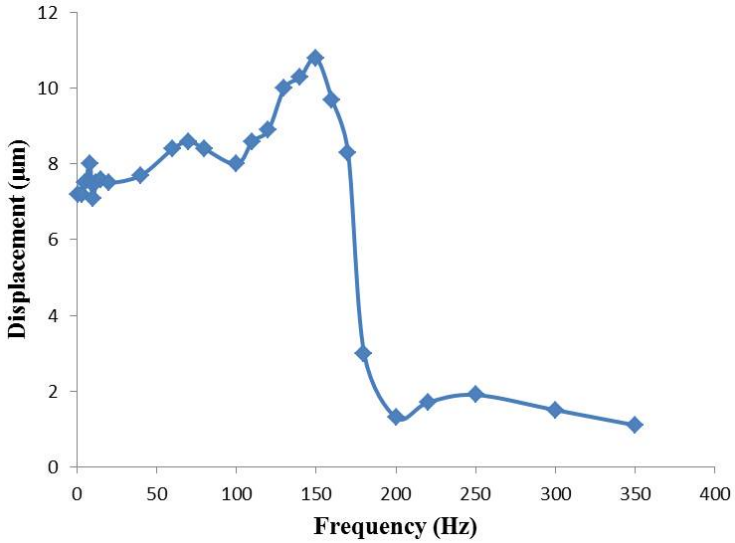

Fig. C6 Frequency response of two-fold z-axis focusing stage when the vertical actuators are activated with driving sinusoidal input

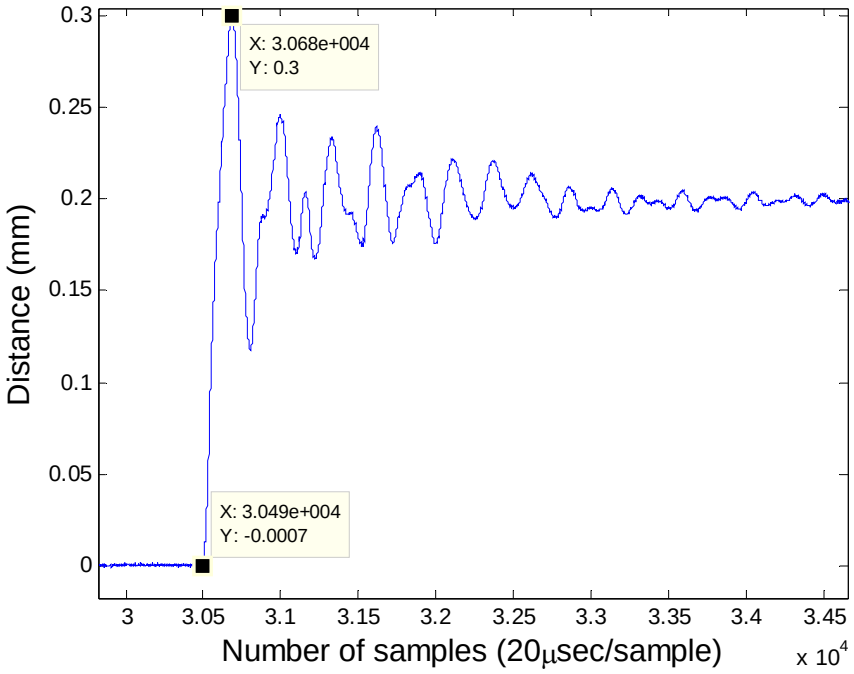

Fig. C7 Transient reponse of two-fold z-axis focusing stage when the vertical actuatosrare activated

Section 3: Summary and Conclusion

Prototype thin-film PZT-actuated vertical translational z-axis focusing stages capable of producing large displacement with faster response time were fabricated and are characterized in this section. As shown in Table C3, the thin-film PZT actuated mirror platform produces a faster response compared to other out-of-plane MEMS stages of different actuation types that are reported in literature or commercially available. Although characterization of a four-fold stage platform is underway, the displacement of two-fold stage plaform shows the good pregress towards desired depth-of-view (DOV) range. For a prototype device, range hase been measured to be 0.25 mm, compared to the ultimate target DOV range into tissue is 0.5 mm. Thin-film PZT vertical actuators are

integrated with complex multi-layer silicon structures encapsulated by silicon oxide vertical barrier trenches, as described in Chapter II. Consistent undercut length of multi-fold thin-film PZT vertical actuators was obtained with minimal effect on the piezoelectric performance of the actuators. The motion generated by the proposed vertical translational z-axis focusing stage is more than 200μm, and the transient response of a two-fold stage shows that fast transient response can be obtained, with 3.8 ms peak time, compared to other actuator types for into-tissue scanning of an endoscopic micro-mirror platform.

Table C3 Comparison of out-of-plane MEMS stage with different actuation for an endoscopic application

	Range	**Speed**	**Volume**	**Voltage**
Pneumatic	12 mm	1000 mm/s	1.3 mm in diameter 15mm in length	?
Electrostatic	1 mm	?	5 mm in diameter	50V
Thermal	0.62 mm	25 mm/s	0.8mm by 0.8mm	5.3V (184mW)
Linear DC	N.A.	N.A.	2 mm in diameter 5.5 mm in length	1V
Squiggle	6 mm	10 mm/s	1.8 by 1.8 by 6 mm	4.5V
Thin-film PZT (two-fold)	0.25 mm	66 mm/s	2 by 2 by 0.5mm	18V (60μW)

REFERENCES

[1] T. Hasenkamp, M. Arvidsson, and I. Gremyr, "A Review Of Practices For Robust Design Methodology," *Journal of Engineering Design*, vol. 20, no. 6, pp. 645-57, 2009.

[2] M. Arvidsson and I. Gremyr, "Principles of Robust Design Methodolog," *Quality and Reliability Engineering International*, vol. 24, no. 1, pp. 23-35, 2008.

[3] P. Andersson, "On Robust Design in the Conceptual Design Phase: A Qualitative Approach," *Journal of Engineering Design*, vol. 8, no. 1, pp. 75-89, 1997.

[4] L. Schenato, W.-C. Wu, L. E. Ghaoui, and K. Pister, "Process Variation Analysis for MEMS Design," *Proc. of SPIE Int. Society for Optical Engineering*, vol. 4236, pp. 272-279, 2001.

[5] M. Shavezipur, K. Ponnambalam, A. Khajepour, and S.M. Hashemi, "Fabrication uncertainties and yield optimization in MEMS tunable capacitors," *Sensors and Actuators, A: Physical*, vol. 147, no. 2, pp. 613-622, 2008.

[6] R. Liu, B. Paden, and K. Turner, "MEMS Resonators That Are Robust To Process-Induced Feature Width Variations," *Journal of Microelectromechanical Systems*, vol. 11, no. 5, pp. 505-11, 2002.

[7] S. Heo, G. H. Yoon, and Y. Y. Kim, "The robust design for micro electro-thermal actuators," *Proc. of SPIE Int. Society for Optical Engineering*, vol. 5389, no. 1, pp. 241-7, 2004.

[8] X. Xiong, Y.-L. Wu, and W.-B. Jone, "Yield analysis for self-repairable MEMS devices," *Analog Integrated Circuit and Signal Processing*, vol. 56, no. 1-2, pp. 71-81, 2008.

[9] J.E. Juber, N.A. Fleck, and M.F. Ashby, "The selection of mechanical actuators based on performance indices," *Proc. of the Royal Society of London A: Mathematical and Physical Sciences*, pp. 2185-2205, 1965.

[10] J. Baborowski, "Microfabrication of Piezoelectric MEMS," *Journal of Electroceramics*, vol. 12, no. 1-2, pp. 33-51, 2004.

[11] S. Trolier-Mckinstry and P. Muralt, "Thin Film Pizoelectrics for MEMS," *Journal of Electroceramics*, 2004.

[12] N. Conway, Z. Traina, and S.-G. Kim, "A strain amplifying piezoelectric MEMS actuator," *Journal of Micromechanics and Microengineering*, vol. 17, no. 4, pp. 781 – 787, 2007.

[13] R.A. Dorey and R.W. Whatmore, "Electroceramic Thick Film Fabrication for MEMS," *Journal of Electroceramics*, vol. 12, no. 1-2, pp. 19-32, 2004.

[14] Z. Wang, J. Miao, C. W. Tan, and T. Xu, "Fabrication of piezoelectric MEMS devices-From thin film to bulk PZT wafer," *Journal of Electroceramics*, vol. 24, no. 1, pp. 25-32, 2010.

[15] J. Karttunen, J. Kiihamaki, S. Franssil, "Loading effects in deep silicon etching," *Proc of SPIE Int. Society for Optical Engineering*, vol. 4174, pp. 90-97, 2000.

[16] K.T. Turner and S.M. Spearing, "Modeling of direct wafer bonding: effect of wafer bow and etch patterns," *Journal of Applied Physics*, vol. 92, no. 12, pp. 7658-66, 2002.

[17] M. C. Lee, S. J. Kang, K. D. Jung, S.-H. Choa, and Y. C. Cho, "A high yield rate MEMS gyroscope with a packaged SiOG process," *Journal of Micromechanics and Microengineering*, vol. 15, no. 11, pp. 2003-10, 2005.

[18] K. Zhang, W. Jiang, and X. Li, "Wafer-level sandwiched packaging for high-yield fabrication of high-performance MEMS inertial sensors," *IEEE Int. Conf. on Micro Electro Mechanical Systems*, pp. 814-17, 2007.

[19] J. Yamaguchi, T. Sakata, N. Shimoyama, H. Ishii, F. Shimokawa, and T. Yamamoto, "High-yield Fabrication Methods for MEMS Tilt Mirror Array for Optical Switches," *NTT Technical Review*, vol. 5, no. 10, 2007.

[20] S.Y. Xiao, L.F. Che, X.X. Li, and Y.L. Wang, "A novel fabrication process of MEMS devices on polyimide flexible substrates," *Microelectronic Engineering*, vol. 85, no. 2, pp. 452-457, 2008.

[21] S.Chen, H.T. Chien, J.Y.Lin, and Y.W. Hsu, "A method of fabricating MEMS Accelerometers," *Int. Conf. on Electronic Materials and Packaging*, pp. 84-87, 2008.

[22] C. O'Neal, A. Malshe, S. Singh, and W.D. Brown, "Challenges in the Packaging of MEMS," *International Symposium on Advanced Packaging Materials*, pp. 41-47, 1999.

[23] E. Peeters, "Challenges in Commercializing MEMS," *IEEE Computational Science and Engineering*, vol. 4, no. 1, pp. 44-8, 1997.

[24] K. Oldham, J. Pulskamp, R. Polcawich, and M. Dubey, "Thin Film PZT Lateral Actuators With Extended Stroke," *Journal of Microelectromechanical Systems*, vol. 17, no. 4, pp. 890-9, 2008.

[25] Y.-C. Tung and K. Kurabayashi, "A Single-Layer PDMS-on-Silicon Hybrid Microactuator with Multi-Axis Out-of-Plane Motion Capabilities – Part II: Fabrication and Characterization," *Journal of Microelectromechanical Systems*, vol. 14, no. 3, pp. 558 – 566, 2005.

[26] T. Bel´endez, C. Neipp, and A. Bel´endez, "Large and small deflections of a cantilever beam," *European Journal of Physics*, vol. 23, pp. 371 – 379, 2002.

[27] Y. Xia and G. M. Whitesides, "Soft Lithography," *Annu. Rev. Mater. Sci.*, 1998.

[28] A. De Luca and B. Siciliano, "Closed-Form Dynamic Model of Planar Multilink Lightweight Robots," *IEEE Transactions on Systems, Man, and Cybernetics*, vol. 21, no.4, pp. 826-39, 1991.

[29] F. Xi and R. G. Fenton, "Determination of Nominal Joint Displacements of a Flexible Link Manipulator By Inverse Kinematics Analysis," *Mech. Mac& Theory*, vol. 29, no. 3, pp. 393 – 405, 1994.

[30] Marcello H. Ang Jr., Wang Wei, Low Teck-Seng, "On the Estimation of the Large Deflection of a Cantilever Beam," *Proc. of Int. Conf. on Industrial Electronics, Control, and Instrumentation*, vol. 3, pp. 1604-1609, 1993.

[31] H. Seto and T. Namerikawa, "Robust Performance and Transient Response of the H_∞/μ DIA Control for Magnetic Suspension Systems," *Proc. of IEEE International Conference on Control Applications*, vol. 2, pp. 1020-5, 2004.

[32] APC International Ltd., from http://www.americanpiezo.com/piezo_theory/index.html

[33] K. Oldham, Ph.D. thesis, "Microdevices for Vibration Suppression in Computer Hard Disk Drives", University of California, Berkeley, 2006.

[34] K. Oldham, "Power Optimization in Autonomous Microsystems via Integrated Motion Control", CAREER Project description

[35] T. Shibano, K. Nakamura, T. Takenaga, and K. Ono, "Platinum etching in Ar/Cl_2 plasmas with a photoresist mask," *Vac. Sci. Technology*, A17, 1999.

[36] NSF Engineering Research Center for Wireless Integrated MicroSystems, "Fantastic Voyage: Microsystem Development at the University of Michigan, 1975 - 2000"

[37] NSF Engineering Research Center for Wireless Integrated MicroSystems, “Fantastic Voyage 2: Microsystem Development at the University of Michigan, 2000 - 2010”

[38] J. Domke, “Design and Optimization of a Large Stroke Z-Stage for Two Photon Endoscopic Imaging”, Master’s Thesis, University of Freiburg, Germany, 2010.

[39] Z. Fan, J. Wang, and E. Goodman, “An Evolutionary Approach for robust layout synthesis of MEMS”. *Proc. of IEEE/ASME Int. Conf. on Advanced Intelligent Mechatronics*, vol. 2, pp. 1186–1191, 2005.

[40] D. Horsley, N. Wongkomet, R. Horowitz, and A. Pisano, “Precision Positioning Using a Microfabricated Electrostatic Actuator,” *IEEE Transactions on Magnetics*, vol. 35, no. 2, pp. 993-9, 1999.

[41] T. Imamura, M. Katayama, Y. Ikegawa, T. Ohwe, R. Koishi, and T. Koshikawa, “MEMS-Based Integrated Head/Actuator/Slider for Hard Disk Drives”, *Transactions on Mechatronics*, vol. 3, no. 3, pp. 166-74, 1998.

[42] H. Fathy, J. Reyer, P. Papalambros, and A. Ulsoy, “On the Coupling between the Plant and Controller Optimization Problems,” *American Control Conference*, vol. 3, pp. 1864-1869, 2001.

[43] D. Hernandes, S. Park, R. Horowitz, and A. Packard, “Dual-Stage Track-Following Servo Design for Hard Disk Drives,” *American Control Conference*, vol.6, pp. 4116-21, 1999.

[44] J. Nie, R. Conway, and R. Horowitz, "Optimal H Infinity Control for Linear Periodically Time-varying Systems in Hard Disk Drives," *ASME Dynamic Systems and Control Conference*, vol. 1, pp. 993-1000, 2010.

[45] R. Conway and R. Horowitz, “A mu-synthesis approaches to guaranteed cost control in track-following servos,” *Proc. of the 17th Int. Federation of Automatic Control*, vol. 17, no. 1, 2008.

[46] R. K. Messenger, T. W. McLain, and L. L. Howell, “Piezoresistive Feedback for Improving Transient Response of MEMS Thermal Actuators,” *Proc. of SPIE Int. Society for Optical Engineering*, vol. 6174, pp. 617408-1-12, 2006.

[47] Gu Hang-ming, Lu Miadz, Zhou Xue-fend, Liang Chun-guand, Gaa Bao-xin, “Transient Response Characterization of Ohmic Contact RF MEMS Switches,” *Proc. 3rd Int. Conf. on Microwave and Millimeter Wave Technology*, pp. 271-4, 2002.

[48] W. Li and P. Liu, “Robust adaptive tracking control of uncertain electrostatic micro-actuators with H-infinity performance”. *Mechatronics*, vol. 19, no. 5, pp. 591-597, 2009.

[49] Q. Yang, and S. Jagannathan, "A Suite of Robust Controllers for the Manipulation of Microscale Objects," *IEEE Transactions on Systems, Man, and Cybernetics, Part B: Cybernetics*, vol. 38, no. 1, pp. 113-125, 2008.

[50] G. Zhu, J. Penet, and L. Saydy, "Modeling and control of electrostatically actuated MEMS in the presence of parasitics and parametric uncertainties," *Journal of Dynamic Systems, Measurement and Control*, vol. 129, no. 6, pp. 786–794, 2007.

[51] F. Amato and M. Ariola, "Finite Time Control of Discrete Time Linear System", *IEEE Trans. Automatic Control*, pp. 724-729, 2005

[52] H. Ichihara and H. Katayama, "Finite-time control for linear discrete-time systems with input constraints", *American Control Conference*, pp. 1171-1176, 2009.

[53] J. Back and H. Shim, "An Inner-Loop Controller Guaranteeing Robust Transient Performance for Uncertain MIMO Nonlinear Systems", *IEEE Transactions on Automatic Control*, vol. 54, no. 7, pp. 1601-7, 2009.

[54] L. Freidovich, and H. Khalil, "Performance Recovery of Feedback-Linearization-Based Designs," *IEEE Transactions on Automatic Control*, vol. 53, no. 10, pp. 2324-34, 2008.

[55] A. Chakrabortty and M. Arcak, "Time-scale separation redesigns for stabilization and performance recovery of uncertain nonlinear systems," *Automatica*, vol. 45, no. 1, pp. 34-44, 2009.

[56] B. Hahn, K. Oldham, "A Model-Free On-Off Iterative Adaptive Controller Based on Stochastic Approximation," *American Control Conference*, pp. 1665-70, 2010.

[57] C. Goldsmith, J. Ehmke, A. Malczewski, B. Pillans, S. Eshelman, Z. Yao, J. Brank, and M. Eberly, "Lifetime Characterization of Capacitive RF MEMS switches," *IEEE MTT-S International Microwave Symposium Digest*, p 227-230, 2001.

[58] D. Bernstein, "Matrix Mathematics", 2nd ed., Princeton University Press, NJ, 2009.

[59] J. Doyle, A. Packard, and K. Zhou, "Review of LFTs, LMIs, and mu," *Proc. of the 30th Conf. on Decision and Control*, vol. 2, pp. 1227-1232, 1991.

[60] P. Lambrechts, J. Terlouw, S. Bennani, and M. Steinbuch, "Parametric Uncertainty Modeling using LFTs," *American Control Conferences*, vol.1, pp. 267-72, 1993

[61] S. Hecker and A. Varga, "Generalized LFT-based representation of parametric uncertain models," *European Journal of Control*, vol. 10, no. 4, pp. 326-337, 2004.

[62] S. Barnett, 1990. Matrices: Methods and Application, Oxford Applied Mathematics and Computing Science Series, Oxford University Press, NY.

[63] G. Balas, J. Doyle, K. Glover, A. Packard, and R. Smith, "μ-Analysis and Synthesis Toolbox", MATLAB manual, The MathWorks.

[64] K. Williams, K. Gupta, and M. Wasilik, "Etch Rates for Micromachining Processing - Part II," *Journal of Microelectromechanical Systems*, vol. 12, no. 6, pp. 761-78, 2003.

[65] S. Kim, J. Kim, J. G. Koo, K. S. Nam, K.-I. Cho, and I.-H. Bae, "Trench formation and filling technique for dielectric isolation of plasma display panel driver integrated circuits," *J. Vac. Sci. Technol. B*, vol. 18, no. 5, p 2482-5, 2000.

[66] F. Ayazi and K. Najafi, "High aspect-ratio polysilicon micromachining technology," *Sensors and Actuators A*, vol. A87, no. 1-2, pp. 46-51, 2000.

[67] Y. Fu, H. Du, W. Huanga, S. Zhang, and M. Hua, "TiNi-based thin films in MEMS applications: A Review," *Sensor and Actuator A*, vol. 112, no. 2-3, pp. 395-408, 2004.

[68] S. Lee, G. Ditmer, N. Singh, C. Hodson, A. Goodyear, and M. Cooke, "Thick-film Doped-oxide Deposition Processes for Applications in Planar Lightwave Circuit Fabrication," *Conf. on Optoelectronic and Microelectronic Materials and Devices*, pp. 441-5, 2002.

[69] M. A. Hopcroft, M. D. Nix, and T.W. Kenny, "What is the Young's Modulus of Silicon?," *Journal of Microelectromechanical Systems*, vol. 19, no. 2, pp. 229-38, 2010.

[70] B. Donald, C. Levey, C. McGray, I. Paprotny, and D. Rus "An Untethered, Electrostatic, Globally Controllable MEMS Micro-Robot," *Journal of Microelectromechanical Systems*, vol. 15, no. 1, pp. 1-15, 2006.

[71] S. Chakraborty, A. R. Chaudhuri, and T. K. Bhattacharyya, "Transient Analysis of MEMS Cantilever based Binary Inverter and Design of a Ring Oscillator," *International Conference on Computers and Devices for Communication*, 2009.

[72] C.-Y. Tsai, W.-T. Kuo, C.-B. Lin, and T.-L. Chen, "Design and fabrication of MEMS logic gates," *Journal of Micromechanics and Microengineering*, vol. 18, no. 4, p 045001, 2008.

[73] P. Dario, R. Valleggi, M. C. Carrozza, M. C. Montesi, and M. Cocco, "Microactuators for microrobots: a critical survey," *J. Micromech. Microeng.*, vol. 2, no. 3, pp. 141 – 157, 1992.

[74] T. Ebefors , J. U. Mattsson , E. Kälvesten , and G. Stemme , "A walking silicon micro-robot," *Proc. Transducers*, pp. 1202–1205, 1999.

[75] R. Murthy, A. Das, and D. O. Popa, "ARRIpede: An assembled micro crawler," *Proc. IEEE Conf. Nanotechnology,* pp. 833 – 836, 2008.

[76] S. Hollar, A. Flynn, C. Bellew, and K. S. J. Pister, "Solar powered 10 mg silicon robot," *Proc. IEEE Int. Conf. MEMS*, pp. 706 – 711, 2003.

[77] S. Bergbreiter, and K. S. J. Pister, "Design of an autonomous jumping microrobot," *Proc. IEEE Int. Conf. Robotics and Automation*, pp. 447 – 453, 2007.

[78] B. R. Donald, C. G. Levey, and I. Paprotny, "Planar microassembly by parallel actuation of MEMS microrobots," *J. Microelectromech. Syst.,* vol. 17, no. 4, pp. 789 – 808, Aug. 2008.

[79] M. H. Mohebbi, M. L. Terry, K. F. Bohringer, G. T. A., Kovacs, and J. W. Suh, "Omnidirectional walking microrobot realized by thermal microactuator arrays," *Proc. ASME Int. Mechanical Engineering Congress and Exposition*, pp. 167 – 173, 2001.

[80] K. R. Oldham, C. Rhee, J. Ryou, R. Polcawich, and J. Pulskamp, "Lateral thin-film piezoelectric actuators for bio-inspired micro-robotic locomotion," *Proc. ASME Int. Conf. DETC,* vol. 6, pp. 759 – 768, 2009.

[81] B. Edamana, B. Hahn, J. S. Pulskamp, R. G. Polcawich, and K. R. Oldham, "Modeling and optimal low-power on-off control of thin-film piezoelectric rotational actuators," *IEEE/ASME Trans. Mechatron.*, vol. 16, no. 5, pp. 884 – 896, 2011.

[82] Z. Qiu, J. S. Pulskamp, X. Lin, C. Rhee, T. Wang, R. G. Polcawich, and K. R. Oldham, "Large displacement vertical translational actuator based on piezoelectric thin films," *J. Micromech. Microeng.*, vol. 20, no. 7, pp. 1 – 10, 2010.

[83] R. T. Howe and R. S. Muller, "Polycrystalline and amorphous silicon micromechanical beams: annealing and mechanical properties," *Sens. Actuators*, vol. 4, no. 3, pp. 447 – 454, 1983.

[84] R. Murthy, and D. O. Popa, "A four degree of freedom microrobot with large work volume," *Proc. IEEE Int. Conf. Robotics and Automation*, pp. 1028 – 1033, 2009.

[85] K. R. Oldham, B. Hahn, and P. Park, "On-off control for low-power servo control in piezoelectricmicro-robotics," *Proc. ASME Dyn. Syst. Control Conf.*, pp. 1269 – 1276, 2008.

[86] J. P. Pulskamp and R. G. Polcawich, "Negative vertical deflection piezoelectric MEMS actuators method of fabrication," U.S. Patent No. 7,944,121, May 17, 2011.

[87] J. P. Pulskamp and R. G. Polcawich, "Large force and displaement piezoelectric MEMS lateral actuator," U.S. Patent No. 7,876,026, Jan. 25, 2011.

[88] S. Franssila, 2010, "Yield and Reliability, in Introduction to Microfabrication," Second Edition, John Wiley & Sons, Ltd, Chichester, UK. doi: 10.1002/9781119990413.ch36

[89] S. F. Elahi and T. D. Wang, "Future and advances in endoscopy," *J. Biophotonics*, vol. 4, no. 7–8, pp. 471–481, 2011.

[90] W. Piyawattanametha and T. D. Wang, 2010, "Miniature Dual Axes Confocal Microscope forReal Time In Vivo Imaging," Advances in Solid State Circuit Technologies, Intech, pp. 393 – 430.

[91] Ryan Rudy, "Optimization of Layer Thicknesses for Improved Weight-Bearing and Mobility of mm-Scale Ground Mobile Robotics," ME590 Report, University of Michigan, 2010.

[92] G. K. Lau, T. Chu Duc, J. F. L. Goosen, P. M. Sarro and F. vanKeulen, "An in-plane thermal unimorph usingconfined polymers," *Journal of Micromechanics and Microengineering*, vol.17, pp. S174–S183, 2007.

[93] K. Kuribayashi and T. Fujfi, "A New Micro SMA Thin Film Actuator Prestrained by Polyimide," *Int. Symposium on Micromechatronics and Human Science*, pp. 165 – 170, 1998.

[94] E. Quandt, "MEMS actuators based on smart film materials," *Proc. SPIE Micromachined Devices and Components IV*, vol. 3514, pp. 136-146, 1998.

[95] Micromo, DC motor, from http://www.micromo.com/microsystems-starter-kits.aspx

[96] Squiggle micro motor, from http://www.newscaletech.com/squiggle_overview.html

[97] M. D. Volder, J. Coosemans, R. Puers, and D. Reynaerts, "Characterization and control of a pneumatic microactuator with an integrated inductive position sensor," *Sensor and Actuators*, vol. 141, pp. 192 – 200, 2008.

[98] T. Sandner, T. Grasshoff, H. Schenk, and A. Kenda, "Out-Of-Plane Translatory MEMS actuator with extraordinary large stroke for optical path length modulation," *Proc. SPIE MOEMS and Miniaturized Systems X*, vol. 7930, pp. 79300I, 2011.

[99] S. Chen, "Design of a high-speed-force-stroke thermomechanical micro-actuator via geometric contouring and mechanical frequency multiplication," Ph.D. Dissertation, Massachusetts Institute of Technology, 2007.

[100] L. Wu and H. Xie, "A large vertical displacement electrothermal bimorph microactuator with very small lateral shift," *Sensor and Actuators*, pp. 371 – 379, 2008.

[101] T. F. Hill "Analysis of DRIE Uniformity for Microelectromechanical Systems," MS Thesis, University of Illinois at Urbana-Champaign, 2001

[102] L. Schenato, Wei-Chung Wu, L. El Ghaoui, and K. Pister, "Process variation analysis for MEMS design," *Proc. of SPIE – Int. Society for Optical Engineering*, vol. 4236, pp. 272-9, 2001

[103] C. Zang, M. I. Friswell, J. E. Mottershead, "A review of robust optimal design and its application in dynamics," *Computers and Structures*, vol. 83, no. 4-5, pp. 315-326, 2005.

[104] J. S. Han and B. M. Kwak, "Robust optimization using a gradient index: MEMS applications," *Structural and Multidisciplinary Optimization*, vol. 27, no. 6, pp. 469-78, 2004.

[105] G. Steiner, A. Weber, and C. Magele, "Managing Uncertainties in Electromagnetic Design Problem With Robust Optimization," *IEEE Transactions on Magnetics*, vol. 40, no. 2, pp. 1094-9, 2004.

[106] T. Namerikawa, M. Fujita, R. S. Smith, and K. Uchida, "On the H_∞ Control System Design Attenuating Initial State Uncertainties," *Trans. Of the Society of Intrument and Control Engineer*, vol. 40, no. 3, 2004.

[107] Y. Soeno, S. Ichikawa, T. Tsuna, Y. Sato, and I. Sato, "Piezoelectric Piggy-Back Microactuator for Hard Disk Drive," *IEEE Transactions on Magentics*, vol. 35, no. 2, pp. 983 – 987, 1999.

[108] J.Q. Mou, Y. Lu, J.P. Yang, B.B. Lim, and S. X. Chen, "Thermal stability modeling and evaluation of piggy-back microactuator for hard disk drives," *Digest of the Asia-Pacific Magnetic Recording Conference*, p WE-P-13-01-We-P-13-02, 2002

[109] P. Muralt, R. G. Polcawich, and S. Trolier-Mckinstry, "Piezoelectric Thin Films for Sensors, Actuators, and Energy Harvesting," *MRS Bulletin*, vol. 34, pp. 658 – 664, 2009.

[110] E. Yoon, "Overview of Lab-on-Chip Technologies and Microfabrication Processes," Lab-on-Chip Workshop at Lurie Nanofabrication Facility, 2009.

[111] S. J. Gross, "Micromachined Switches and Cantilever Actuatorsbased on Piezoelectric Lead Zirconate Titanate (PZT)," Ph.D. Dissertation, Pennsylvania State University, 2004.

[112] S. Awtar and G. Parmar, "Design Of A Large Range XY Nanopositioning System," *Proc. of ASME Design Engineering Technical Conference*, vol. 2, pp. 387-399, 2010.

[113] D. Molinero and L. Castaner, "Transient discharge current measurements to study dielectric charging in MEMS," *Proc. Spanish Conf. on Electron Devices*, pp. 285-288, 2009.

[114] X. Yuan, J. C. M. Hwang, D. Forehand, and C. L. Goldsmith, "Modeling and Characterization of Dielectric-Charging Effects in RF MEMS Capacitive Switches," *IEEE MTT-S International Microwave Symposium Digest*, pp. 753-756, 2005.

[115] L. P. Wang, R. Wolf, Q. Zhou, S. Trolier-McKinstry, and R. J. Davis, "Wet-etch patterning of lead zirconate titanate (PZT) thick films for microelectromechanical systems (MEMS) applications," *Materials Science of Microelectromechanical Systems (MEMS) Devices III*, vol. 657, pp. EE5391-EE5396, 2001.

[116] PZT Wet Etching. from http://ssel-sched.eecs.umich.edu/wiki/Public.PZT%20Wet%20Etching.ashx

[117] K. Kanda, T. Iga, T. Hashimoto, T. Fujita, K. Higuchi, and K. Maenaka, "Microfabrication and Application of Series-Connected PZT Elements," *Procedia Chemistry*, vol. 1, no. 1, pp. 808-811, 2009.

[118] Y. Kokaze, I. Kimura, M. Endo, M. Ueda, S. Kikuchi, Y. Nishioka, K. and Suu, "Dry Etching Process for Pb(Zr, Ti)O_3 Thin-Film Actuators," Japanese Journal of Applied Physics, vol. 46, no. 1, pp. 280 – 282, 2007.

[119] K. T. Lim, K. T. Kim, D. P. Kim, and C. I Kim, "Reduction of etching damage in lead-zirconate-titanate thin films with inductively coupled plasma," *Journal of Vacuum Science & Technology A*, vol. 21, no. 4, pp. 1563-7, 2003.

[120] E. Zakar, "Surface Analysis of Reactive Ion Etched PZT Thin Films in SF_6 Plasma," ARL-TR-4284, Army Research Laboratory, 2007.